

**SPATIAL AND TEMPORAL SYSTEM CALIBRATION OF GNSS/INS-
ASSISTED FRAME AND LINE CAMERAS ONBOARD UNMANNED
AERIAL VEHICLES**

by

Lisa M. LaForest

A Dissertation

Submitted to the Faculty of Purdue University

In Partial Fulfillment of the Requirements for the degree of

Doctor of Philosophy



Lyles School of Civil Engineering

West Lafayette, Indiana

August 2020

THE PURDUE UNIVERSITY GRADUATE SCHOOL
STATEMENT OF COMMITTEE APPROVAL

Dr. Ayman Habib, Chair

Lyles School of Civil Engineering

Dr. Melba Crawford

Lyles School of Civil Engineering

Dr. James Bethel

Lyles School of Civil Engineering

Dr. Henry Theiss

Centauri

Approved by:

Dr. Dulcy Abraham

To my beloved children, Nora and Lucas LaForest.

ACKNOWLEDGMENTS

I would like to first extend my deepest gratitude to my advisor Dr. Ayman Habib. I would not have been able to produce this work without his extensive knowledge and countless hours of guidance, patience, encouragement, and unwavering support. I am truly grateful for the experience and opportunity to have worked with Dr. Ayman Habib.

I would also like to express my deepest appreciation to the members of my committee: Dr. James Bethel, Dr. Melba Crawford, and Dr. Henry Theiss. Each of them has greatly helped deepen my understanding of Geomatics and research methods. I am extremely thankful for their support. A special acknowledgment is given to the members and team leaders of the Digital Photogrammetry Research Group (DPRG) and Laboratory for Applications of Remote Sensing (LARS) research groups for collaboration, data collections, and data system acquisition, especially Meghdad Hasheminasab and Tian Zhou.

I'd like to recognize several others that have supported me during my Ph.D. studies. First, I want to thank Dr. Edward Mikhail, whose support and guidance led me to this program. Also, I would like to recognize my friends and colleagues at the National Geospatial Intelligence Agency for their years of encouragement and support, particularly those in the Precision Engagement Division and the photogrammetric community.

I would also like to thank my family. My mother, Kellie, who has always encouraged me from the beginning. My aunt, Colleen Walsh, who has continually supported me and instilled the importance of education and work-ethic. My siblings, Dennis and Brittany Lee, who have given their companionship and timely guidance and support.

An extreme heartfelt appreciation is given to my husband and best friend, Alex, who has tirelessly supported and encouraged me throughout my Ph.D. journey. His dedication and support to my studies and our family is unparalleled. Lastly, a special thanks to my daughter, Nora, who, even as a toddler, continually shows me the importance of curiosity, perseverance, and lightheartedness.

Furthermore, the information, data, or work presented herein was funded in part by the Civil Engineering Center for Applications of UAS for a Sustainable Environment (CE CAUSE), Army Research Office (ARO), and the Advanced Research Projects Agency Energy (ARPA E), U.S. Department of Energy, under Award Number DE AR0001135. The work was also partially

supported by the Nationally Geospatial Intelligence Agency (NGA). The contents of this proposal reflect the views of the author, who is responsible for the facts and the accuracy of the data presented herein, and do not necessarily reflect the official views or policies of the sponsoring organizations. Approved for public release, 21-442.

TABLE OF CONTENTS

LIST OF TABLES	9
LIST OF FIGURES	12
LIST OF ACRONYMS	15
ABSTRACT.....	16
1. PROBLEM STATEMENT	18
1.1 Background	18
1.2 Challenges in System Calibration of Consumer-Grade Sensors.....	19
1.3 Research Objectives	20
1.4 Dissertation Outline	22
2. LITERATURE REVIEW	23
2.1 Overview	23
2.2 Spatial System Calibration.....	23
2.3 Hardware Time Synchronization Solutions	24
2.4 Spatial and Temporal System Calibration: Software Time Delay Solutions.....	26
2.5 Summary	29
3. FRAME CAMERAS – NEW STRATEGIES FOR TIME DELAY ESTIMATION DURING SYSTEM CALIBRATION FOR UAV-BASED GNSS/INS-ASSISTED IMAGING SYSTEM	31
3.1 Introduction.....	32
3.2 Related Work	35
3.3 Methodology	39
3.3.1 Conceptual Basis of Bundle Block Adjustment	39
3.3.2 Direct Approach for Time Delay Estimation.....	42
3.3.3 Optimal Flight Configuration for System Calibration while Considering Time Delay	45
3.3.4 Indirect Approach for Time Delay Estimation	50
3.4 Experimental Results	52
3.4.1 Date Acquisition	52
3.4.2 Dataset Description.....	54

3.4.3	Experimental Results and Analysis	60
3.5	Conclusions and Recommendations for Future Work	81
3.6	Acknowledgements	84
4.	SYSTEM CALIBRATION INCLUDING TIME DELAY ESTIMATION FOR GNSS/INS- ASSISTED LINE CAMERAS ONBOARD UAV PLATFORMS	85
4.1	Introduction and Related Work	86
4.2	Methodology	88
4.2.1	Collinearity Equations for Frame and Line Camera Systems	88
4.2.2	Direct Approach for Time Delay Estimation in Line Camera Systems	90
4.2.3	Optimal Flight Configuration for Line Camera System Calibration while Considering Time Delay	93
4.3	Experimental Results	96
4.3.1	Data Acquisition	97
4.3.2	Dataset Description	99
4.3.3	Experimental Results and Analysis	101
4.4	Conclusions and Recommendations for Future Research	115
5.	SYSTEM CALIBRATION WITH TIME DELAY ESTIMATION FOR UAV-BASED FRAME AND LINE CAMERAS USING AUTOMATICALLY-DERIVED TIE POINTS.....	116
5.1	Introduction	117
5.2	Related Work	121
5.3	System Specifications and Dataset Description	123
5.4	Methodology for Automated Feature Extraction and System Calibration	126
5.4.1	Automated Feature Extraction and Matching for Frame Camera Systems	126
5.4.2	Automated Feature Extraction and Matching for Line Camera Systems	130
5.4.3	System Calibration for Frame and Line Camera using Automatically-Derived Tie Points	140
5.5	Experimental Results	145
5.5.1	DJI M200 integrated with FLIR Duo Pro R – FLIR RGB Frame Sensor	146
5.5.2	DJI M600 integrated with nHS-70 Hyperspectral Line Camera Sensor	150
5.6	Conclusions and Recommendations for Future Work	153
6.	CONCLUSIONS AND RECOMMENDATIONS FOR FUTURE WORK	154

6.1 Research Conclusions	154
6.2 Recommendations for Future Work.....	157
APPENDIX.....	159
REFERENCES	161

LIST OF TABLES

Table 3.1 Dependency of the bias impact for the system calibration parameters on flight configuration & image point location	49
Table 3.2 FLIR and Sony nominal boresight angles, lever arm components, and angular field of view.....	54
Table 3.3 FLIR and Sony flight parameters for the different data acquisition dates.....	56
Table 3.4 Interior orientation parameters (IOPs) for the FLIR and Sony cameras.....	62
Table 3.5 Estimated parameter results for the DJI M200 thermal platform, including the standard deviation for direct results.	64
Table 3.6 Correlation matrix of system parameters for July 25th thermal direct approach results.	65
Table 3.7 Components and mean/standard deviation/RMSE of the differences between checkpoints and surveyed coordinates for the five checkpoints for the DJI M200 thermal platform.	66
Table 3.8 Mean standard deviation of five checkpoints from direct approach for the DJI M200 thermal platform from mini bundle adjustment.	68
Table 3.9 Derived statistics of horizontal/planimetric coordinate differences for the five checkpoints derived from the orthophoto from the DJI M200 thermal platform.	70
Table 3.10 Estimated parameter results for the DJI M200 RGB platform including the standard deviation for direct results.	73
Table 3.11 Components and mean/standard deviation/RMSE of the differences between checkpoint and surveyed coordinates for the five checkpoints for the DJI M200 RGB platform.....	74
Table 3.12 Mean standard deviation of five checkpoints from direct approach for the DJI M200 RGB platform from mini bundle adjustment.	75
Table 3.13 Derived statistics of horizontal/planimetric coordinate differences for the five check targets derived from the orthophoto for DJI M200 RGB platform.....	76
Table 3.14 Estimated parameter results for the DJI M600 platform, including the standard deviations for the direct results.	79
Table 3.15 Components and mean/standard deviation/RMSE of the differences between checkpoint and surveyed coordinates for the five checkpoints for the DJI M600 platform—Sony RGB.	80
Table 3.16 Mean standard deviation of five checkpoints from direct approach for the DJI M600 platform from bundle adjustment.....	80

Table 3.17 Derived statistics of horizontal/planimetric coordinates for five check targets derived from orthophoto—DJI M600 platform.	81
Table 4.1 Impact of bias in system parameters on 3D point coordinates for frame and line camera systems	94
Table 4.2 Headwall nominal boresight angles and lever arm components.....	99
Table 4.3 Flight parameters for the different systems and collection dates.....	100
Table 4.4 Estimated system parameter including the standard deviation and a-posteriori variance factor	102
Table 4.5 Correlation matrix of system parameters for July 09 th nHs-70 direct approach results	104
Table 4.6 Relative accuracy evaluated through the mean standard deviation of checkpoints derived from the bundle adjustment and the absolute accuracy measured through the Mean/Standard Deviation/RMSE of the differences between checkpoint and surveyed coordinates of the five checkpoints from direct approach	Error! Bookmark not defined.
Table 4.7 Estimated system parameter including the standard deviation and a-posteriori variance factor with 200 ms artificial time delay introduced	110
Table 4.8 Relative accuracy evaluated through the mean standard deviation of checkpoints derived from the bundle adjustment and the absolute accuracy measured through the Mean/Standard Deviation/RMSE of the differences between checkpoint and surveyed coordinates of the five checkpoints from direct approach	112
Table 4.9 Estimated system parameter including the standard deviation and a-posteriori variance factor	114
Table 4.10 Correlation matrix of system parameters for July 09 th nHs-70 indirect approach results	114
Table 5.1 FLIR RGB and Headwall nHS-70 platform’s nominal boresight angles and lever arm components	125
Table 5.2 Flight parameters and dataset description for the imaging systems	126
Table 5.3 Estimated system parameters including the standard deviation and a-posteriori variance factor for FLIR RGB system.....	148
Table 5.4 Correlation matrix for system parameters of the checkpoint and the SIFT point results for FLIR RGB system	148
Table 5.5 Mean standard deviation of check/SIFT points derived from the bundle adjustment for the FLIR RGB system.....	149
Table 5.6 Statistics of the differences between the RTK/GNSS measurements of the checkpoints and those derived either by the bundle adjustment when using only check points or by multi-light ray intersection using the derived system parameters from the SIFT-based bundle adjustment for the FLIR RGB system.....	149

Table 5.7 Estimated system parameters including the standard deviation and a-posteriori variance factor for nHS-70 line camera system	151
Table 5.8 Correlation matrix of system parameters for the checkpoint and the SIFT point results for nHS-70	152
Table 5.9 Mean standard deviations of check/SIFT points derived from the bundle adjustment for the nHS-70 system	152
Table 5.10 Statistics of the differences between the RTK/GNSS measurements of the checkpoints and those derived either by the bundle adjustment when using only check points or by multi-light ray intersection using the derived system parameters from the SIFT-based bundle adjustment for the nHS-70 system	152

LIST OF FIGURES

Figure 1.1 (a) Orthophoto generated without (a) and with (b) considering time delay	20
Figure 2.1 Illustration of Simulated Feedback Approach Diagram	25
Figure 2.2 Illustration of Simulated Feedback Approach Combined with the Optical Clock Method	25
Figure 2.3. Illustration of Direct Feedback Approach	26
Figure 3.1 (a) Orthophoto generated while ignoring the time delay during calibration. (b) Orthophoto generated with time delay accounted for during calibration.	33
Figure 3.2. Conceptual basis of bundle block adjustment	40
Figure 3.3 Illustration of collinearity equations.....	41
Figure 3.4 Establishing an expression for the correct IMU body frame orientation in the presence of time delay	44
Figure 3.5 Illustration of the direct approach for time delay estimation within the bundle block adjustment with system self-calibration.....	45
Figure 3.6. Illustration of where measurements are taken to acquire the nominal lever arm values.	50
Figure 3.7 Processing workflow of the indirect approach process for time delay estimation.	51
Figure 3.8 M200-based thermal/RGB system configuration.	53
Figure 3.9 DJI M600-based Sony Alpha 7R system configuration.	54
Figure 3.10 Trajectory and target locations for FLIR Duo Pro R and Sony Alpha 7R.	57
Figure 3.11 (a) XYZ component linear velocity over flight time for the July 25 th thermal dataset. (b) ω , ϕ , κ component angular velocity over flight time for the July 25 th thermal dataset.....	57
Figure 3.12 Sample corresponding thermal and RGB images from the FLIR Duo Pro R.	58
Figure 3.13 Flight area with enhanced representations of checkerboard targets and sample thermal and RGB images of the FLIR camera around the target location.	59
Figure 3.14 Sample images captured by the Sony RBG sensor over the calibration test field. (a) 20m flying height and (b) 40m flying height.....	59
Figure 3.15 Sony A7R calibration field.	59
Figure 3.16 Distribution of the tie points used for the FLIR thermal sensor in the Sept. 14th collection date for the direct (right) and indirect* (left) approaches (*only 10% of total tie points are plotted).	68

Figure 3.17 Orthophoto result while ignoring the time delay using the original trajectory data for FLIR thermal July 25 th data collection (red boxes show the location of the checkpoints, <i>Original Image GSD</i> $\approx 0.03m$).	70
Figure 3.18 Orthophoto result while ignoring the time delay using the refined trajectory data for FLIR thermal July 25 th data collection (red boxes show the location of the checkpoints, <i>Original Image GSD</i> $\approx 0.03m$).	71
Figure 3.19 Orthophoto result from direct approach for FLIR thermal July 25 th data collection (red boxes show the location of the checkpoints, <i>Original Image GSD</i> $\approx 0.03m$).	71
Figure 3.20 Orthophoto result from direct approach for FLIR thermal September 14 th data collection (red boxes show the location of the checkpoints, <i>Original Image GSD</i> $\approx 0.03m$)...	71
Figure 3.21 Orthophoto result ignoring the time delay using the original trajectory data for FLIR RGB July 25 th data collection (red boxes show the location of the checkpoints—only two visible, <i>Original Image GSD</i> $\approx 0.01m$).	77
Figure 3.22 Orthophoto result ignoring the time delay using the refined trajectory data for FLIR RGB July 25 th data collection (red boxes show the location of the checkpoints, <i>Original Image GSD</i> $\approx 0.01m$).	77
Figure 3.23 Orthophoto result from direct approach for FLIR RGB July 25 th data collection (red boxes show the location of the checkpoints, <i>Original Image GSD</i> $\approx 0.01m$).	77
Figure 3.24 Orthophoto result from direct approach for FLIR RGB Sept. 14 th data collection (red boxes show the location of the checkpoints, <i>Original Image GSD</i> $\approx 0.01m$).	78
Figure 3.25 Orthophoto result from direct approach for Sony—May 06 th data collection (red boxes show the location of the checkpoints, <i>GSD</i> $\approx 0.0056m$).	81
Figure 4.1 Illustration of collinearity equations for (a) frame camera and (b) push-broom line camera.	90
Figure 4.2 DJI M600P equipped with nHS-70 and uVS-307 system configuration	98
Figure 4.3 DJI M600P equipped with nHS-199 system configuration	98
Figure 4.4 Ground control point locations and trajectory for the July 09 th nHS-70/uVS-307 platform	100
Figure 4.5 (a) Sample of the raw (a) uVS-307 SWIR and (b) nHS-70 VNIR imagery in the calibration field with enhanced representation of the targets.	101
Figure 4.6 Tie point distribution for (a) uVS-307 July 09 th dataset and (b) uVS-August 14 th dataset.	108
Figure 5.1 Illustration of (a) frame camera and (b) line camera sensor data acquisition and overlapping sample scenes for frame (c) and line (d) camera imagery	119
Figure 5.2 Scale difference in sample overlapping imagery captured from 40 m and 20 m flying heights, (a) frame images, and (b) line scenes.	120

Figure 5.3 System configuration for the DJI M200 equipped with the FLIR RGB frame sensor	125
Figure 5.4 System configuration for the DJI M600P equipped with the nHS-70 line sensor	125
Figure 5.5 Sample SIFT matching results, (a) initial matches, and (b) remaining matches after Nister/RANSAC step* (*for a better visualization, only 10% of total matched features are plotted)	129
Figure 5.6 Samples of raw scenes for nHS-70 VNIR 20190709 dataset, (a) and (b) raw scenes and (c) and (d) zoomed-in regions.....	131
Figure 5.7 Flowchart of the proposed approach for automatically establishment of conjugate features in line cameras.....	132
Figure 5.8 Schematic illustration of the iterative ortho-rectification process for line camera scenes, (a) projection of a given DSM cell onto the initial scan line, (b) iterating the projection process using an updated scan line, (c) final projection, and (d) assigning RGB values from the projected point to the ortho-rectified cell.	134
Figure 5.9 Samples of partially ortho-rectified scenes for the nHS-70 VNIR 20190709 dataset, (a) and (b) partially ortho-rectified scenes and (c) and (d) zoomed-in regions.....	135
Figure 5.10 Illustration of the propoposed feature matching strategy using the nHS-70 VNIR 20190709 dataset, (a) detected SIFT features (red dots) on partially ortho-rectified scene, denoted as first scene, (b) detected SIFT features (red dots) on partially ortho-rectified scene, denoted as second scene, (c) selected feature in first scene (left image) and its corresponding search window and established conjugate feature in second scene (right image), (d) zoomed-in views of the established conjugate features, and (e) final 558 matched features between the two ortho-rectified scenes.	137
Figure 5.11 A sample tracked SIFT feature, (a) trackd feature (in red) is shown on three differnet partially-orthorectified scenes, and (b) illustration of the tracked feature on the corresponding raw scenes.	139
Figure 5.12 Illustration of collinearity equations for (a) frame and (b) line camera.	142
Figure 5.13 Illustration of estimated precision of a bundle adjustment based on intersection geometry	149
Figure 5.14 Mean intersection geometry for the check points and mean and maximum intersection geometry of the FLIR RGB SIFT object points.....	150
Figure A.1 Illustration of the change in the scale as a result of angular sensor tilt	160

LIST OF ACRONYMS

AFOV	Angular Field of View	POS	Position and Orientation System
ARPA-E	Advanced Research Project Agency-Energy	PPS	Pulse Per Second
DJI	Dà-Jiāng Innovations	RANSAC	RANdom SAmple Consensus
DSM	Digital Surface Model	RGB	Red, Green, and Blue
EOPs	Exterior Orientation Parameters	RMSE	Root-Mean-Square Error
FOV	Field of View	ROPs	Relative Orientation Parameters
GCP	Ground Control Point	RTK	Real-Time Kinematic
GNSS	Global Navigation Satellite System	SfM	Structure from Motion
GSD	Ground Sampling Distance	SIFT	Scale Invariant Feature Transform
IMU	Inertial Measurement Unit	SURF	Speeded Up Robust Features
INS	Inertial Navigation System	SVD	Singular Value Decomposition
IOPs	Interior Orientation Parameters	SWIR	Short Wavelength Infrared
ISO	Integrated Sensor Orientation	UAV	Unmanned Aerial Vehicle
LiDAR	Light Detection and Ranging	VNIR	Visible and Near-Infrared
LSA	Least Squares Adjustment		
MAV	Micro Aerial Vehicle		
NGA	National Geospatial Intelligence Agency		

ABSTRACT

Unmanned aerial vehicles (UAVs) equipped with imaging systems and integrated global navigation satellite system/inertial navigation system (GNSS/INS) are used for a variety of applications. Disaster relief, infrastructure monitoring, precision agriculture, and ecological forestry growth monitoring are among some of the applications that utilize UAV imaging systems. For most applications, accurate 3D spatial information from the UAV imaging system is required. Deriving reliable 3D coordinates is conditioned on accurate geometric calibration. Geometric calibration entails both spatial and temporal calibration. Spatial calibration consists of obtaining accurate internal characteristics of the imaging sensor as well as estimating the mounting parameters between the imaging and the GNSS/INS units. Temporal calibration ensures that there is little to no time delay between the image timestamps and corresponding GNSS/INS position and orientation timestamps. Manual and automated spatial calibration have been successfully accomplished on a variety of platforms and sensors including UAVs equipped with frame and push-broom line cameras. However, manual and automated temporal calibration has not been demonstrated on both frame and line camera systems without the use of ground control points (GCPs). This research focuses on manual and automated spatial and temporal system calibration for UAVs equipped with GNSS/INS frame and line camera systems. For frame cameras, the research introduces two approaches (direct and indirect) to correct for time delay between GNSS/INS recorded event markers and actual time of image exposures. To ensure the best estimates of system parameters without the use of ground control points, an optimal flight configuration for system calibration while estimating time delay is rigorously derived. For line camera systems, this research presents the direct approach to estimate system calibration parameters including time delay during the bundle block adjustment. The optimal flight configuration is also rigorously derived for line camera systems and the bias impact analysis is concluded. This shows that the indirect approach is not a feasible solution for push-broom line cameras onboard UAVs due to the limited ability of line cameras to decouple system parameters and is confirmed with experimental results. Lastly, this research demonstrates that for frame and line camera systems, the direct approach can be fully-automated by incorporating structure from motion (SfM) based tie point features. Methods for feature detection and matching for frame and line camera systems are presented. This research also presents the necessary changes in the bundle

adjustment with self-calibration to successfully incorporate a large amount of automatically-derived tie points. For frame cameras, the results show that the direct and indirect approach is capable of estimating and correcting this time delay. When a time delay exists and the direct or indirect approach is applied, horizontal accuracy of 1–3 times the ground sampling distance (GSD) can be achieved without the use of any ground control points (GCPs). For line camera systems, the direct results show that when a time delay exists and spatial and temporal calibration is performed, vertical and horizontal accuracy are approximately that of the ground sample distance (GSD) of the sensor. Furthermore, when a large artificial time delay is introduced for line camera systems, the direct approach still achieves accuracy less than the GSD of the system and performs 2.5-8 times better in the horizontal components and up to 18 times better in the vertical component than when temporal calibration is not performed. Lastly, the results show that automated tie points can be successfully extracted for frame and line camera systems and that those tie point features can be incorporated into a fully-automated bundle adjustment with self-calibration including time delay estimation. The results show that this fully-automated calibration accurately estimates system parameters and demonstrates absolute accuracy similar to that of manually-measured tie/checkpoints without the use of GCPs.

1. PROBLEM STATEMENT

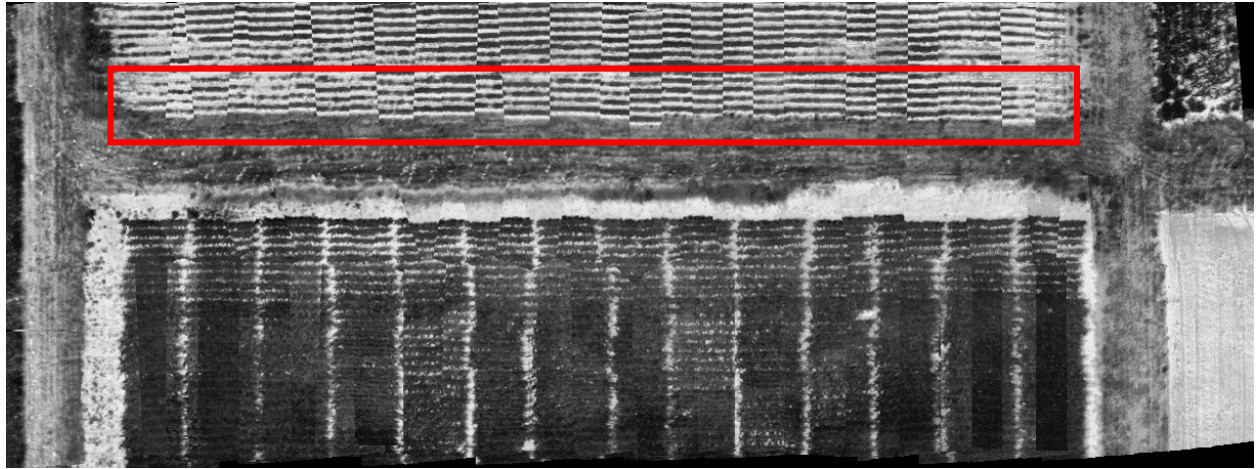
1.1 Background

Advances in technologies, paired with inexpensive hardware options, have increased the use of imaging platforms. A variety of imaging platforms are used to obtain 3D information such as static and wheel-based ground systems, manned and unmanned aerial systems, and small and large spaceborne systems. In addition to a variety of imaging platforms, there is also a wide range of imaging sensors onboard the system. Imaging platforms can include frame cameras, line cameras, LiDAR (Light Detection and Ranging), and radar sensors. Imaging platforms are designed for a diverse range of applications. Infrastructure monitoring, precision agriculture, disaster relief, emergency management, and defense are among some of the leading industries taking advantage of accurate 3D spatial information from imaging platforms. There are a wide range of platforms, sensors, and applications all with a common goal of obtaining useful spatial information and achieving it as quickly, inexpensively, and accurately as possible. Unmanned Aerial Vehicles (UAVs) equipped with Global Navigation Satellite System/Inertial Navigation System (GNSS/INS) and imaging sensors accomplish these goals. UAV-based GNSS/INS-assisted imaging systems are relatively low-cost compared to alternative methods such as wheel-based mobile mapping and manned aerial mapping. Many applications rely on UAV imaging systems not only because of their high accuracy but also for their relatively low-cost and timeliness. A UAV-based GNSS/INS-assisted imaging system is comprised of the UAV, an imaging sensor, and a GNSS/INS unit. For UAV-based imaging systems to have accurate geopositioning capability, special attention must be paid to calibration. Geometric system calibration focuses on the integration of the system as a whole. This includes estimating internal characteristics and system mounting parameters as well as time delay in the system, known as spatial and temporal calibration, respectively. In recent years, spatial system calibration has become a focus of study. Describing the differences between the position and orientation of the GNSS/INS body and camera frame via the lever arm components and boresight angles is key to system calibration. However, even with accurate mounting parameters, precise time tagging and temporal calibration is essential for accurate derivation of 3D spatial information. Accurate time synchronization between the imaging sensor and GNSS/INS unit is an important part of this integration. For consumer-grade systems, a

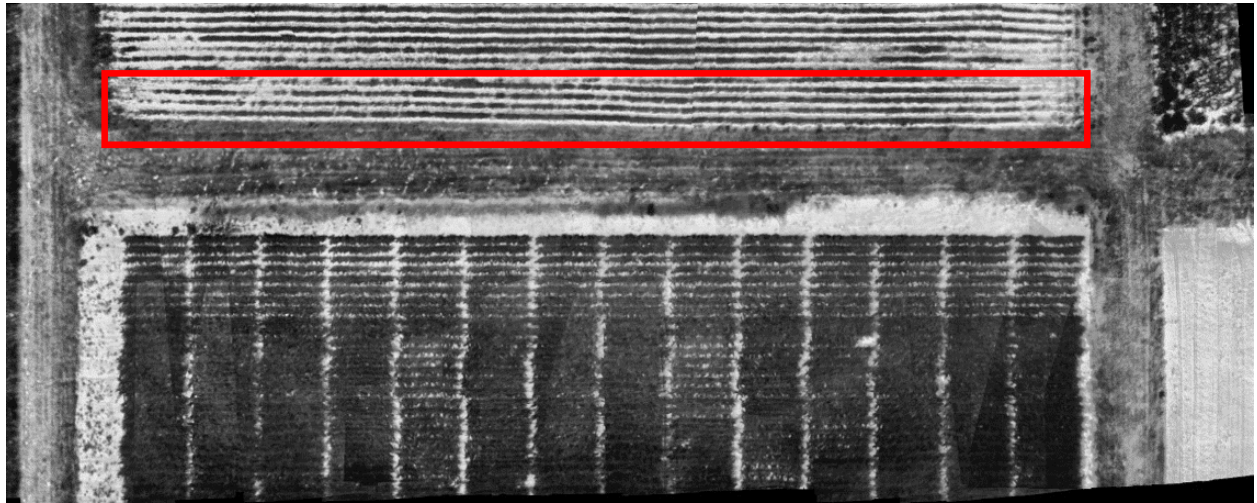
time delay between image mid-exposure and the corresponding GNSS/INS event recording often exists and 3D spatial accuracy will be greatly degraded if this time delay is not taken into account. In this dissertation, ‘consumer-grade’ refers to cameras that require system calibration by the user instead of by the manufacturer or other high-end laboratory settings and UAV systems that are equipped with relatively low-cost GNSS/INS units. Some research has been completed on temporal calibration. However, past research has yet to address temporal calibration that can be implemented as a one-step procedure achieving acceptable absolute accuracy without the use of ground control points (GCPs) with options for both with or without bundle adjustment software modifications. In addition, past research has yet to apply temporal calibration for UAV line camera systems. Furthermore, research has not been conducted on a fully-automated spatial and temporal system calibration for UAV frame and line camera systems.

1.2 Challenges in System Calibration of Consumer-Grade Sensors

Geometric system calibration is crucial for obtaining accurate 3D spatial information from remote sensing imaging platforms. Many current applications of remote sensing rely on consumer-grade imaging platforms for their needs. In addition to classical spatial system calibration, many consumer-grade sensors also need temporal calibration for accurate 3D reconstruction. When time synchronization is not addressed and a time delay between the mid-exposure and GNSS/INS event marker exists, inaccuracy occurs. As an example, an orthophoto generated using estimated system calibration parameters which did not include any time delay compensation and the same orthophoto generated when the time delay was accounted for is shown in Figure 1.1a and 1.1b, respectively. This system was found to have a time delay between the GNSS/INS event markers and corresponding mid-exposure times and not estimating the time delay resulted in extreme misalignments in the orthophoto generated. Although some research has focused on temporal calibration, there has yet to be an approach that can be applied to both frame and line camera systems while also being platform and sensor agnostic. Furthermore, there is also a need for spatial and temporal calibration that does not require expensive and time-consuming GCPs. Lastly, manually measuring tie points for system calibration is extremely time consuming and requires expertise in image interpretation. There has yet to be an approach that can incorporate automatically-derived tie points and still accurately estimate system parameters including time delay for frame and line camera systems without the use of GCPs.



(a)



(b)

Figure 1.1 (a) Orthophoto generated without (a) and with (b) considering time delay

1.3 Research Objectives

The following research objectives are meant to address the current challenges and gaps in geometric system calibration for frame and line camera systems. The objectives include the development of two new system calibration approaches – direct and indirect – that will accurately estimate time delay during system calibration. Furthermore, this research aims to derive optimal flight configurations for frame and line camera systems such that system parameters can be accurately and simultaneously estimated without the use of GCPs. Lastly, the research objectives

include the development of a fully-automated system calibration with time delay estimation for frame and line camera systems. More specifically, research objectives include:

1. Frame Cameras – Develop new strategies for time delay estimation during system calibration for UAV-based, GNSS/INS-assisted imaging systems
 - Incorporates a modified mathematical model to include time delay as an unknown system parameter during the bundle block adjustment procedure for frame camera systems
 - Establishes the optimal flight configuration for frame camera systems such that system parameters can be estimated as accurately as possible without the use of GCPs
 - For users without capability of updating software, provides an alternative for accurately estimating time delay for system calibration in frame camera systems
2. Line Cameras – Introduce spatial and temporal calibration for UAV-based, GNSS/INS-assisted line camera imaging systems
 - Incorporates a modified mathematical model to include time delay as an unknown system parameter during the bundle block adjustment procedure for line camera systems
 - For users without capability of updating software, provides an alternative for accurately estimating time delay for system calibration in line camera systems
 - Establishes the optimal flight configuration for line camera systems such that system parameters can be estimated as accurately as possible without the use of GCPs
3. Develop a fully automated spatial and temporal calibration for frame and line camera systems
 - Successfully extracts tie point features automatically for both frame and line camera systems
 - Incorporates a large amount of automatically-derived tie points into the bundle adjustment with self-calibration

1.4 Dissertation Outline

Chapter 2 contains a comprehensive literature review of related work. First, an overview of the different type of system calibration is presented. This section is followed by a discussion of previous work in system calibration. Next, past research dealing with time delay issues with hardware solutions are presented. Lastly, mitigating time delay issues with software solutions are discussed. Chapter 3 introduces two new strategies for time delay estimation during system calibration for UAV-based GNSS/INS assisted frame camera imaging systems. Chapter 4 presents system calibration while estimating time delay for UAV-based GNSS/INS assisted line camera systems. Chapter 5 introduces a fully-automated approach for system calibration while estimating time delay for line camera systems. Note that this dissertation is constructed as an article-based dissertation, which is a collection of published (or will be published) research articles. Chapters 3, 4, and 5 have their own abstract, introduction, related work, methodology, dataset description, experimental results, and conclusions. As chapters 3, 4, and 5 are meant to be stand alone, they have overlap in some of the sections, particularly in the literature review/related work and dataset descriptions sections. Chapter 6 includes the conclusions and recommendations for future work.

2. LITERATURE REVIEW

2.1 Overview

Imaging systems used to obtain accurate 3D spatial information require geometric calibration. There has been a wide variety of calibration research over the years. Geometric system calibration can be categorized into two primary areas of research: spatial and temporal. Spatial calibration accurately estimates both internal characteristics and mounting parameters of the system. Temporal calibration eliminates time delay between the timestamps of the image exposure epoch and the corresponding GNSS/INS position and orientation timestamps. Some spatial calibration research focuses specifically on internal sensor calibration, such as interior orientation parameters, while others focus on system calibration which can include internal orientation parameters as well as mounting parameters and time delay between the imaging sensor and GNSS/INS system. Hardware and software solutions have been introduced in an effort towards time synchronization issues. This literature review first presents previous research on spatial system calibration. A review of time synchronization with hardware implementations are then discussed. Lastly, spatial and temporal system calibration with software solutions are reviewed.

2.2 Spatial System Calibration

Spatial system calibration has been thoroughly researched over the years. Much of the system calibration research has been focusing on spatial system parameters and neglects the temporal complexity of the systems. The focus of this dissertation is on both spatial and temporal calibration. However, it is important review past work on spatial only system calibration to highlight current gaps. The methodology behind camera calibration, either completed by manufactures in a laboratory setting or through a bundle adjustment with self-calibration, is well-known [1]. For example, Furukawa and Ponce [2] presented camera calibration from multi-view stereo using bundle adjustment. Weng et al. [3] focused on camera calibration specifically for distortion models which include radial, decentering, and thin prism distortions. Others researched bundle adjustments with self-calibration using detected features. Rathnayaka et al. [4] presented calibration field-of-view stereo camera system using embedded checkerboard patterns. Habib et al. focused on camera and LiDAR self-calibration using straight lines and planar patches,

respectively [5, 6]. In recent years, system calibration has become a focus of study. Describing the differences between the position and orientation of the GNSS/INS body frame and camera frames is key to system calibration. Ravi et al. [7] focused on simultaneous system calibration of a multi-LiDAR multicamera mobile mapping platform. Also, boresight calibration of push-broom hyperspectral cameras and LiDAR UAV platforms has been researched [8, 9]. Both the interior camera calibration and system mounting parameter calibration has been thoroughly researched. Both manual and automated system calibration has been achieved on a variety of systems and sensors. However, none of the research described above has also incorporated a robust temporal calibration in their solution.

2.3 Hardware Time Synchronization Solutions

For GNSS/INS-assisted imaging systems, the GNSS/INS information gives prior information about the position and orientation of the unit at the time of exposure. It is assumed that the recorded timestamp of the image exposure corresponds to the recorded event marker of the GNSS/INS unit. Using the recorded event marker of the GNSS/INS unit, the position and orientation is derived and assumed to be the position and orientation of the platform at the moment of exposure. However, this assumption does not always hold true. Hardware solutions have been researched for time synchronization as a way to mitigate time delay in imaging systems. Hardware solutions consist of modifications and additions to the imaging sensor and/or GNSS/INS system. One particular time synchronization issues that arises is the assumption made that when a camera receives a triggering signal to capture an image, that the camera captures the image instantaneously. However, a delay can exist from when the camera receives the signal to capture an image and when the camera actually captures the image, known camera response time. Rehak and Skaloud [10] used an optical clock to determine the camera response time delay using LED bar-graphs. The optical clock sends a triggering signal to the camera to capture and image at an optional interval and begins counting with a graphical clock. The camera then receives that signal and takes images of the optical clock counter. The camera response time delay can then be estimated based on the count of the optical clock of when it sent the triggering signal to the camera and when the camera actually took the image. The camera lag delay is then known. This approach assumes the time delay to be constant for future uses. Elbahnasawy and Habib [11] introduced two hardware solutions to establish synchronization among different sensors, such as the recorded exposure time

and the actual mid-exposure time. The authors discussed the simulated feedback approach, which uses a triggering system (Raspberry Pi Module) to send a signal to both the camera and the GNSS/INS unit simultaneously. A diagram of the simulated feedback approach is shown in Figure 2.1. The hypothesis of the simulated feedback approach is that the camera would capture the image at the same time the triggering signal is received. However, a camera does not capture an image instantaneously once the triggering signal is received. Therefore, the simulated feedback approach ignores the camera response time delay. The simulated feedback approach, where a triggering signal is sent to both the camera and an optical clock, and the optical clock counting method can be combined to estimate the camera response time delay. A diagram of the simulated feedback approach combined with the optical clock method is shown in Figure 2.2.

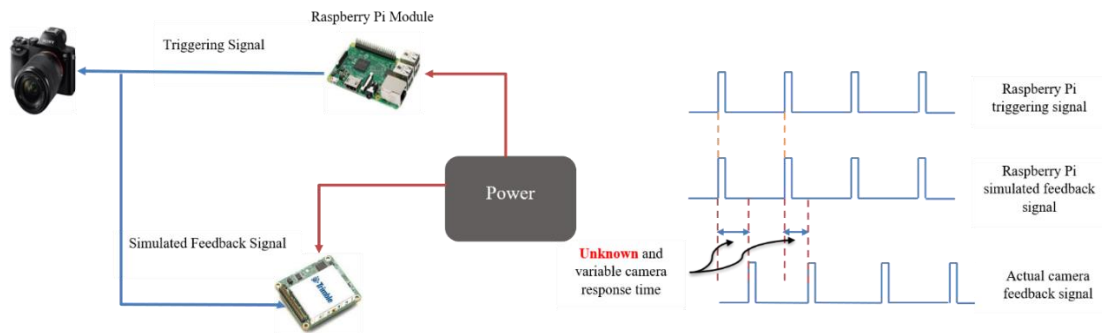


Figure 2.1 Illustration of Simulated Feedback Approach Diagram

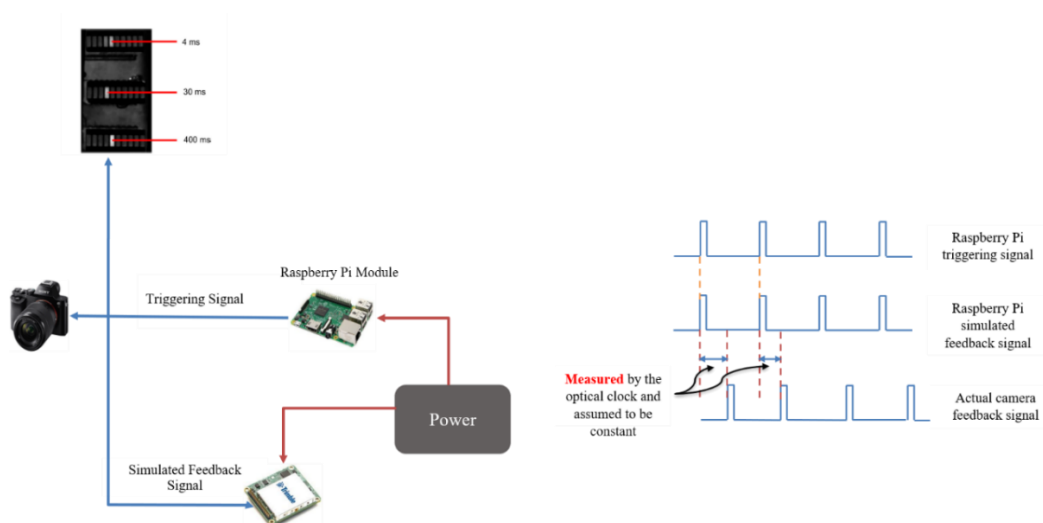


Figure 2.2 Illustration of Simulated Feedback Approach Combined with the Optical Clock Method

Elbahnasawy and Habib [11] second approach, direct feedback, attempted to mitigate this camera response time delay further. The direct feedback approach utilizes the camera flash hot-shoe to generate a signal at the time the image is captured. This camera feedback signal is then sent to the GNSS/INS unit onboard, and a corresponding event time is recorded. An illustration of the direct feedback approach is presented in Figure 2.3. One limitation to the direct feedback approach is that it assumes the hot-shoe flash signal corresponds exactly to the mid-exposure time. This cannot be assumed, and therefore a camera response time delay would still exist. Hardware can reduce the effects of time delay, however it has shown to be difficult to record the actual mid-exposure time of the image. Hardware solutions also require technical knowledge and expertise to implement which may not be an option for all users and applications.

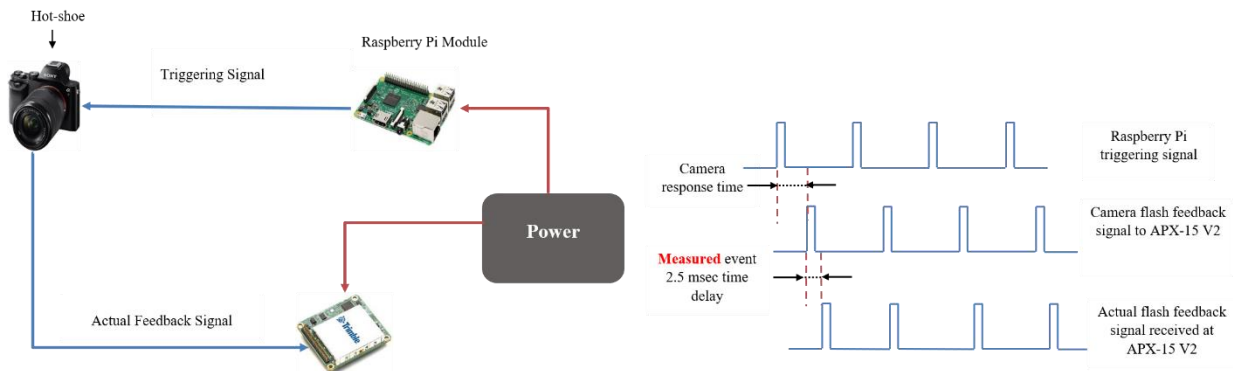


Figure 2.3. Illustration of Direct Feedback Approach

2.4 Spatial and Temporal System Calibration: Software Time Delay Solutions

Software solutions for temporal calibration can be faster and less expensive than hardware modification solutions. Recent software solutions for time delay estimation in imaging systems can be characterized into two categories. The first is one-step procedures that require a modification to bundle adjustment code. The second is two-step procedures that do not need modification to existing bundle adjustment code, but require two different independent adjustments.

Chiang et al. [12] proposed a calibration method to estimate the magnitude of exposure time delay for a UAV-based imaging system. The authors introduced a two-step approach for estimating time delay. The interior orientation parameters (IOPs) are initially estimated through a camera calibration process. In the first step, the exterior orientation parameters (EOPs) are estimated through indirect geo-referencing using GCPs. The differences in position and orientation between the EOPs and the interpolated trajectory from the on-board position and orientation system (POS) are derived. In the second step, the differences are then used in their calibration algorithm to solve for lever arm components, boresight angles, and time delay. Finally, the authors used the calibration parameters to perform direct geo-referencing applications without the need for GCPs. The results showed that by implementing the proposed calibration algorithm, a direct geo-positioning horizontal accuracy of 8 m at a flying height of 600 m and a 3D accuracy of 12 m can be achieved. The GSD while at 600 m flying height was 20 cm, and the camera had a pixel size of 0.0064 mm. Furthermore, the authors showed that the proposed calibration algorithm improved results by about 10% compared to traditional calibration. One limitation of the proposed algorithm is that a two-step process is needed to produce results. EOPs are first derived through indirect geo-referencing with the help of GCPs, and the difference in position and rotation between the EOPs and the interpolated GNSS/INS solutions is calculated. Next, the calibration is completed by solving for mounting parameters and time delay. The algorithm also assumes that the rotation of the vehicle does not change during this time discrepancy. In their study, the measured time delay was between -0.107 and -0.227 s and the inertial measurement unit (IMU) rotation matrix was assumed to be constant during the delay. This assumption may not be valid, specifically when using lightweight UAV systems. Another disadvantage of this study is that it was sensitive to imaging/GCP/tie point configuration within the indirect geo-referencing step. Lastly, this study neglected the consideration of a suitable flight configuration for estimating time delay and ignored potential correlation among the EOPs and other unknowns.

Gabrlík et al. [13] proposed a similar two-step approach to that of Chiang et al. [12] for system calibration for estimating offset in lever arm, offset in GNSS/INS base station, and time delay for a UAV-based imaging system. In the first step of their approach, EOPs are estimated through indirect geo-referencing using Agisoft Photoscan Professional software [14]. The positional components of the EOPs are then considered the true positions of the images. Finally, the difference between the derived position from the GNSS receiver and the true position of an image

is considered as a function of the system parameters mentioned above. Similar to Chiang et al., this approach depends on the availability of GCPs to estimate ground truth for camera positions. However, compared to Chiang et al. [12] even when taking into consideration the differences in platform, sensor, and flying height, this approach did produce more accurate results, with RMSE in the XY component of 3.3 cm and 2.5 cm in the Z component.

Blazaquez, M. [15] introduced a new approach for one-step ‘spatio-temporal’ calibration of multi-sensor systems. This approach focused on modifying the sensor model to include a time synchronization parameter. The approach uses the GNSS/INS-based linear and angular velocities to compute the displacement and orientation differences in estimating the time delay. Instead of solving for boresight angles, the author included a relative model that used the fact that if the sensor and IMU are rigidly attached, the relative rotation between two epochs is the same for both the sensor and the IMU. The author discussed the importance of varying linear velocity throughout the flight configuration for estimating the time delay parameter. However, because this specification was not met in their data collection, the data was manipulated to simulate strips being flown at different velocities. The absolute ‘spatio-temporal’ model produced RMS accuracy for checkpoints in the 25–35 mm range. The approach also estimated the time synchronization parameter at the tenth of a millisecond precision level. The experiments relied on GCPs for accurate estimates of system calibration parameters, including time delay.

Rehak and Skaloud [10] worked on time synchronization of consumer cameras on micro aerial vehicles (MAVs). The author’s MAV system consisted of a Sony sensor that was initially modified to compensate for time synchronization issues between the camera and GNSS by using the direct feedback approach. The authors investigated two different methods for determining time delay within their system. The first method was an analysis of residuals between the observed camera positions and those estimated by indirect geo-referencing, which is a two-step process. The second method was a one-step approach to modify the mathematical model to include time delay as a parameter in the bundle adjustment. The second method used in their absolute spatio-temporal model, with position, rotation, linear velocity, and angular velocity as observations. Both of these methods assume access to the position and velocity data from the GNSS/INS unit. A heuristic optimal flight configuration for estimating time delay was recommended. First, as part of the optimal configuration for system calibration while considering time delay, it was suggested that the lever arm be determined in a laboratory calibration, due to the correlation with the time delay.

The overall optimal flight configuration then suggested that there must be a strong block configuration with both GNSS/INS in-flight data and ground control, high forward and side lap, variations in flying height and linear and angular velocities, and obliquity in the imagery. The authors tested the validity of the methods through the evaluation of checkpoints. During the evaluation experiment, nine checkpoints were used in an integrated sensor orientation (ISO) with absolute aerial position observations. The results of this configuration showed an RMS of 56, 26, 54 mm in the X, Y, Z components, respectively, when the time events were corrected for a time delay of -6.2 ms. The interior orientation parameters and lever arm components were estimated in a separate calibration. The estimated time delay parameter ranged from -9.2 to -1.9 ms for the different methods.

2.5 Summary

Traditional spatial system calibration has been thoroughly covered by past research. There has been focus on calibration for the internal characteristic of the sensor as well as the system mounting parameters. There has also been focus on self-calibration using automatically-derived tie points. However, for consumer-grade systems, only focusing on the spatial system calibration neglects the time synchronization of the platform that is essential for accurate 3D reconstruction. Hardware time synchronization solutions have been researched to address this gap. However, hardware solutions require additions or modifications to the imaging platform. These additions or modifications require technical expertise and knowledge to implement. Furthermore, previous time synchronization hardware solutions were not capable of estimating or removing the entire camera response time delay without assuming this delay to be constant. Software solutions have also been implemented in efforts to mitigate time delay in consumer-grade imaging systems. However, previous software solutions required two-step processes, neglected to consider that the orientation of the platform may change during the time delay, and did not present suitable flight configurations for estimating time delay, which then ignore correlations between EOPs and other unknowns. Furthermore, all of the previous software solutions used GCPs in their system calibration to estimate time delay. In addition, temporal calibration has not been performed on consumer-grade line camera imaging platforms. Lastly, all previous temporal calibration work is performed with time consuming manually-measured tie points. This dissertation is intended to address these gaps and challenges. This research aims to develop two new system calibration

approaches – direct and indirect – that will accurately estimate time delay during system calibration. The direct approach is developed for both frame and line camera systems without the need for GCPs. The indirect approach is developed to allow flexibility for users to perform system calibration with time delay estimation without the capability of modifying existing bundle adjustment software. Optimal flight configurations are derived for frame and line camera systems such that system parameters can be accurately and simultaneously estimated without the use of GCPs. Lastly, a fully-automated system calibration with time delay estimation is developed for frame and line camera systems and intended to accurately estimate system parameters without the use of GCPs.

3. FRAME CAMERAS – NEW STRATEGIES FOR TIME DELAY ESTIMATION DURING SYSTEM CALIBRATION FOR UAV-BASED GNSS/INS-ASSISTED IMAGING SYSTEM

The research article, “New Strategies for Time Delay Estimation during System Calibration for UAV-Based GNSS/INS-Assisted Imaging Systems”, was published in the 2019 Remote Sensing journal.

LaForest, L.; Hasheminasab, S.M.; Zhou, T.; Flatt, J.E.; Habib, A. New Strategies for Time Delay Estimation during System Calibration for UAV-Based GNSS/INS-Assisted Imaging Systems. Remote Sens. 2019, 11, 1811.

Abstract: The need for accurate 3-D spatial information is growing rapidly in many of today’s key industries such as precision agriculture, emergency management, infrastructure monitoring, and defense. Unmanned Aerial Vehicles (UAVs) equipped with Global Navigation Satellite System/Inertial Navigation System (GNSS/INS) and consumer-grade digital imaging sensors are capable of providing accurate 3-D spatial information at a relatively low-cost. However, with the use of consumer-grade sensors, system calibration is critical for accurate 3-D reconstruction. In this study, ‘consumer-grade’ refers to cameras that require system calibration by the user instead of by the manufacturer or other high-end laboratory settings as well as relatively low-cost GNSS/INS units. In addition to classical spatial system calibration, many consumer-grade sensors also need temporal calibration for accurate 3-D reconstruction. This study examines the accuracy impact of time delay in the synchronization between the GNSS/INS unit and cameras on-board UAV-based mapping systems. After reviewing existing strategies, this study presents two approaches (direct and indirect) to correct for time delay between GNSS/INS recorded event markers and actual time of image exposure. Our results show that both approaches are capable of handling and correcting this time delay, with the direct approach being more rigorous. When a time delay exists and the direct or indirect approach is applied, horizontal accuracy of 1-3 times the ground sampling distance (GSD) can be achieved both without the use of any ground control points (GCPs) or adjusting the original GNSS/INS trajectory information.

3.1 Introduction

There is an increasing use of UAV-based GNSS/INS-assisted imaging systems among industries such as precision agriculture, infrastructure monitoring, emergency management, and defense. In particular, UAV imaging systems used in precision agriculture have a variety of applications such as monitoring crops, estimating crop yield and best crop placement, and improving land cover classification. Use of UAVs in agricultural applications has expanded rapidly in recent years due to their relatively low cost and improved spatial and temporal resolution when compared to traditional satellite and manned aircraft imagery [16]. In addition, it is possible to equip UAVs with a variety of imaging sensors. These factors have increased the effectiveness of UAVs as a tool for precision agriculture and crop monitoring [17-23]. Additionally, RGB frame imagery can be useful for automating hyperspectral data orthorectification process, allowing prediction of biomass and other phenotypic factors [24]. Thermal imagery has been used to estimate soil moisture, monitor evapotranspiration, and improve land cover classification [25-29]. Remotely sensed imagery has proven its usefulness in a wide-range of agricultural environments. For many of these applications, remotely sensed imagery must be geo-referenced accurately. Proper system calibration is vital to providing accurate and actionable data for those applications.

System calibration of a UAV-based GNSS/INS-assisted imaging system deals with both spatial and temporal aspects. Spatial system calibration aims at estimating both internal characteristics of the camera, known as camera calibration, as well as system mounting parameters. Such parameters include principal point coordinates, principal distance, and distortion parameters for the internal camera characteristics and lever arm components and boresight angles for the integration between GNSS/INS and multiple imaging sensors. The methodology behind camera calibration, either completed by manufactures in a laboratory setting or in a bundle adjustment with self-calibration, is well-known [1, 4-5, 30]. In recent years, system calibration has become a focus of study. Describing the differences between the position and orientation of the GNSS/INS body frame and camera frames, lever arm components and boresight angles, is key to system calibration. Lever arm and boresight calibration processes have also been well-established by several research groups. Li et al. [8] worked on boresight calibration of both a mobile and UAV LiDAR system using strip adjustment. While Habib et al. [9] completed rigorous boresight calibration for a UAV platform with a hyperspectral camera equipped with GNSS/INS. Costa and Mitishita [31] focused on integrating photogrammetric and LiDAR datasets to improve sensor

orientation information. However, even with accurate mounting parameters, precise time tagging between the imaging sensor and GNSS/INS unit is essential for accurate derivation of 3D spatial information. For consumer-grade systems, a time delay between image exposure and the corresponding GNSS/INS event recording might exist and 3D spatial accuracy will be greatly degraded if this time delay is not taken into account. Throughout this manuscript, we will refer to the term “event marker”, which is used to indicate the time of exposure based on feedback signals received by the GNSS/INS unit from the camera. When time synchronization is not addressed and a time delay between the mid-exposure and GNSS/INS event marker exists, inaccuracy occurs. As an example, an orthophoto generated using estimated system calibration parameters which did not include any time delay compensation, shown in Figure 3.1a., and the same orthophoto generated when the time delay was accounted for using the direct approach, which will be presented later in this paper is shown in Figure 3.1b. In the highlighted area in Figure 3.1a, there are significant misalignments in the generated orthophoto. However, after time delay was compensated for within the bundle adjustment process, shown in Figure 3.1b, the generated orthophoto in the same highlighted area as Figure 3.1a. shows a smooth alignment.

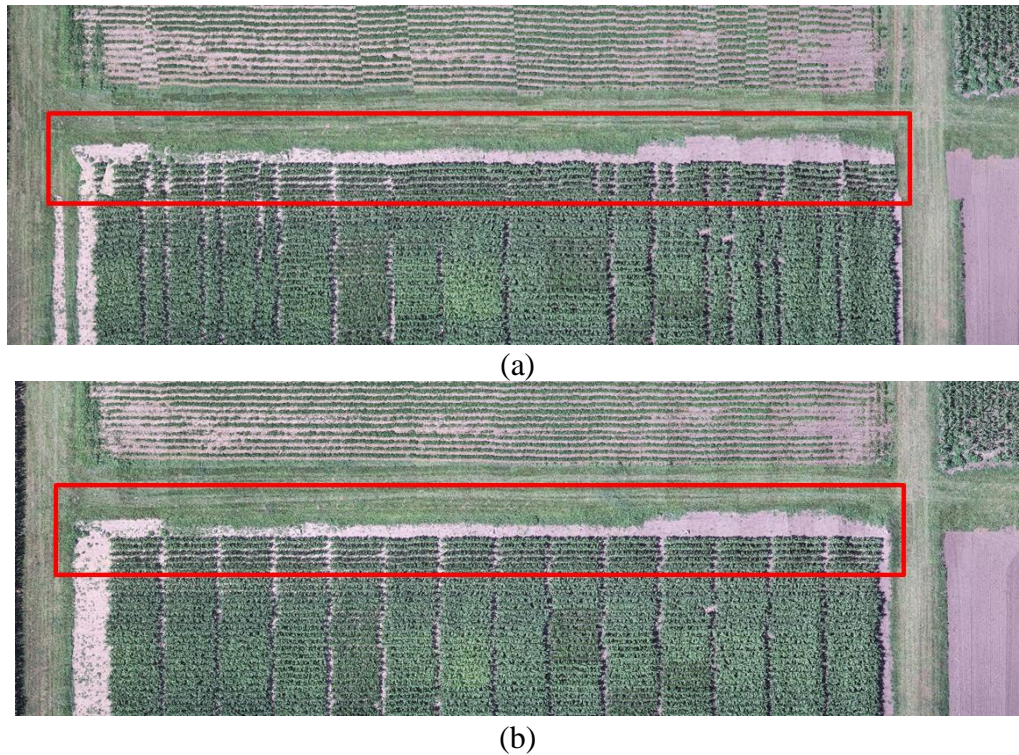


Figure 3.1 (a) Orthophoto generated while ignoring the time delay during calibration. (b) Orthophoto generated with time delay accounted for during calibration.

In addition to proper system calibration, the geo-referencing technique used in system parameters estimation process are also important for providing accurate 3-D information. There are a variety of techniques used for geo-referencing which depend greatly on the application purpose, availability of resources, and accuracy requirements of the project. Direct and indirect geo-referencing are two main techniques used. Indirect geo-referencing uses aerial triangulation with the help of ground control points (GCPs) to accurately estimate system parameters. Indirect geo-referencing produces high accuracy but is costly and time consuming because of the need for GCPs in the triangulation [32-33]. On the other hand, direct geo-referencing uses a simple intersection adjustment and eliminates the need for GCPs but can also degrade the overall accuracy of the system calibration. Several recent studies focus on direct geo-referencing and the reduction or elimination of GCPs [34-36]. The accuracy of direct geo-referencing depends greatly on the onboard GNSS/INS unit and its integration within the rest of the imaging system and without GCPs, degradation of geopositioning is a concern. However, the reduction or elimination of GCPs while ensuring improved accuracy is a valuable prospect, considering it reduces cost, time, and equipment requirements when collecting data.

This study focuses on system calibration of UAV-based GNSS/INS-assisted imaging systems, specifically studying calibration strategies capable of estimating time delay between GNSS/INS event markers and the image mid-exposure time. After review of existing strategies, we detail two approaches – direct and indirect – to solve for and correct this time delay. The direct approach uses a modified mathematical model to solve directly for the time delay in a bundle block adjustment. The direct approach modifies the bundle adjustment code for implementation. The indirect approach, on the other hand, exploits the correlation between the lever arm along the flying direction and the time delay – which follows from a less-than optimal flight configuration – as well the speed/time/distance relation to indirectly estimate time delay. The indirect approach exploits existing bundle adjustment code to estimate time delay. Section 2 focuses on related work while section 3 describes the methodology of the bundle block adjustment procedure, direct and indirect approaches, as well as optimal flight configuration for reliable estimation of the system calibration parameters. Section 4 focuses on the description of the UAV-based imaging systems and data used in this study in addition to experimental results and analysis. Lastly, section 5 provides conclusions and recommendations for future research.

3.2 Related Work

Imaging systems used for obtaining accurate 3D spatial information need calibration both within the sensor and between the sensor and remaining system units. There has been a wide variety of calibration research over the years. Some research focuses on the sensor calibration itself and does not include the system parameters such as in [3]. Whereas some research system calibration focuses not only the internal characteristics of a sensor but also the external and mounting parameters of the system as a whole [4, 5]. Identifying features in imagery is also essential for calibration [37]. Many works have used distinct points while others have used linear or planar features [5, 6]. The type of control data used in previous calibration ranges from ground-based surveyed points, on-board GNSS/INS sensors, and superior sensor sources such as LiDAR. The accuracy associated with these type of control data used in calibration is approximately 3mm for ground-based surveyed points, 8mm planimetric accuracy for on-board GNSS/INS points, and 25 cm planimetric accuracy for LiDAR derived control data [12, 13, 38]. Among this work, a variety of calibration parameters are of interest. As stated before, some are interested only in internal characteristics of a sensor while others are interested in full system calibration. Some of this research is strictly focused on the spatial calibration aspects of an imaging system and neglects to address the temporal calibration.

As consumer-grade sensors integrated with GNSS/INS units on-board UAVs become more popular options for geospatial applications, the need to accurately estimate any time delay between GNSS/INS event marker and mid-exposure time during system calibration becomes increasingly important. Both hardware and software solutions have been introduced in an attempt to mitigate this problem. Elbahnasawy and Habib [11] introduce two hardware solutions to establish the synchronization among different sensors such as the recorded exposure time and the actual mid-exposure time. The authors discuss the simulated feedback approach which uses a triggering system to send a signal to both the camera and the GNSS/INS unit simultaneously. The hypothesis of the simulated feedback approach is that the camera would capture the image at the same time the triggering signal is received. However, a camera does not capture an image instantaneously once the triggering signal is received. Therefore, the simulated feedback approach ignores the camera response time delay. Another hardware solution consists of using both a triggering signal, as described in the simulated feedback approach, and an optical clock to measure the camera response time [10]. The triggering signal is sent to the camera, GNSS/INS unit, and the optical

clock. The function of the signal from the optical clock also sends a signal to the camera at an optional interval and begins counting with a graphical clock. The camera takes images of the optical clock counter and image processing then determines the value displayed on the counter. The camera lag delay is then known. This approach assumes the time delay to be constant for future uses. Elbahnasawy and Habib's [11] second approach, the direct feedback, attempts to mitigate this camera response time delay further. The direct feedback approach utilizes the camera flash hot-shoe to generate a signal at the time the image is captured. This camera feedback signal is then sent to the GNSS/INS unit on-board and a corresponding event time is recorded. One limitation to the direct feedback approach is that it assumes the hot-shoe flash signal corresponds exactly to the mid-exposure time. This cannot be assumed and therefore a camera response time delay would still exist. Although hardware approaches can reduce the effects of time delay, it is shown to be difficult to record the actual mid-exposure. Furthermore, hardware modifications require both more time and monetary investment to implement. This may not be an option for all systems and applications. Therefore, others have investigated methods to measure time delay with software solutions. Recent software solutions for time delay estimation in imaging systems can be characterized in two categories. The first being one-step procedures that require a modification to bundle adjustment code. The second being two-step procedures that do not need modification to existing bundle adjustment code but require two different independent adjustments.

Chiang et al. [12] proposed a calibration method to compensate for and estimate the magnitude of exposure time delay for a UAV-based imaging system. The authors introduce a two-step approach for estimating time delay. The interior orientation parameters (IOPs) are initially estimated through a camera calibration process. Then in the first step, the exterior orientation parameters (EOPs) are estimated through indirect geo-referencing using GCPs. The differences in position and orientation between the EOPs and the interpolated trajectory from the on-board Position and Orientation System (POS) are derived. In the second step, the differences are then used in their calibration algorithm to solve for lever arm components, boresight angles, and time delay. Finally, the authors use the calibration parameters to perform direct geo-referencing applications without the need for GCPs. The results show that by implementing the proposed calibration algorithm, a direct geo-positioning horizontal accuracy of 8 m at a flying height of 600 m and a 3D accuracy of 12 m can be achieved. The GSD while at 600 m flying height was 20 cm and the camera had a pixel size of 0.0064 mm. Furthermore, the authors show that the proposed

calibration algorithm improved results by about 10% compared to traditional calibration. One limitation of the proposed algorithm is that a two-step process is needed – requiring two different independent adjustments – to produce results. EOPs are first derived through indirect geo-referencing with the help of GCPs and the difference in position and the rotation between the EOPs and the interpolated GNSS/INS solutions are calculated. Next, the calibration is completed by solving for mounting parameters and time delay. The algorithm also assumes that the rotation of the vehicle does not change during this time discrepancy. In their study, the measured time delay was between -0.107 and -0.227 s and the IMU rotation matrix was assumed to be constant during the delay. This assumption may not be valid, specifically when using light-weight UAV systems. Another disadvantage of this study is that it is sensitive to imaging/GCP/tie point configuration within the indirect geo-referencing step. Lastly, this study neglects the consideration of a suitable flight configuration for estimating time delay and ignores potential correlation among the EOPs and other unknowns.

Gabrlik et al. [13] proposed a similar two-step approach to that of Chiang et al. [12] for system calibration for estimating offset in lever arm, offset in GNSS/INS base station, and time delay for a UAV-based imaging system. In the first step of their approach, EOPs are estimated through indirect geo-referencing using Agisoft Photoscan Professional software [14]. Then, the positional component of the EOPs are considered as true position of the images. Finally, difference between the derived position from the GNSS receiver and the true position of an image is considered as a function of the system parameters mentioned above. Similar to Chiang et al. [12], this approach depends on the availability of GCPs to estimate ground truth for camera positions. However, compared to [12], even when taking into consideration the differences in platform, sensor, flying height this approach did produce more accurate results with RMSE in the XY-component of 3.3 cm and 2.5 cm in Z-component. In addition, the proposed strategy does not consider any rotation variation information when estimating time delay.

Blazaquez, M. [15] introduces a new approach for one-step ‘spatio-temporal’ calibration of multi-sensor systems. This approach focuses on modifying the sensor model to include a time synchronization parameter. The approach uses the GNSS/INS-based linear and angular velocities to compute the displacement and orientation differences in estimating the time delay. Instead of solving for boresight angles, the author includes a relative model that used the fact that if the sensor and IMU are rigidly attached, the relative rotation between two epochs is the same for both the

sensor and IMU. The author discusses the importance of varying linear velocity throughout the flight configuration for estimating the time delay parameter. However, because this specification was not met in their data collection, the data was manipulated to simulate strips being flown at different velocities. The absolute ‘spatio-temporal’ model produced RMS accuracy for checkpoints in the 25-35 mm range. The approach also estimated time synchronization parameter at the tenth of a millisecond precision level. The experiments rely on GCPs for accurate estimates of system calibration parameters including time delay.

Rehak and Skaloud [10] worked on time synchronization of consumer cameras on Micro Aerial Vehicles (MAVs). The author’s MAV system consisted of a Sony sensor that was initially modified to compensate for time synchronization issues between the camera and GNSS by using the direct feedback approach. The authors investigated two different methods for determining time delay within their system. The first method was an analysis of residuals between the observed camera positions and those estimated by indirect geo-referencing, which is a two-step process. The second method was a one-step approach to modify the mathematical model to include time delay as a parameter in the bundle adjustment. The second method uses their absolute spatio-temporal model with position, rotation, linear velocity, and angular velocity as observations. Both of these methods assume access to the position and velocity data from the GNSS/INS unit. A heuristic optimal flight configuration for estimating time delay was recommended. First, as part of the optimal configuration for system calibration while considering time delay, it was suggested to determine the lever arm in a laboratory calibration due to the correlation with the time delay. Then, the overall optimal flight configuration suggested that there must be a strong block configuration with both GNSS/INS in-flight data and ground control, high forward and side lap, variations in flying height and linear and angular velocities, and some obliquity in the imagery. The authors tested the validity of the methods through evaluation of checkpoints. During the evaluation experiment, 9 checkpoints were used in an integrated sensor orientation (ISO) with absolute aerial position observations. The results of this configuration showed an RMS of 56, 26, 54 mm in the X, Y, Z components, respectively when the time events were corrected for a time delay of -6.2 ms. The interior orientation parameters and lever arm components were estimated in a separate calibration. The estimated time delay parameter ranged from -9.2 to -1.9 ms for the different methods.

3.3 Methodology

The presented approach in this study proposes two one-step algorithms – direct and indirect. The direct approach computes the linear and angular velocities directly and does not rely on raw data from the IMU. Also, to ensure the highest possible accuracy, the direct approach does not assume that the platform rotation to be constant during the time delay period. The approaches are tested on systems with sensors both that are modified to incorporate the flash hot-shoe time synchronization – which significantly reduces the time delay – and also a sensor that only makes use of the manufactured internal “frame sync” option. Furthermore, the approaches presented are tested and evaluated in an integrated sensor orientation (ISO) and direct geo-referencing adjustments, without the need for GCPs. Lastly, an optimal flight configuration is derived so that one can estimate the system parameters, including the lever arm components, boresight angles, and time delay simultaneously. The optimal flight configuration presented maximizes the impact of biases or any possible errors in the system parameters while also decoupling those parameters.

3.3.1 Conceptual Basis of Bundle Block Adjustment

For many photogrammetric applications, the goal is to gain accuracy while decreasing required resources. The bundle block adjustment theory is a well-known method for improving geospatial precision and accuracy derivation from imagery by improving geometric configuration and increasing redundancy while reducing the quantity of GCPs [1]. The bundle adjustment aims to ensure best accuracy and precision of the reconstructed object space using minimal control. A graphical illustration of the bundle adjustment target function is introduced in Figure 3.2. It promotes flexibility among solvable unknown parameters to suit individual user needs, and in more recent years, it has been shown to be platform agnostic and capable of simultaneously combining a variety of sensors. Ravi et al. [7] used bundle adjustment theory to simultaneously perform system calibration of a multi-LiDAR/multi-camera mobile mapping platform. Habib et al. [5] demonstrated the use of bundle adjustment for self-calibration of line cameras using linear features detected in multiple datasets. Whether using frame or line cameras, or combining multiple sensors on a single/multiple platform(s), the mathematical model and overall least squares adjustment implementation of bundle adjustment is the same.

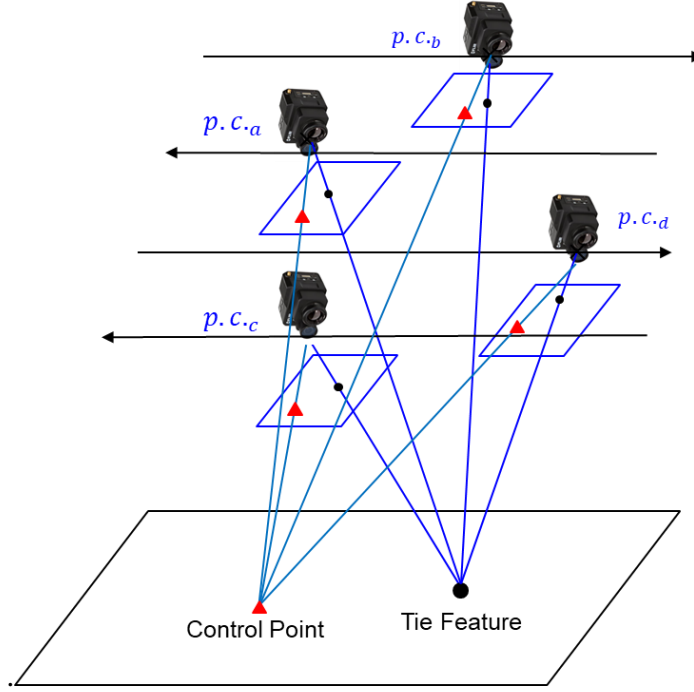


Figure 3.2. Conceptual basis of bundle block adjustment

A UAV-based GNSS/INS-assisted imaging system involves three coordinate systems – a mapping frame, an IMU body frame, and a camera frame. The mathematical model of the collinearity principle – which describes the collinearity of the camera perspective center, image point, and corresponding object point – is graphically illustrated and mathematically introduced in Figure 3.3 and Equation (3.1), respectively. The following notations are used throughout this study: a vector connecting point ‘b’ to point ‘a’ relative to a coordinate system associated with point ‘b’ is represented as r_a^b and a rotation matrix transforming from coordinate system ‘a’ to coordinate system ‘b’ is represented as R_a^b .

$$r_I^m = r_{b(t)}^m + R_{b(t)}^m r_c^b + \lambda(i, c, t) R_{b(t)}^m R_c^b r_i^{c(t)} \quad (3.1)$$

Where:

r_I^m : ground coordinates of the object point I

$r_i^{c(t)} = \begin{bmatrix} x_i - x_p - dist_{x_i} \\ y_i - y_p - dist_{y_i} \\ -c \end{bmatrix}$: vector connecting perspective center to the image point

x_p, y_p : principal point coordinates

c : principal distance

$dist_{x_i}, dist_{y_i}$: distortion in x and y directions for image point i

t : time of exposure

$r_{b(t)}^m$: position of IMU body frame relative to the mapping reference frame at time t derived from the GNSS/INS integration process

$R_{b(t)}^m$: rotation matrix from the IMU body frame to the mapping reference frame at time t derived from GNSS/INS integration process

r_c^b : lever arm from camera to IMU body frame

R_c^b : rotation (boresight) matrix from camera to IMU body frame

$\lambda(i, c, t)$: scale factor for point i captured by camera c at time t

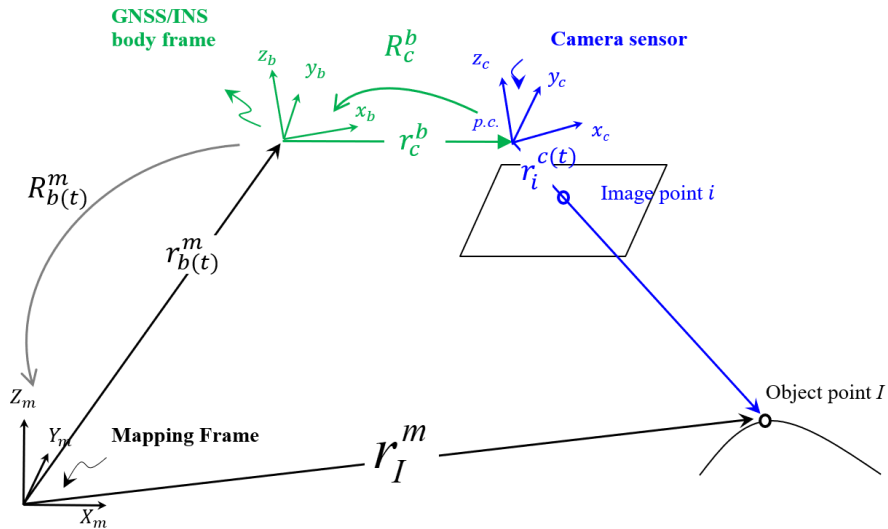


Figure 3.3 Illustration of collinearity equations

Reformulating Equation (3.1), one can represent image coordinates as a function of the GNSS/INS position and orientation, ground coordinates of GCPs/tie points, lever arm components, and the boresight matrix as shown in Equation (3.2).

$$r_i^{c(t)} = \frac{1}{\lambda(i, c, t)} R_b^c \left[R_m^{b(t)} [r_l^m - r_{b(t)}^m] - r_c^b \right] = \frac{1}{\lambda(i, c, t)} \begin{bmatrix} N_x \\ N_y \\ D \end{bmatrix} \quad (3.2)$$

Where:

$$\begin{bmatrix} N_x \\ N_y \\ D \end{bmatrix} = R_b^c \left[R_m^{b(t)} [r_l^m - r_{b(t)}^m] - r_c^b \right]$$

To eliminate the unknown scale factor $\lambda(i, c, t)$ from Equation (3.2), the first and second rows can be divided by the third one to produce equations (3.3a) and (3.3b) [1], which are nonlinear forms in the unknowns, including system calibration.

$$x_i - x_p - \text{dist}_{x_i} = -c \frac{N_x}{D} \quad (3.3a)$$

$$y_i - y_p - \text{dist}_{y_i} = -c \frac{N_y}{D} \quad (3.3b)$$

3.3.2 Direct Approach for Time Delay Estimation

The first strategy for time delay estimation introduced in this study is the direct approach where the time delay is directly estimated in a bundle adjustment with system self-calibration process. The previously discussed mathematical model is modified to incorporate the time delay parameter and is derived as explained below.

Given the position and orientation at t_0 , initial event marker time, the objective is to find the correct position and orientation at the actual mid-exposure time, t , by taking into account the time (delay), Δt , between actual exposure time and initial event marker time. It follows that the actual time of exposure equals to the initial event marker time plus the time delay, $t = t_0 + \Delta t$. Based on the collinearity equations (3.1), it is clear that a time delay between the mid-exposure and the recorded event marker by the GNSS/INS unit will directly affect the position $r_{b(t)}^m$ and orientation $R_{b(t)}^m$ of the body frame. Therefore, one must estimate the changes in position and orientation caused by the time delay. The position at the correct time, $r_{b(t)}^m$, can then be expressed by using the position at the initial event marker time tag and adding the displacement caused by the time delay, expressed in equation (3.4). The instantaneous linear velocity, $\dot{r}_{b(t_0)}^m$, at the initial

event marker time is needed to calculate the displacement. The instantaneous linear velocity is expressed in equation (3.5). It should be noted that the GNSS and IMU units typically have data rates of 10 and 200 Hz, respectively. The GNSS/INS integration process produces the position and orientation of the IMU body frame at a given time interval which is usually interpolated to that of the data rate of the IMU, which is 200 Hz in this study. Given this trajectory, we specify a time interval, dt , which we use to compute the instantaneous linear and later the angular velocity. The interpolation frequency chosen is controlled by the data rate of the IMU unit and the expected noise level in the derived trajectory. Choosing a very high frequency for the interpolation will magnify the impact of noise. The frequency of the interpolation process is balanced to consider both the data rate of the data acquisition system as well as reducing the impact of the noise in the derived trajectory.

$$r_{b(t)}^m = r_{b(t_0)}^m + \Delta t \dot{r}_{b(t_0)}^m \quad (3.4)$$

$$\dot{r}_{b(t_0)}^m = \frac{1}{dt} [r_{b(t_0+dt)}^m - r_{b(t_0)}^m] \quad (3.5)$$

Next, an expression for the orientation of the IMU body frame, $R_{b(t)}^m$, at the correct mid-exposure time can be derived. Deriving an expression for the orientation of the IMU body frame at the correct mid-exposure time enables the direct approach to handle rotation variation during the time delay. Here, we examine the changes in the rotation of the IMU body frame at different times. With the help of Figure 3.4, we can see that the rotation matrix at the correct exposure time, $R_{b(t)}^m$, can be derived from the rotation of the body frame at time t_0 as well as the angular velocity and time delay. The angular velocity is derived based on the rotation at time t_0 and rotation at time $t_0 + dt$ as shown in equation (3.6). More specifically, we can use the rotation at time t_0 and the rotation at time $t_0 + dt$ to derive the changes in the rotation angles denoted by $d\omega_b(t_0)$, $d\phi_b(t_0)$, and $d\kappa_b(t_0)$. These rotation changes along with the user-defined time interval, dt , can then be used to derive the angular velocity as per equation (3.7a-3.7c). Using the angular velocities and the time delay, the change in rotation caused by the existing time delay can be derived, shown in equation (3.8). It should be noted that an expression for the incremental rotation matrix is used in equation (3.8) since the angular change caused by the time delay are relatively small. Finally, using the IMU body orientation at the initial event marker time, expressed as $R_{b(t_0)}^m$, along with the rotation changes during the time delay, expressed as $R_{b(t_0+\Delta t)}^{b(t_0)}$, the IMU body orientation at

the actual exposure time, $R_{b(t)}^m$, can be derived as per equation (3.9). Substituting equations (3.4) and (3.9) in equation (3.1), the collinearity equations can be rewritten as in equation (3.10).

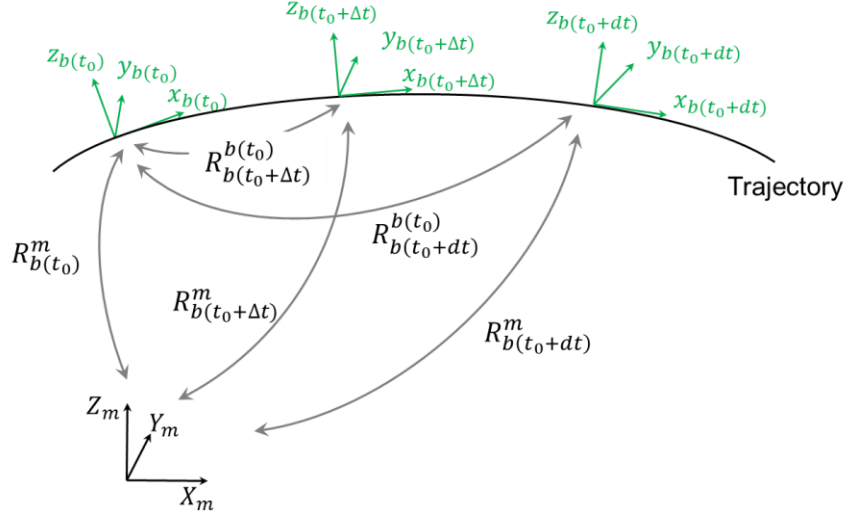


Figure 3.4 Establishing an expression for the correct IMU body frame orientation in the presence of time delay

$$R_{b(t_0+dt)}^{b(t_0)} = R_m^{b(t_0)} R_{b(t_0+dt)}^m = \text{Rotation}(d\omega_b(t_0), d\varphi_b(t_0), d\kappa_b(t_0)) \quad (3.6)$$

$$\dot{\omega}_b(t_0) = \frac{d\omega_b(t_0)}{dt} \quad (3.7a)$$

$$\dot{\varphi}_b(t_0) = \frac{d\varphi_b(t_0)}{dt} \quad (3.7b)$$

$$\dot{\kappa}_b(t_0) = \frac{d\kappa_b(t_0)}{dt} \quad (3.7c)$$

$$R_{b(t_0+dt)}^{b(t_0)} = \text{Rotation}(\dot{\omega}_b(t_0)\Delta t, \dot{\varphi}_b(t_0)\Delta t, \dot{\kappa}_b(t_0)\Delta t) \cong \begin{bmatrix} 1 & -\dot{\kappa}_b(t_0)\Delta t & \dot{\varphi}_b(t_0)\Delta t \\ \dot{\kappa}_b(t_0)\Delta t & 1 & -\dot{\omega}_b(t_0)\Delta t \\ -\dot{\varphi}_b(t_0)\Delta t & \dot{\omega}_b(t_0)\Delta t & 1 \end{bmatrix} \quad (3.8)$$

$$R_{b(t)}^m = R_{b(t_0)}^m R_{b(t_0+\Delta t)}^{b(t_0)} \quad (3.9)$$

$$r_i^{c(t)} = \frac{1}{\lambda(i,c,t)} R_b^c \left[R_{b(t_0)}^{b(t_0+\Delta t)} R_m^{b(t_0)} (r_I^m - r_{b(t_0)}^m - \dot{r}_{b(t_0)}^m \Delta t) - r_c^b \right] \quad (3.10)$$

The mathematical model is now modified so that the image coordinate measurements are a function of the trajectory information, IOPs, lever arm components, boresight angles, ground coordinates, and time delay. More specifically, during the least squares adjustment, time delay is treated as an unknown parameter. The initial value of time delay is set to zero. The first iteration is performed and the lever arm components, boresight angles, ground coordinates of tie points, and time delay are solved for. The time delay is applied to adjust the IMU body frame position and orientation for the next iteration, and the time delay is set back to zero before the next iteration. The iterations continue until the time delay estimate is approximately zero and the corrections to the other unknown parameters are sufficiently small, as illustrated by Figure 3.5.

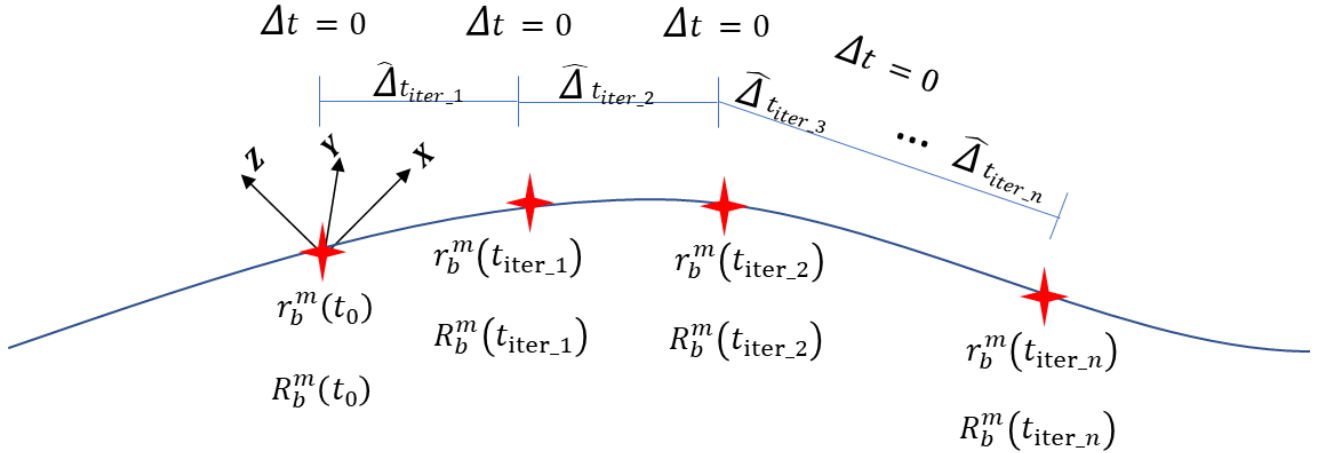


Figure 3.5 Illustration of the direct approach for time delay estimation within the bundle block adjustment with system self-calibration

3.3.3 Optimal Flight Configuration for System Calibration while Considering Time Delay

The objective of this section is to determine an optimal flight configuration which results in an accurate estimation of the system parameters, including the lever arm components, boresight angles, and time delay. The optimal flight configuration is the one that maximizes the impact of

biases or any possible errors in the system parameters while also decoupling those parameters. A rigorous approach of doing this is to derive the impact of biases in the system parameters on the derived ground coordinates. Bias impact analysis can be done by deriving the partial derivatives of the point positioning equation with respect to the system parameters. Equation (3.11) reformulates equation (3.10) to express the ground coordinates as a function of the measurements and system parameters. Partial derivatives are derived from equation (3.11).

For system calibration, the unknown parameters, denoted henceforth by x , consist of the lever arm components, $\Delta X, \Delta Y, \Delta Z$, boresight angles, $\Delta\omega, \Delta\phi, \Delta\kappa$, and time delay, Δt . Generalizing equation (3.11) to equation (3.12), we can see that the ground coordinate, r_I^m , is a function of the system parameters, x . Taking the partial derivatives of the collinearity equations with respect to each system parameter and multiplying by the discrepancy in the system parameters, δx , show which flight configuration produce a change in the ground coordinates, δr_I^m , as expressed in equation (3.13).

$$r_I^m = r_{b(t_0)}^m + \dot{r}_{b(t_0)}^m \Delta t + R_{b(t_0)}^m R_{b(t_0+\Delta t)}^{b(t_0)} r_c^b + \lambda(i, c, t) R_{b(t_0)}^m R_{b(t_0+\Delta t)}^{b(t_0)} R_c^b r_i^{c(t)} \quad (3.11)$$

$$r_I^m = f(x) \quad (3.12)$$

$$\delta r_I^m = \frac{\partial r_I^m}{\partial x} \delta x \quad (3.13)$$

Where:

$$\delta x = (\delta\Delta X, \delta\Delta Y, \delta\Delta Z, \delta\Delta\omega, \delta\Delta\phi, \delta\Delta\kappa, \delta\Delta t)$$

To simplify this analysis, we make a few assumptions. These assumptions are specifically made to simplify the derivation and the analysis of the bias impact is not affected if such assumptions are not met. It should be noted that deviations from these assumptions would have a more favorable effect on our ability to decouple the impact of various system parameters. We assume that the sensor is travelling with a constant attitude in the south-to-north and north-to-south directions. Throughout this manuscript we use double signs, \pm and \mp , to refer to the direction of the flight. The top sign pertains to the south-to-north flight and the bottom sign refers to the north-to-south flight. Also, we assume that the sensor and IMU body frame coordinate systems are

vertical. Therefore, we also assume that the sensor and IMU body frame coordinate systems are almost parallel. Lastly, we assume that we are flying over a flat horizontal terrain, where the scale is equal to the flying height over the principal distance, $\lambda = \frac{H}{c}$.

Now that these assumptions are established, we compute the partial derivatives with respect to each system parameter. Examining equation (3.11), we can see that there are three terms that are comprised of system parameters and needed to compute the partial derivatives for, namely $\dot{r}_{b(t_0)}^m \Delta t$, $R_{b(t)}^m r_c^b$ and $\lambda(i, c, t) R_{b(t)}^m R_c^b r_i^{c(t)}$. The first term, $\dot{r}_{b(t_0)}^m \Delta t$, only includes the time delay system parameter and its partial derivative will simply be the instantaneous linear velocity. Based on the sensor flight direction assumption and the incremental rotation resulting from the time delay, shown in equation (3.8), we can expand $R_{b(t)}^m$ to the form in equation (3.14). Using the assumption that the sensor to IMU-body frame lever arm is small, second order incremental terms in $R_{b(t)}^m r_c^b$ are ignored; and using equation (3.14), $R_{b(t)}^m r_c^b$ can then be expressed as in equation (3.15). Next, after multiplication of the image coordinate vector, boresight matrix, IMU body frame rotation matrix, and scale factor, the third term, $\lambda(i, c, t) R_{b(t)}^m R_c^b r_i^{c(t)}$, is expressed in equation (3.16) where second order incremental terms are again ignored. From equations (3.15) and (3.16), we explicitly have the terms needed for the partial derivatives.

$$\begin{aligned}
 R_{b(t)}^m &= \begin{bmatrix} \pm 1 & 0 & 0 \\ 0 & \pm 1 & 0 \\ 0 & 0 & 1 \end{bmatrix} \begin{bmatrix} 1 & -\dot{\kappa}_b(t_0)\Delta t & \dot{\phi}_b(t_0)\Delta t \\ \dot{\kappa}_b(t_0)\Delta t & 1 & -\dot{\omega}_b(t_0)\Delta t \\ -\dot{\phi}_b(t_0)\Delta t & \dot{\omega}_b(t_0)\Delta t & 1 \end{bmatrix} \\
 &= \begin{bmatrix} \pm 1 & \mp \dot{\kappa}_b(t_0)\Delta t & \pm \dot{\phi}_b(t_0)\Delta t \\ \pm \dot{\kappa}_b(t_0)\Delta t & \pm 1 & \mp \dot{\omega}_b(t_0)\Delta t \\ -\dot{\phi}_b(t_0)\Delta t & \dot{\omega}_b(t_0)\Delta t & 1 \end{bmatrix} \quad (3.14)
 \end{aligned}$$

$$R_{b(t)}^m r_c^b = \begin{bmatrix} \pm \Delta X \\ \pm \Delta Y \\ \Delta Z \end{bmatrix} \quad (3.15)$$

$$\begin{aligned}
 &\lambda(i, c, t) R_{b(t)}^m R_c^b r_i^{c(t)} \\
 = &\lambda(i, c, t) \begin{bmatrix} \pm x_i \mp y_i \Delta \kappa \mp \dot{\kappa}_b(t_0) y_i \Delta t \mp c \Delta \phi \mp \dot{\phi}_b(t_0) c \Delta t \\ \pm \dot{\kappa}_b(t_0) x_i \Delta t \pm x_i \Delta \kappa \pm y_i \pm c \Delta \omega \mp \dot{\omega}_b(t_0) c \Delta t \\ -\dot{\phi}_b(t_0) x_i \Delta t - x_i \Delta \phi + \dot{\omega}_b(t_0) y_i \Delta t + y_i \Delta \omega - c \end{bmatrix} \quad (3.16)
 \end{aligned}$$

The partial derivatives needed for the bias impact analysis are those relative to the lever arm components, boresight angles, and time delay. These partial derivatives, derived from equations (3.15) and (3.16), are expressed in equations (3.17a-3.17c) (see Appendix for expanded details). Examining these partial derivatives, one can see which dependencies these system parameters exhibit. The impact of the lever arm component changes depends on the flying direction. The impact of the boresight angles on the ground coordinates is a function of the flying height, flying direction, and the ratio of the image point coordinates and the principal distance, $\frac{x_i}{c}$ and $\frac{y_i}{c}$. Lastly, the impact of the time delay is a function of the linear and angular velocities, scale, image point coordinates, principal distance, and flying direction. The dependency of the bias impact for the system calibration parameters on image point location, flying direction, flying height, and linear and angular velocity are summarized in Table 3.1.

$$\delta r_I^m |_{\delta r_c^b} = \begin{bmatrix} \pm \delta \Delta X \\ \pm \delta \Delta Y \\ \delta \Delta Z \end{bmatrix} \quad (3.17a)$$

$$\delta r_I^m |_{\delta \Delta \omega, \delta \Delta \varphi, \delta \Delta \kappa} = H \begin{bmatrix} \pm \frac{x_i y_i}{c^2} \delta \Delta \omega \mp (1 + \frac{x_i^2}{c^2}) \delta \Delta \varphi \mp \frac{y_i}{c} \delta \Delta \kappa \\ \pm (1 + \frac{y_i^2}{c^2}) \delta \Delta \omega \mp \frac{x_i y_i}{c^2} \delta \Delta \varphi \pm \frac{x_i}{c} \delta \Delta \kappa \\ 0 \end{bmatrix} \quad (3.17b)$$

$$\delta r_I^m |_{\delta \Delta t} = \dot{r}_{b(t_0)}^m \delta \Delta t + \lambda(i, c, t) \begin{bmatrix} \pm \kappa_b(t_0) y_i \delta \Delta t \mp \dot{\varphi}_b(t_0) c \delta \Delta t \\ \pm \kappa_b(t_0) x_i \delta \Delta t \mp \dot{\omega}_b(t_0) c \delta \Delta t \\ -\dot{\varphi}_b(t_0) x_i \delta \Delta t + \dot{\omega}_b(t_0) y_i \delta \Delta t \end{bmatrix} \quad (3.17c)$$

Table 3.1 Dependency of the bias impact for the system calibration parameters on flight configuration & image point location

System Parameter	Image Point Location	Flying Direction	Flying Height	Linear Velocity	Angular Velocity
Lever Arm	NO	YES (except ΔZ)	NO	NO	NO
Boresight	YES	YES	YES	NO	NO
Time Delay	YES (only in the presence of angular velocities)	YES	YES (only in the presence of angular velocities)	YES	YES

Now that we know which system parameters produce a change in ground coordinates, and whether that change depends on the image point location, flying direction, flying height, and/or linear/angular velocity, we then design the optimal flight configuration for system calibration while considering time delay. As a result of this analysis we can conclude that the horizontal components of the lever arm can be estimated using different flying directions, while its vertical component is independent of flight configuration. On the other hand, to estimate boresight angles while decoupling them from lever arm components, different flying directions and flying heights are needed, as well as a good distribution of image points. Finally, to derive the time delay and decouple this parameter from the lever arm components and boresight angles, variation in linear/angular velocity and a good distribution of image points are required. In summary, it is recommended to derive the system parameters using opposite flying directions at different flying heights, as well as having a variation in the linear and angular velocities and good distribution of the image points. It should be emphasized that the assumptions imposed while deriving the minimal optimal flight configurations were only made to simplify the derivations and are not requirements for the presented approaches or experiments. If these assumptions are not met, the analysis of bias impact is not affected. Furthermore, any deviations from the abovementioned assumptions will lead to a more favorable impact on the ability to decouple system parameters. It should be noted that variation in the angular velocity might be difficult to control. However, for small, multi-rotor UAVs, angular velocity variation might be present. Using the optimal flight configuration, systematic errors can be easily detected, estimated, and removed, therefore resulting in more accurate 3D reconstruction.

3.3.4 Indirect Approach for Time Delay Estimation

The next approach we propose to evaluate time delay is the indirect approach. This approach uses the above bias impact analysis by exploiting the fact that the lever arm component in the flying direction is correlated with the time delay, given a single linear velocity and insignificant angular velocity. In other words, if flights in opposite directions and constant linear velocity are used, then the lever arm component in the flying direction will be correlated with the time delay. As a result, by estimating the lever arm component in the flying direction, while not considering the time delay, and then comparing it with the nominal value which can be directly measured from the GNSS/INS unit to the imaging sensor, one can discern the existence of a possible time delay in system synchronization. An illustration of where measurements are taken to acquire the nominal lever arm values is shown in Figure 3.6. This approach is meant as a special case in which one chooses to use an existing bundle adjustment with system self-calibration mechanism to estimate time delay, instead of incorporating the time delay as a parameter and implementing the direct approach.

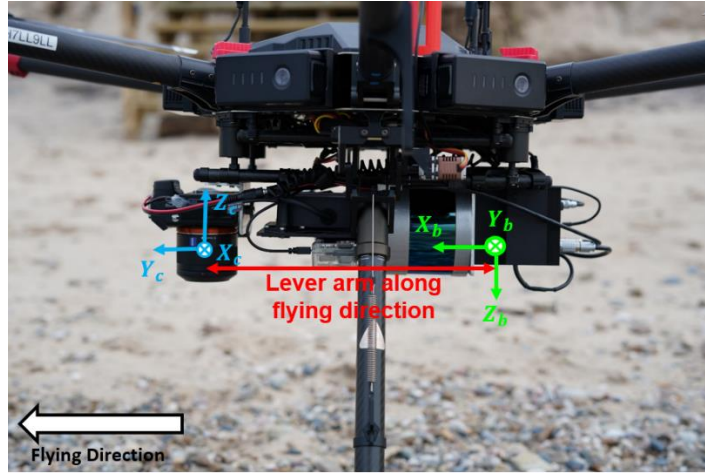


Figure 3.6. Illustration of where measurements are taken to acquire the nominal lever arm values.

The indirect approach consists of a single bundle adjustment, with the system self-calibration operation completed twice. In the first operation, an initial GNSS/INS-assisted bundle adjustment is performed to solve for the lever arm components (only lever arm in the flying direction) and boresight angles. If a significant time delay exists, the computed lever arm in the flying direction

will be quite different from the nominal value. This will be the first hint that the system may have a time delay issue. After the initial bundle adjustment is performed, the difference between the computed lever arm and the nominal/measured lever arm in the flying direction is derived. In the second operation, this difference in distance is now known and the time delay can be computed using the speed/time/distance relation. The computed time delay is then applied to derive the new position and orientation of IMU body frame at the actual exposure time. Finally, another bundle adjustment is performed to solve for the mounting parameters. Figure 3.7 presents the processing workflow of this approach.

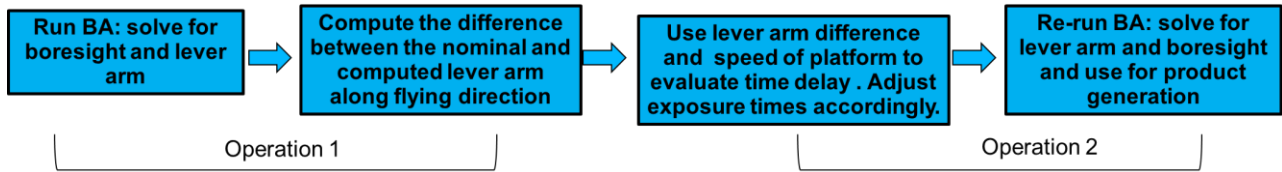


Figure 3.7 Processing workflow of the indirect approach process for time delay estimation.

In summary, the bundle block adjustment and mathematical model does not change from the traditional GNSS/INS-assisted bundle adjustment with system self-calibration procedure, expressed in Equation (3.3). The image coordinates are still a function of the trajectory information, IOPs, lever arm components, boresight angles, and ground coordinates. The time delay is not directly derived, but indirectly estimated using the lever arm deviation in the along flight direction and the speed/time/distance relation. However, one limitation of this approach is that because we are making the assumption that the time delay impact is absorbed by the lever arm in the flying direction, we have to fly at a single linear velocity. Additionally, because this approach only considers the impact of time delay on the lever arm component, it ignores the possibility of rotation changes during the time delay (i.e., angular velocity). Therefore, the calibration results may be less accurate than using the direct approach and an optimal flight configuration. However, the key advantage for the indirect approach is that it is capable of using existing bundle adjustment software to estimate the time delay in the system.

3.4 Experimental Results

In this section, data acquisition is discussed first, which includes information about the platforms and imaging systems used in this study. Next, the dataset description is presented. This description includes information on the flight configuration and ground control points collected. Finally, the experimental results and analysis are discussed. Each experiment and its results are presented in detail, along with an analysis discussion.

3.4.1 Date Acquisition

Data for validating the comparative performance of the proposed approaches in this study were acquired using two UAV systems, a Dà-Jiāng Innovations (DJI) Matrice 200 (M200) and a DJI Matrice 600 Pro (M600P) [39, 40]. Co-aligned thermal and RGB data were acquired with the DJI M200, and the DJI M600 was used as a second, RGB-only platform. Both systems included an on-board Applanix APX-15 UAV v2 GNSS/INS unit for direct geo-referencing, with a predicted positional accuracy of 2–5 cm and heading and roll/pitch of 0.080 and 0.025°, respectively [41]. Both imaging systems also had the means to send event marker signals to the GNSS/INS unit.

The DJI M200-based imaging system employed a FLIR Duo Pro R 640 combined thermal and RGB image sensor. The Uncooled VOx Microbolometer thermal sensor array was 640×512 with a pixel size of $17 \mu\text{m}$ and had a nominal focal length of 19mm. The RGB visible sensor array size was 4000×3000 , with a pixel size of $1.85 \mu\text{m}$ and a nominal focal length of 8 mm [42]. The Duo Pro R has an internal GNSS/INS unit for in-camera geo-tagging, but that unit was not used for this study. Figure 3.8 shows the FLIR Duo Pro R and APX-15 configuration on the M200 UAV, and illustrates the coordinate systems for the IMU body, camera, and vehicle frames. The FLIR Duo Pro R utilized a mobile-phone based app to set camera parameters via Bluetooth. The mobile-phone based app includes the ability to set the capture interval for the camera and to start and stop triggering. Event feedback to the APX was provided directly by the FLIR Duo Pro R using the “Frame Sync” option. This option output a low voltage transistor to transistor logic (3.3V) pulse that was wired directly to the event input of the APX-15. It is important to note that only one triggering interval and frame sync output can be set on the FLIR Duo Pro R, despite the fact that there are two sensors housed in the single unit. Therefore, one might assume that both

sensors are capturing images simultaneously. However, during the experiments, the FLIR thermal and RGB sensors were treated independently as separate sensors. The system calibration parameters, including the time delay, were estimated for each sensor so the results were not affected by having only one triggering interval.

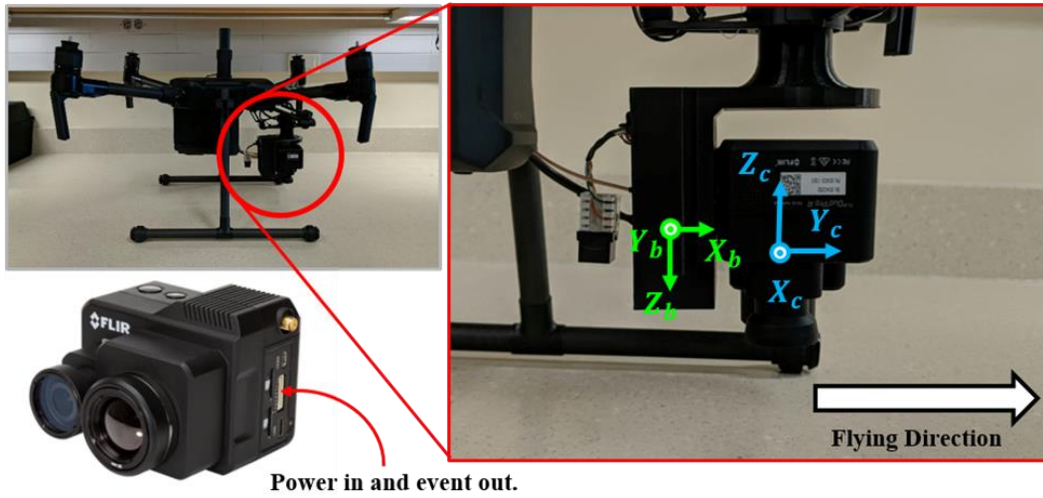


Figure 3.8 M200-based thermal/RGB system configuration.

The second imaging system, flown onboard the DJI M600P, incorporated a Sony Alpha 7R RGB camera and a Velodyne VLP-32C LiDAR sensor, although the LiDAR sensor was not used for this study. The Sony Alpha 7R (ILCE-7R) camera on the DJI M600P had a 7360×4912 CMOS array with a $4.9 \mu\text{m}$ pixel size, and a lens with a nominal focal length of 35 mm [43]. The M600-based RGB-only system used a direct feedback synchronization approach, utilizing the camera flash hot-shoe to generate a signal at the time the image was captured. This camera feedback signal was then sent to the APX-15 and a corresponding event time was recorded. This method also adjusted the event markers during post-processing to account for the constant time delay between the flash operation and the true mid-exposure time [11]. Figure 3.9 shows the Sony Alpha 7R and APX-15 configuration on the M600. Table 3.3 outlines the nominal boresight and lever arm values, as well as the angular field of view (FOV) for both the FLIR and Sony systems.

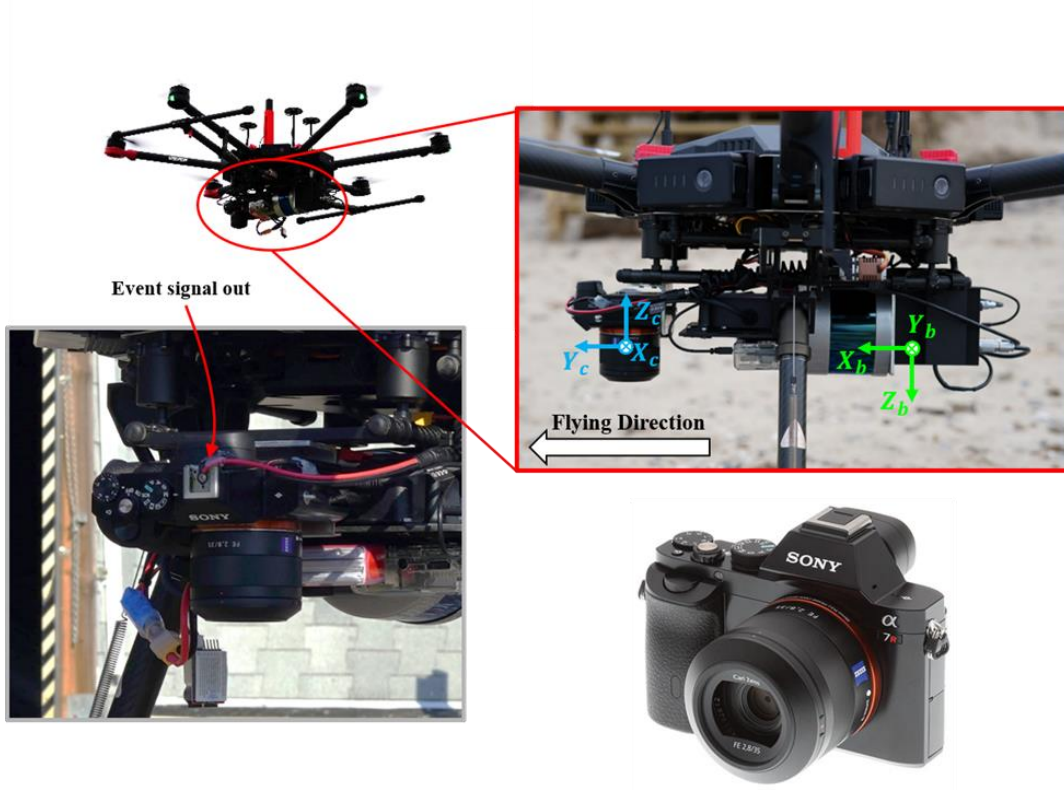


Figure 3.9 DJI M600-based Sony Alpha 7R system configuration.

Table 3.2 FLIR and Sony nominal boresight angles, lever arm components, and angular field of view.

Sensor	$\Delta\omega$ (Degree)	$\Delta\phi$ (Degree)	$\Delta\kappa$ (Degree)	Δx (m)	Δy (m)	Δz (m)	Angular FOV (Degrees)
FLIR—Thermal	180	0	-90	0.045	-0.015	0.045	32×26
FLIR—RGB				0.045	0.025	0.050	57×42
Sony—RGB	180	0	-90	0.260	0.026	-0.010	54×38

3.4.2 Dataset Description

Five datasets were collected for this time-delay estimation study. Four datasets were collected across two dates, July 25th and September 14th, with the FLIR Duo Pro R. For both collection dates, the FLIR Duo Pro R captured both thermal and RGB images. One RGB dataset from the Sony Alpha 7R camera was also captured and was evaluated alongside the FLIR datasets. Table 3.4 outlines the flight and data collection parameters for the FLIR Duo Pro R and the Sony Alpha 7R.

All datasets were collected at a research farm. Figure 3.10 outlines the flight trajectory for both the FLIR and Sony datasets. Figure 3.11 a, b shows the linear and angular velocity variations over the flight time for the July 25th thermal dataset, respectively. Analyzing Figure 3.11, the change in the linear velocity in the X direction can be explained by the variation in both the flying direction and linear velocity at different flying altitudes. Furthermore, significant changes in the linear and angular velocity were observed in the remaining linear and angular velocity components. This significant change was caused by the small size of the UAV, the impact of the wind, and the attempt of the autopilot to maintain a constant heading. The linear and angular velocities for this data demonstrate that the direct approach uses such variability for reliable estimation of the parameters. The indirect approach, on the other hand, has the capability to tolerate variations which would create decoupling between time delay and lever arm in the along flying direction. All other collection dates had similar linear and angular velocity variations over the flight time.

Table 3.3 FLIR and Sony flight parameters for the different data acquisition dates.

Date	Sensor	Altitude Above Ground	Ground Speed	GSD Thermal	GSD RGB	Overlap Thermal/R GB	Side lap Thermal/R GB	Number of Flight Lines	Number of Images
July 25 2018	FLIR Duo Pro R	20 m	2.7 m/s	1.8 cm	0.7 cm	70/80%	70/80%	6	284
		40 m	5.4 m/s	3.6 cm	1.4 cm	70/80%	70/80%	6	164
Sept. 14 2018		20 m	2.7 m/s	1.8 cm	0.7 cm	70/80%	70/80%	6	294
		40 m	5.4m/s	3.6 cm	1.4 cm	70/80%	70/80%	6	168
May 05 2019	Sony A7R	20 m	2.7 m/s	-	0.28 cm	70%	82%	6	198
		40 m	5.4 m/s	-	0.56 cm	70%	82%	6	116

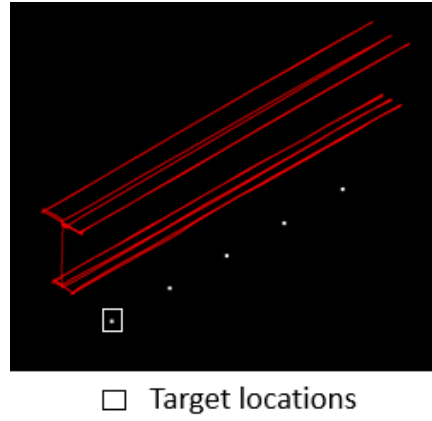


Figure 3.10 Trajectory and target locations for FLIR Duo Pro R and Sony Alpha 7R.

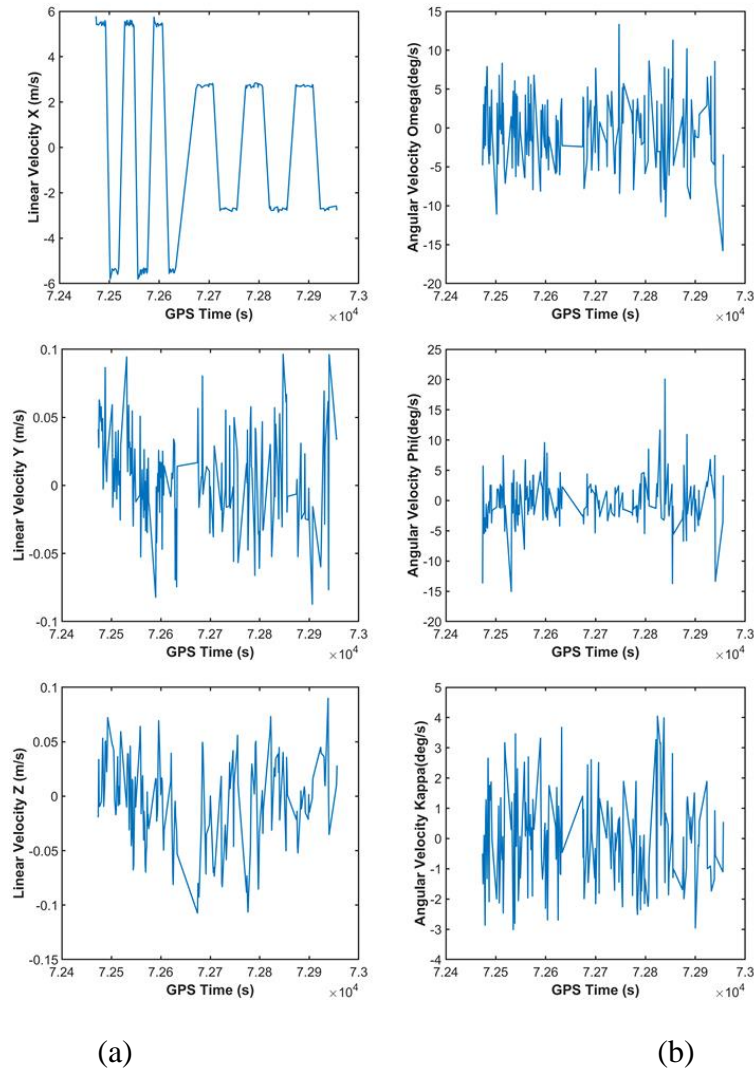


Figure 3.11 (a) XYZ component linear velocity over flight time for the July 25th thermal dataset. (b) ω , ϕ , κ component angular velocity over flight time for the July 25th thermal dataset.

Five checkerboard targets, used as checkpoints, were deployed in the calibration field for the FLIR and Sony cameras. The ground coordinates of all the checkerboard targets were surveyed by a Topcon GR-5 GNSS receiver with an accuracy of 2–3cm. The checkerboard targets were identified in raw and orthorectified images to either solve for the unknowns in the GNSS/INS-assisted bundle adjustment with system self-calibration process or check orthorectification accuracy, depending on the method implemented, respectively. Figure 3.12 shows full-size thermal and RGB imagery captured by the FLIR Duo Pro R camera. Here, it is clear that the angular field of view of the RGB is much larger than that of the thermal. Figure 3.13 shows the data collection area with enhanced representations of checkerboard targets and a zoomed region of the targets in the thermal and RGB images of the FLIR camera. Figure 3.14 shows sample RGB imagery captured by the Sony Alpha 7R. Figure 3.15 shows the flight area of the Sony Alpha 7R calibration field with the five checkerboard targets.

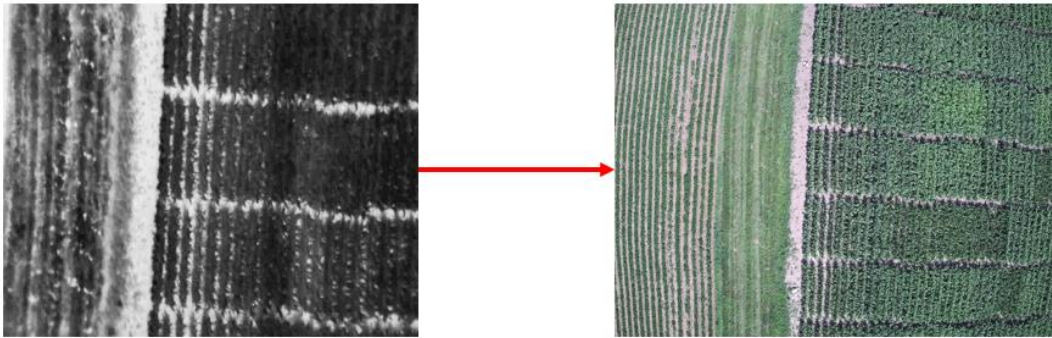


Figure 3.12 Sample corresponding thermal and RGB images from the FLIR Duo Pro R.

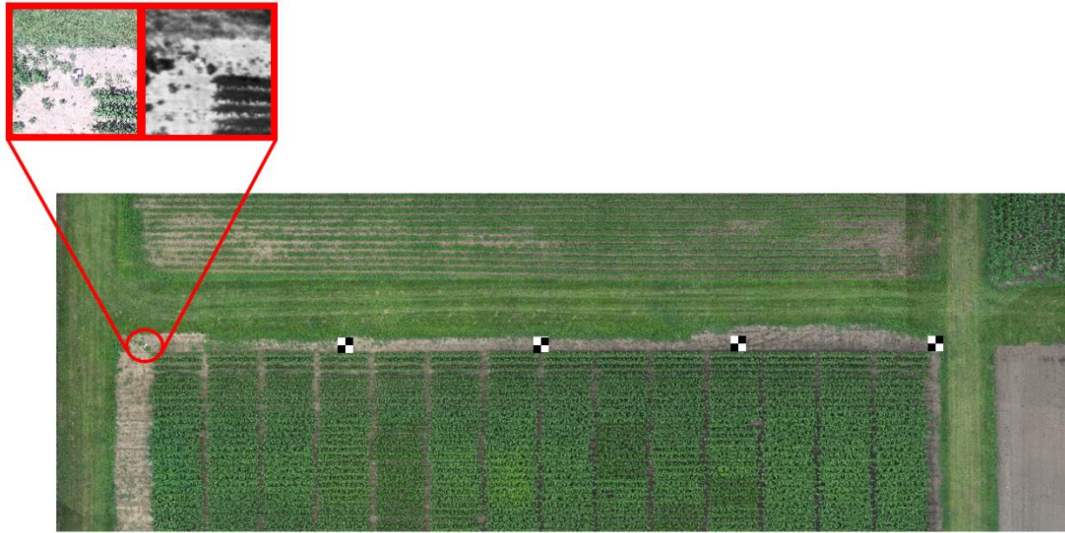
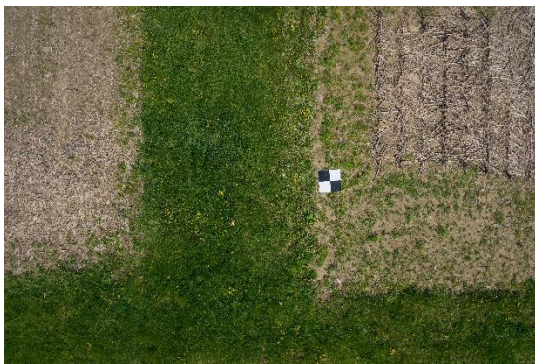
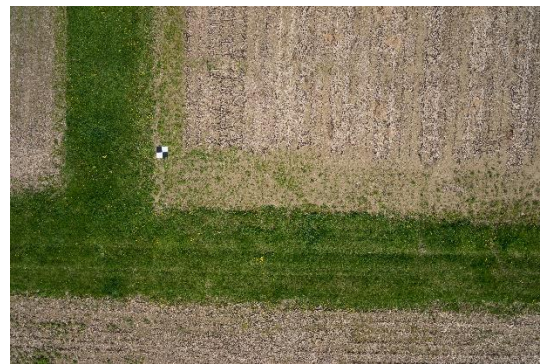


Figure 3.13 Flight area with enhanced representations of checkerboard targets and sample thermal and RGB images of the FLIR camera around the target location.



(a)



(b)

Figure 3.14 Sample images captured by the Sony RGB sensor over the calibration test field. (a) 20m flying height and (b) 40m flying height.



Figure 3.15 Sony A7R calibration field.

3.4.3 Experimental Results and Analysis

In this section, the proposed direct and indirect approaches were applied to each dataset, and the experiments tested the validity of the two approaches to successfully estimate time delay in an imaging system. In addition to the direct and indirect approach results, bundle adjustments that ignored the time delay are also presented for further comparison. As described in Section 3.2, the direct approach modifies the mathematical model to include the time delay as a system calibration parameter. This approach was simultaneously applied to both the 20 and 40 m flying height datasets for the DJI M200 and M600 platforms. The indirect approach makes use of existing bundle adjustment software and was applied only to a single flying height: 40 m for the FLIR and Sony cameras. In addition to the direct and indirect approach, bundle adjustment experiments were also conducted while ignoring the time delay, which was also only applied to the 40 m flying height for the FLIR and Sony cameras. The goal of these experiments was to test three main hypotheses. First, that the approaches can be applied to a variety of imaging platforms and maintain the ability to accurately estimate the time delay. Second, that the direct and indirect approaches are comparable. Finally, that the direct and indirect approaches produce consistently accurate results using the original GNSS/INS trajectory file.

Throughout this study, we referred to three different types of point classifications: control, tie, and checkpoints. Control points have known ground points, tie points are interest points used to tie overlapping imagery, and checkpoints are used for numerically evaluating results. Tie points in the indirect approach and in the bundle adjustments that ignored the time delay were established among stereo images (among the same sensor) using detected features from the Scale Invariant Feature Transform (SIFT) algorithm [44] within a Structure from Motion (SfM) strategy. The SfM algorithm starts with estimating initial relative orientation parameters (ROPs) between overlapping neighboring images while using the position and orientation information provided by the on-board GNSS/INS unit and considering the nominal mounting parameters relating the camera to the GNSS/INS unit. In the next step, SIFT detectors and descriptors are applied to the stereo pairs in question, and potential matches are then identified through a similarity evaluation of the Euclidian distances between SIFT descriptors for the detected features in both images. SIFT-based matches and initial ROPs are used to identify matching outliers based on point-to-epipolar distance of each corresponding point pair. Once all tie points are established among all possible stereo pairs, their ground coordinates are estimated using a simple intersection, and are used later as initial values in

the bundle adjustment procedure. These SIFT generated tie points were not used in the direct approach because it can sometimes be difficult to identify automatically-derived tie points in thermal imagery when dealing with data from multiple flying heights. To ensure we could apply the direct approach whether or not automatically-derived tie point detection was used, we used manually-measured points that corresponded to signalized targets. Because the direct approach does not use any other tie points except the checkpoints, the direct approach's results were considered to come from what will be referred to as a mini bundle adjustment. The indirect approach results, as well as the results ignoring the time delay, were considered as a full bundle adjustment.

For all direct approach experiments, the unknown system parameters included lever arm components in the along and across flying directions, boresight angles, time delay, and ground coordinates of checkpoints. It should be noted that the vertical lever arm component was not estimated in any experiments because it would require control points during the adjustments, and these experiments tested the approaches without the use of ground control. In the indirect approach experiments, lever arm components in the along and across flying directions, boresight angles, and ground coordinates of tie points, including checkpoints, were estimated. Once the initial bundle adjustment was performed in the indirect approach, the difference between the nominal and estimated lever arm along the flying direction was computed. Existing time delay was estimated by dividing this difference by the linear velocity, and was then considered to determine the actual time of exposure for each image. Next, IMU body frame position $r_{b(t)}^m$ and orientation $R_{b(t)}^m$ was estimated using linear and spherical linear interpolation of available GNSS/INS trajectory data (with 200HZ data rate), respectively. Lastly, a second bundle adjustment was performed with the updated (based the estimated time delay) IMU body frame position and orientation to derive the proper lever arm components in the along and across flying directions and boresight angles, as the unknown parameters. The experiments, while ignoring the time delay, used the same IOPs as other experiments, the same checkpoints, and the same SIFT-based tie points. The unknowns consisted of the ground coordinates of the five checkpoints, the ground coordinates of the SIFT-based tie points, and the boresight angles. It should be noted that the lever arm components were intentionally not solved for in the bundle adjustment that ignored time delay, because the time delay error would be absorbed by the lever arm in the along flying direction. For all cameras, IOPs were obtained prior to the experiments. An initial integrated sensor orientation (ISO) bundle

adjustment was performed on the FLIR thermal and RGB cameras to obtain the principal distance, principal point coordinates, and distortion parameters. The ISO bundle adjustment used SIFT-based tie points, five GCPs, and GNSS/INS assistance to obtain the IOPs. The IOPs for the Sony RGB camera were estimated through a combination of ISO and an indoor calibration lab procedure. The estimated IOPs were then used throughout all experiments and are presented in Table 3.5.

Table 3.4 Interior orientation parameters (IOPs) for the FLIR and Sony cameras.

Estimate d c (Pixel)	Estimate d x_p (Pixel)	Estimate d y_p (Pixel)	Estimated k1 (Pixel-2)	Estimated k2 (Pixel-4)	Estimated p1 (Pixel-1)	Estimated p2 (Pixel-2)
<i>Thermal- FLIR</i>						
1131.96	-5.238	3.2	$3.015e^{-007}$	$9.998e^{-014}$	$-1.992e^{-006}$	$2.302e^{-006}$
<i>RGB- FLIR</i>						
4122.26	35.07	-39.96	$-2.429e^{-008}$	$-1.250e^{-015}$	$1.576e^{-007}$	$-2.693e^{-007}$
<i>RGB- Sony</i>						
7436.44	-10.51	11.72	$7.771e^{-010}$	$-6.557e^{-017}$	$1.906e^{-007}$	$2.702e^{-007}$

Qualitative and quantitative analyses are presented for all experiments. The five signalized points were used as checkpoints to numerically evaluate results. The bundle adjustment derived 3D ground coordinates were numerically compared to ground truth data for quantitative analysis. Qualitative analyses were constructed by generating orthophotos with the original trajectory data and visually inspecting for good alignment for both the direct and indirect approaches. Additionally, orthophotos were generated from bundle adjustments while ignoring time delay, both with the original and refined trajectory data, and results were analyzed. The orthophotos were also quantitatively evaluated by measuring checkpoints and numerically comparing them to surveyed ground truth data.

3.4.3.1 DJI M200 integrated with FLIR Duo Pro R – FLIR Thermal

A summary of the FLIR thermal sensor results for the direct and indirect approaches while ignoring the time delay is presented in Table 3.6. In Table 3.6, the boresight angles and the square root of the a-posteriori variance factors are reported for all experiments. The estimated time delay and lever arm components in the across and along flying directions are presented for the direct and indirect approaches. Table 3.6 shows the estimated boresight $\Delta\omega$ and $\Delta\phi$ to be around 180° and -90° , respectively. In the bias impact analysis, we made the assumption that the boresight angles were small. This assumption was only made to simplify the bias impact derivation, and is not a requirement for conducting the estimation process. The time delay was estimated to be -268 and -261 ms for the direct approach on the two collection dates. For the indirect approach, the time delay is estimated to be -279 and -275 ms for the two collection dates. This consistency across the dates allowed estimation of the time delay in an initial system calibration, then use of that estimate for subsequent missions and applications. The square root of the a-posterior variance factor was less than 1 pixel for all experiments except the direct approach. The direct approach had a higher a-posterior variance factor, at 2–4 pixels, because far less tie points were used in the direct approach, leading to less redundancy. The correlation matrix of estimated system parameters for the July 25th direct approach results are reported in Table 3.6. The correlation values were similar in all experiments, therefore only one matrix is displayed in this study. All correlations were low except between the boresight angle $\Delta\phi$ and lever arm component ΔX , as well as between the $\Delta\omega$ and ΔY which had correlation values of 0.885 and -0.945 , respectively, which are highlighted in red in Table 3.7. Even though this correlation was high, it would be even higher without using the optimal flight configurations. Tests show that when only one flying height was used for the direct approach, the correlation between the boresight angle $\Delta\phi$ and lever arm component ΔX , as well as between the $\Delta\omega$ and ΔY , increased to 0.99. Therefore, using the optimal flight configuration presented in this study decoupled the parameters so that they could be estimated accurately.

Table 3.5 Estimated parameter results for the DJI M200 thermal platform, including the standard deviation for direct results.

	Estimated Time Delay Δt (ms)	Estimated Lever Arm ΔX (m)	Estimated Lever Arm ΔY (m)	Estimated Boresight $\Delta \omega$ (°)	Estimated Boresight $\Delta \varphi$ (°)	Estimated Boresight $\Delta \kappa$ (°)	Square Root of A-Posteriori Variance Factor (Pixel) $\hat{\sigma}_o$
<i>Ignoring Time Delay (bundle adjustment)</i>							
July 25 th	NA	NA	NA	179.12	1.26	−90.63	0.67
Sept 14 th	NA	NA	NA	179.05	1.23	−90.54	0.84
<i>Direct Approach (mini bundle adjustment)</i>							
July 25 th	−268 ± 2.6	0.114 ± 0.024	−0.032 ± 0.024	179.03 ± 0.055	−0.395 ± 0.052	−90.82 ± 0.093	4.63
Sept 14 th	−261 ± 1.41	0.100 ± 0.015	−0.038 ± 0.014	178.99 ± 0.030	−0.508 ± 0.028	−90.50 ± 0.060	2.19
<i>Indirect Approach (bundle adjustment)</i>							
July 25 th : Operation 1	N/A	−1.46	−0.015 (constant)	179.11	−0.56	−90.62	0.48
July 25 th : Operation 2	−279*	0.066	−0.29	178.68	−0.56	−90.72	0.47
Sept 14 th : Operation 1	N/A	−1.44	−0.015 (constant)	179.05	−0.58	−90.55	0.75
Sept 14 th : Operation 2	−275*	0.142	−0.27	178.68	−0.50	−90.91	0.72

* Time delay was estimated using the difference between the estimated lever arm in flying direction in Operation 1, and its nominal value while considering speed/time/distance relation.

Table 3.6 Correlation matrix of system parameters for July 25th thermal direct approach results.

	ΔX	ΔY	ΔZ (Not Estimated)	$\Delta \omega$	$\Delta \varphi$	$\Delta \kappa$	Δt
ΔX	1						
ΔY	-0.001	1					
ΔZ (not estimated)	0	0	1				
$\Delta \omega$	0.015	-0.945	0	1			
$\Delta \varphi$	0.885	-0.013	0	0.009	1		
$\Delta \kappa$	0.011	-0.026	0	0.024	-0.011	1	
Δt	-0.023	-0.067	0	0.022	0.326	-0.025	1

Five checkpoints' 3D coordinates were estimated in all of the experiments. Table 3.8 presents the XYZ components, mean, standard deviation, and RMSE of the differences between checkpoints and surveyed coordinates of the five checkpoints from estimated object point coordinates. As displayed in Table 3.4, the GSD of the FLIR thermal sensor was in the range of 1.8 to 3.6 cm for the different flying heights. For the direct approach results, the RMSE in the horizontal direction was approximately that of the GSD at 1–3 cm, and the indirect approach results showed no more than two times that of the GSD. Overall, the direct approach produced the best results for the XY components when compared to both the results of the indirect approach, and while ignoring the time delay. The vertical accuracy was much worse than the horizontal one. This was expected and can be explained by the geometric configuration. Using the base height ratio along with the variance in x-parallax, the estimated vertical accuracy was expected to be between 0.09–0.18 m. Therefore, estimated 0.07 and 0.08 m standard deviations in the vertical direction are within reason. Additionally, because of the small test area and the limited number of checkpoints, the Z-component showed a bias, reflected in the mean. For the RMSE Z-component, the indirect approach showed an approximate 26 to 63% decrease from the direct approach. This can be explained by the difference in tie points used. Since the indirect approach used the SIFT-based tie points, there were many more, with better distribution, compared to the few tie points used in the direct approach. That being said, the improvement in the X- and Y-components of the

direct approach over the indirect approach and the approach ignoring the time delay shows the superiority of the direct approach. More specifically, even though the direct approach did not use the SIFT-based tie points, which improved point distribution and geometry significantly, the direct approach was still capable of improving the results. The distribution of tie points for the direct and indirect approaches for the Sept 14th FLIR thermal dataset is shown in Figure 3.16. The distribution of tie points was similar for the other collection dates and sensors in these experiments. Furthermore, the mean standard deviations of the checkpoints are only presented for the direct results, because the bundle adjustments using the large number of SIFT-based tie points did not produce a final dispersion matrix, due to the large size of the unknowns. The mean standard deviation of the five checkpoints derived from the direct approach mini bundle adjustment is displayed in Table 3.9. Again, the horizontal components had better accuracy than the vertical.

Table 3.7 Components and mean/standard deviation/RMSE of the differences between checkpoints and surveyed coordinates for the five checkpoints for the DJI M200 thermal platform.

<i>Without Considering Time Delay</i> Thermal—July				<i>Without Considering Time Delay</i> Thermal—Sept		
	$X_{dif} (m)$	$Y_{dif}(m)$	$Z_{dif} (m)$	$X_{dif} (m)$	$Y_{dif}(m)$	$Z_{dif} (m)$
N1	0.03	0.03	−0.18	0.01	−0.05	−0.06
N2	0.05	0.06	−0.29	−0.06	−0.06	−0.12
N3	0.03	0.08	−0.51	−0.03	−0.01	−0.03
N4	−0.04	0.12	−0.12	−0.02	−0.01	0.02
N5	0.04	0.19	0.08	0.070	0.02	0.00
Mean	0.02	0.10	−0.20	−0.01	−0.02	−0.04
Standard Deviation	0.04	0.06	0.22	0.05	0.03	0.05
RMSE	0.04	0.11	0.28	0.05	0.04	0.06

Table 3.7 continued

<i>Direct Approach</i> Thermal—July				<i>Direct Approach</i> Thermal—Sept		
	$X_{dif} (m)$	$Y_{dif}(m)$	$Z_{dif} (m)$	$X_{dif} (m)$	$Y_{dif}(m)$	$Z_{dif} (m)$
N1	−0.02	0.05	0.14	−0.01	−0.02	0.24
N2	0.01	0.03	0.25	0.01	0.00	0.31
N3	0.01	0.03	0.12	0.00	−0.00	0.27
N4	−0.00	0.03	0.28	0.00	0.01	0.15
N5	−0.04	0.02	0.12	−0.003	0.01	0.16
Mean	−0.01	0.03	0.18	0.00	0.00	0.22
Standard Deviation	0.02	0.01	0.08	0.01	0.01	0.07
RMSE	0.02	0.03	0.19	0.01	0.01	0.23
<i>Indirect Approach</i> Thermal—July				<i>Indirect Approach</i> Thermal—Sept		
	$X_{dif} (m)$	$Y_{dif}(m)$	$Z_{dif} (m)$	$X_{dif} (m)$	$Y_{dif}(m)$	$Z_{dif} (m)$
N1	0.01	0.05	−0.11	−0.061	−0.02	0.14
N2	−0.01	0.05	−0.06	−0.078	−0.03	0.12
N3	0.01	0.05	−0.03	−0.03	0.01	0.21
N4	0.00	0.05	0.04	−0.0	−0.00	0.16
N5	0.04	0.07	0.10	0.07	0.01	0.20
Mean	0.01	0.05	−0.01	−0.02	−0.01	0.17
Standard Deviation	0.02	0.01	0.08	0.06	0.02	0.04
RMSE	0.02	0.06	0.07	0.06	0.02	0.17

Table 3.8 Mean standard deviation of five checkpoints from direct approach for the DJI M200 thermal platform from mini bundle adjustment.

<i>Direct Approach</i>			
	X(m)	Y(m)	Z(m)
July 25 th	0.018	0.018	0.096
Sept 14 th	0.011	0.011	0.072

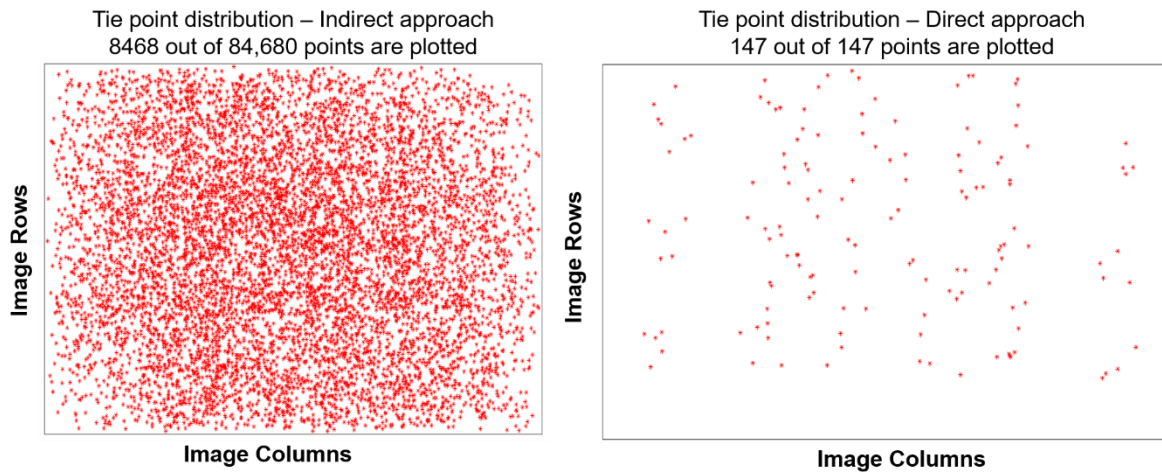


Figure 3.16 Distribution of the tie points used for the FLIR thermal sensor in the Sept. 14th collection date for the direct (**right**) and indirect* (**left**) approaches (*only 10% of total tie points are plotted).

The above M200 platform—thermal calibration results were used to create 1 cm orthophotos using the estimated system parameters from the results while ignoring the time delay, both using the original and refined trajectory data, as well as the direct and indirect approach results and for all collection dates, using only the original trajectory data. The orthorectification process was carried out by an in-house developed code. An orthophoto resolution of 1 cm was chosen as suitable for the agricultural application requirements. The 40 m flying height images were used for the orthophoto generation. Coordinates of the check targets were then measured on the generated orthophotos. Generating these orthophotos allowed for both a qualitative and quantitative evaluation of the system parameters used for each dataset. Figure 3.17 shows the orthophoto generated using the system parameters estimated while ignoring the time delay and

using the original trajectory data. Figure 3.18 shows the orthophoto generated using the system parameters estimated while ignoring the time delay, but with the refined trajectory data obtained using the bundle adjustment results. Visually, the orthophoto generated using the refined trajectory data, Figure 3.18, is much better than that of the one using the original trajectory data, Figure 3.17. This is because the refined trajectory was obtained from the bundle adjustment results where the exterior orientation parameters (EOPs) absorbed the impact of the time delay i.e., the pitch of the trajectory was modified to absorb the impact of the time delay. Figures 3.19 and 3.20 show the orthophotos generated using the direct approach's calibration results for the July 25th and September 14th collection dates, respectively. The indirect approach's orthophotos are visually similar to those of the corresponding direct approach results. Table 3.10 shows the statistics of horizontal/planimetric coordinate differences for the five check targets derived from the orthophotos. The results while ignoring time delay but refining the trajectory data prior to generating the orthophoto show comparable results to those of the direct and indirect approaches, which used the original trajectory data, with well-aligned orthophotos and a horizontal accuracy approximately 1–5 times the GSD of the original image. However, refining the trajectory data involves running the bundle adjustment then adjusting the original trajectory data based on the bundle adjustment results for each dataset. The results while ignoring the time delay and using the original trajectory data for generating the orthophoto show accuracy as low as 6–7 times that of the GSD of the original images. The qualitative and quantitative results from the generated orthophotos show that the direct and indirect approach produced accurate results while using the original trajectory data.

Table 3.9 Derived statistics of horizontal/planimetric coordinate differences for the five checkpoints derived from the orthophoto from the DJI M200 thermal platform.

<i>Ignoring Time Delay—Original Trajectory Data</i>			
	Mean—X/Y (m)	Standard Deviation—X/Y (m)	RMSE—X/Y (m)
July 25 th	−0.12/−0.07	0.24/0.11	0.25/0.12
Sept 14 th	−0.05/−0.12	0.21/0.24	0.23/0.27
<i>Ignoring Time Delay—Refined Trajectory Data</i>			
July 25 th	−0.02/−0.10	0.03/0.08	0.03/0.13
Sept 14 th	0.02/0.02	0.04/0.03	0.05/0.03
<i>Direct Approach—Original Trajectory Data</i>			
	Mean—X/Y (m)	Standard Deviation—X/Y (m)	RMSE—X/Y (m)
July 25 th	−0.04/−0.07	0.09/0.03	0.10/0.07
Sept 14 th	−0.09/0.03	0.14/0.03	0.15/0.03
<i>Indirect Approach—Original Trajectory Data</i>			
	Mean—X/Y (m)	Standard Deviation—X/Y (m)	RMSE—X/Y (m)
July 25 th	−0.04/−0.07	0.08/0.03	0.08/0.08
Sept 14 th	−0.06/−0.06	0.14/0.08	0.14/0.09

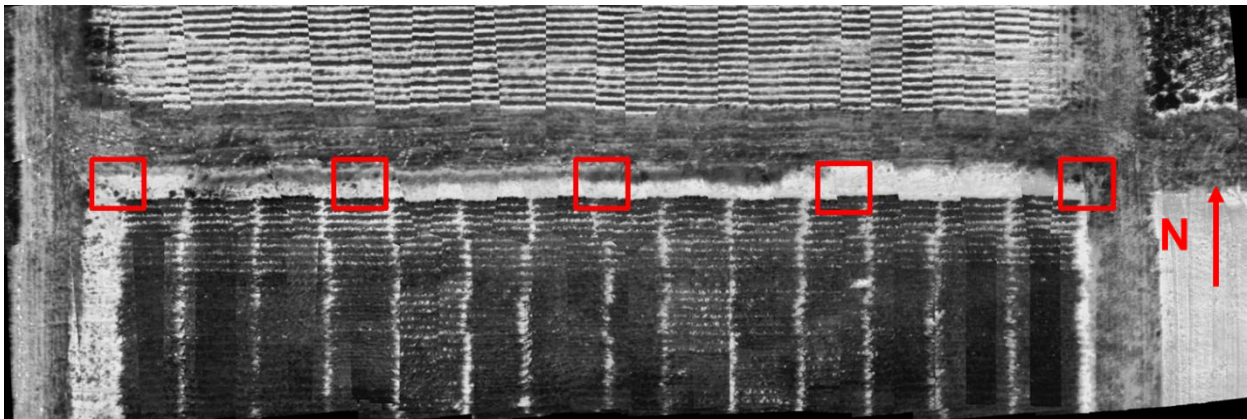


Figure 3.17 Orthophoto result while ignoring the time delay using the original trajectory data for FLIR thermal July 25th data collection (red boxes show the location of the checkpoints, *Original Image GSD* \approx 0.03m).

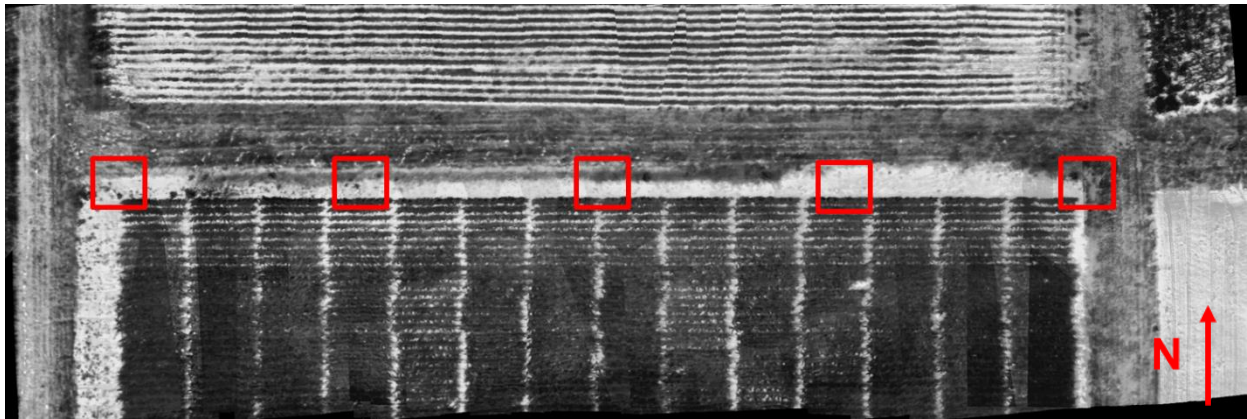


Figure 3.18 Orthophoto result while ignoring the time delay using the refined trajectory data for FLIR thermal July 25th data collection (red boxes show the location of the checkpoints, *Original Image GSD $\approx 0.03m$*).

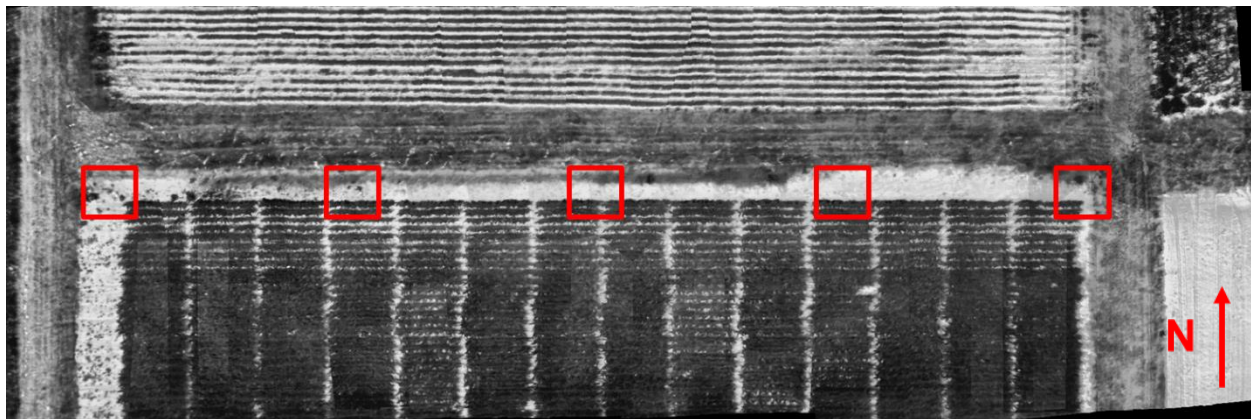


Figure 3.19 Orthophoto result from direct approach for FLIR thermal July 25th data collection (red boxes show the location of the checkpoints, *Original Image GSD $\approx 0.03m$*).

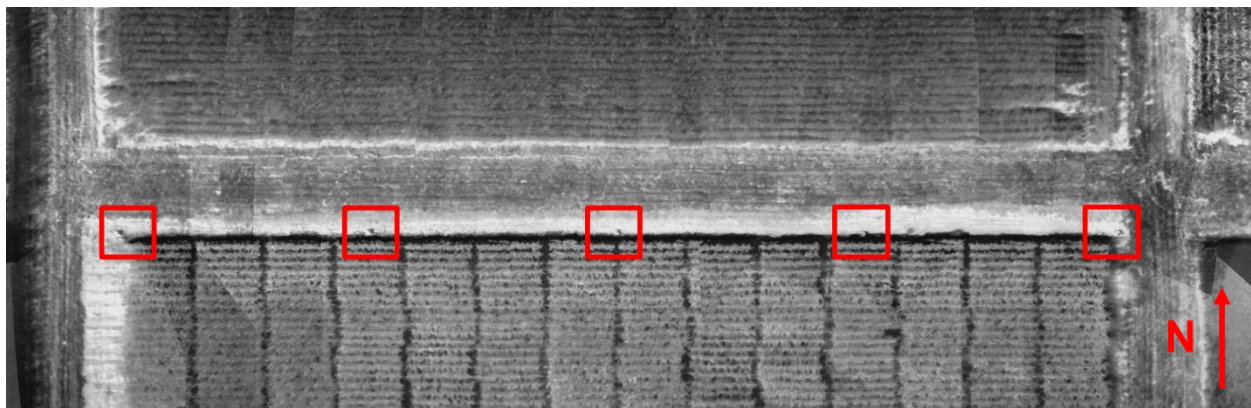


Figure 3.20 Orthophoto result from direct approach for FLIR thermal September 14th data collection (red boxes show the location of the checkpoints, *Original Image GSD $\approx 0.03m$*).

3.4.3.2 DJI M200 integrated with FLIR Duo Pro R – FLIR RGB

A summary of the FLIR RGB sensor results for both collection dates, while ignoring the time delay, and for the direct and indirect approaches is presented in Table 3.11. Table 3.11 shows the applicable estimated parameters as well as the square root of the a-posterior variance factor for all experiments. Similar to the thermal results, time delay estimated through the two approaches was comparable. Moreover, the two collection dates showed relatively consistent time delay, with time delays estimated to be in the range of –205 and –188 ms for both approaches. Based on the flying speed, the difference in the estimated time delay between –205 and –188 ms equates to approximately 4–9 cm on the ground. Given the APX predicted positional accuracy of 2–5 cm, and heading and roll/pitch of 0.080 and 0.025°, respectively, a difference in results of 4–9 cm on the ground would still be considered consistent results. Having a consistent time delay over multiple collection dates shows the potential to estimate the time delay in a calibration mission and then use that estimate for subsequent missions. However, the time delay estimates from the thermal sensor on the FLIR compared to the RGB sensor showed approximately 60–90 ms difference. This difference shows that the RGB and thermal sensor triggering were not simultaneous, and therefore would need independent calibration adjustments to estimate each sensor’s time delay. The square root of the a-posteriori variance factor was approximately 2.5 pixels for all experiments except the direct approach. The direct approach’s square root of the a-posteriori variance factor was approximately 4.7 pixels. Again, this difference in the a-posterior variance factor was because far fewer tie points were used in the direct approach. The components and the mean/standard deviation/RMSE of the differences between checkpoints and surveyed coordinates for the five checkpoints while ignoring the time delay, as well as for the direct and indirect approaches are presented in Table 3.12. Again, the horizontal component results for the direct approach were overall improved compared to both the indirect approach and while ignoring the time delay results. The RMSE in the horizontal direction for the direct approach was approximately 1–2 times the GSD of the 40 m flying height imagery. The RMSE in the horizontal direction for the indirect approach and ignoring the time delay was approximately 1–7 times the GSD of the 40 m flying height imagery. The vertical RMSE showed an improvement compared to the thermal sensor at approximately 8–11 cm. This improvement can be explained by the fact that the FLIR RGB has a larger angular FOV, presented in Table 3.3, which results in a better intersection geometry. Lastly, Table 3.13 shows the mean standard deviation of the five

checkpoints for the direct approach obtained in the mini bundle adjustment, with the reported values for the horizontal components being much less than that of the vertical. Again, the mean standard deviations of the checkpoints are only presented for the direct results because the bundle adjustments using the SIFT-based tie points do not produce a final dispersion matrix.

Table 3.10 Estimated parameter results for the DJI M200 RGB platform including the standard deviation for direct results.

	Estimated Time Delay Δt (ms)	Estimated Lever Arm ΔX (m)	Estimated Lever Arm ΔY (m)	Estimated Boresight $\Delta \omega$ (°)	Estimated Boresight $\Delta \varphi$ (°)	Estimated Boresight $\Delta \kappa$ (°)	Square Root of A-Posteriori Variance Factor (Pixel) $\hat{\sigma}_o$
<i>Ignoring Time Delay (bundle adjustment)</i>							
July 25 th	NA	NA	NA	178.55	0.26	−90.84	2.46
Sept 14 th	NA	NA	NA	178.61	0.50	−90.67	2.54
<i>Direct Approach (mini bundle adjustment)</i>							
July 25 th	−205 ± 0.433	0.068 ± 0.005	0.005 ± 0.005	178.57 ± 0.011	0.072 ± 0.011	−90.92 ± 0.014	4.78
Sept 14 th	−203 ± 0.457	0.073 ± 0.005	0.0083 ± 0.005	178.58 ± 0.012	0.119 ± 0.011	−90.83 ± 0.015	4.76
<i>Indirect Approach (bundle adjustment)</i>							
July 25 th : Operation 1	N/A	−0.97	0.025 (constant)	178.56	0.23	−90.87	2.46
July 25 th : Operation 2	−188	0.06	−0.02	178.55	0.23	−90.86	2.45
Sept 14 th : Operation 1	N/A	−1.03	0.025 (constant)	178.59	0.26	−90.68	2.53
Sept 14 th : Operation 2	−199	0.11	−0.03	178.53	0.22	−90.83	2.51

Table 3.11 Components and mean/standard deviation/RMSE of the differences between checkpoint and surveyed coordinates for the five checkpoints for the DJI M200 RGB platform.

<i>Without Considering Time Delay</i> RGB—July				<i>Without Considering Time Delay</i> RGB—September		
	$X_{dif} (m)$	$Y_{dif}(m)$	$Z_{dif} (m)$	$X_{dif} (m)$	$Y_{dif}(m)$	$Z_{dif} (m)$
N1	−0.07	−0.05	0.11	0.06	−0.03	0.07
N2	−0.03	0.01	0.10	0.01	−0.00	0.01
N3	0.01	0.08	0.08	−0.01	−0.03	−0.00
N4	0.04	0.13	0.06	−0.02	0.00	0.08
N5	0.09	0.20	0.01	0.07	0.06	0.14
Mean	0.01	0.07	0.07	0.02	0.00	0.06
Standard Deviation	0.06	0.10	0.04	0.04	0.04	0.06
RMSE	0.06	0.11	0.08	0.04	0.03	0.08
<i>Direct Approach</i> RGB—July				<i>Direct Approach</i> RGB—September		
	$X_{dif} (m)$	$Y_{dif}(m)$	$Z_{dif} (m)$	$X_{dif} (m)$	$Y_{dif}(m)$	$Z_{dif} (m)$
N1	0.00	0.04	0.07	−0.00	−0.02	0.10
N2	−0.01	0.03	0.10	−0.01	−0.01	0.11
N3	0.00	0.03	0.12	−0.00	−0.00	0.13
N4	−0.01	0.02	0.12	−0.02	−0.00	0.04
N5	−0.00	0.01	0.09	−0.02	0.00	0.05
Mean	0.00	0.02	0.10	−0.01	−0.01	0.09
Standard Deviation	0.01	0.01	0.02	0.01	0.01	0.04
RMSE	0.01	0.03	0.10	0.01	0.01	0.09

Table 3.11 continued

<i>Indirect Approach</i> RGB—July				<i>Indirect Approach</i> RGB—September		
	$X_{dif} (m)$	$Y_{dif}(m)$	$Z_{dif} (m)$	$X_{dif} (m)$	$Y_{dif}(m)$	$Z_{dif} (m)$
N1	0.06	0.00	−0.05	−0.05	−0.03	0.05
N2	0.04	0.04	−0.07	−0.05	−0.00	0.01
N3	0.03	0.09	−0.10	−0.03	−0.03	0.08
N4	0.00	0.13	−0.11	−0.04	−0.01	0.14
N5	−0.01	0.17	−0.15	−0.01	0.03	0.18
Mean	0.02	0.04	−0.04	−0.04	−0.01	0.09
Standard Deviation	0.04	0.05	0.03	0.02	0.02	0.07
RMSE	0.04	0.07	0.05	0.04	0.02	0.11

Table 3.12 Mean standard deviation of five checkpoints from direct approach for the DJI M200 RGB platform from mini bundle adjustment.

<i>Direct Approach</i>			
	X(m)	Y(m)	Z(m)
July 25 th	0.004	0.004	0.015
Sept 14 th	0.004	0.004	0.016

Again, once the calibration was completed the results were then used to generate 1 cm orthophotos while ignoring the time delay, both using the original and adjusted trajectory data, and for the direct and indirect, using the original trajectory data, and using the 40 m flying height data for all collection dates. Figure 3.21 and Figure 3.22 show the generated orthophotos for the results while ignoring the time delay. The direct results of the FLIR RGB sensor for both collection dates are shown in Figure 3.23 and Figure 3.24. The indirect orthophotos show similar visual results. The results while ignoring the time delay and using the refined trajectory data, as well as the results for the direct and indirect approaches, using the original trajectory data, show well-aligned orthophotos. Using the generated orthophotos, the five check targets were measured and the

statistics of the horizontal coordinate differences are shown in Table 3.14. These results showed horizontal accuracy ranging from 1–7 times the GSD of the original image. Table 3.14 shows the direct approach having slightly better results for the evaluation of orthophoto derived points compared to the control data than that of the indirect approach, and ignoring the time delay using the adjusted trajectory data. The results ignoring the time delay and using the original trajectory data were extremely poor and only two of the five checkpoints were visible for measurement.

Table 3.13 Derived statistics of horizontal/planimetric coordinate differences for the five check targets derived from the orthophoto for DJI M200 RGB platform.

<i>Ignoring Time Delay—Original Trajectory Data</i>			
	Mean—X/Y (m)	Standard Deviation—X/Y (m)	RMSE—X/Y (m)
July 25 th	–1.11/0.06	0.02/0.06	1.12/0.07
Sept 14 th	–0.38/–0.05	0.77/0.03	0.78/0.06
<i>Ignoring Time Delay—Refined Trajectory Data</i>			
July 25 th	–0.01/–0.10	0.07/0.09	0.08/0.13
Sept 14 th	–0.01/–0.01	0.05/0.04	0.05/0.04
<i>Direct Approach—Original Trajectory Data</i>			
	Mean—X/Y (m)	Standard Deviation—X/Y (m)	RMSE—X/Y (m)
July 25 th	–0.04/–0.07	0.06/0.02	0.06/0.07
Sept 14 th	0.01/0.01	0.01/0.03	0.01/0.03
<i>Indirect Approach—Original Trajectory Data</i>			
	Mean—X/Y (m)	Standard Deviation—X/Y (m)	RMSE—X/Y (m)
July 25 th	–0.03/0.07	0.04/0.03	0.05/0.08
Sept 14 th	–0.01/0.01	0.03/0.03	0.03/0.03



Figure 3.21 Orthophoto result ignoring the time delay using the original trajectory data for FLIR RGB July 25th data collection (red boxes show the location of the checkpoints—only two visible, *Original Image GSD* $\approx 0.01\text{m}$).



Figure 3.22 Orthophoto result ignoring the time delay using the refined trajectory data for FLIR RGB July 25th data collection (red boxes show the location of the checkpoints, *Original Image GSD* $\approx 0.01\text{m}$).



Figure 3.23 Orthophoto result from direct approach for FLIR RGB July 25th data collection (red boxes show the location of the checkpoints, *Original Image GSD* $\approx 0.01\text{m}$).

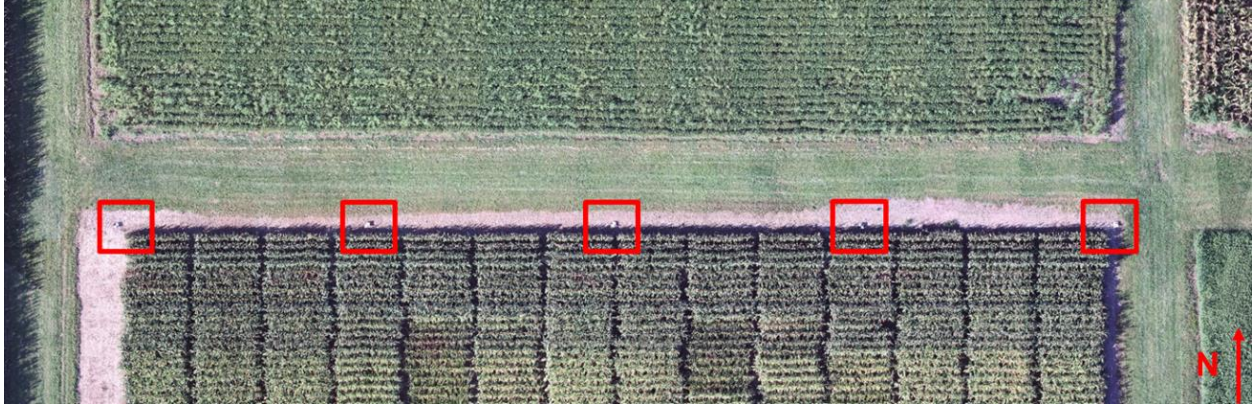


Figure 3.24 Orthophoto result from direct approach for FLIR RGB Sept. 14th data collection (red boxes show the location of the checkpoints, *Original Image GSD* $\approx 0.01\text{m}$).

3.4.3.3 DJI M600 integrated with Sony Alpha 7R (ILCE-7R)

The results while ignoring the time delay as well as the direct and indirect estimated parameter results for the DJI M600 platform are presented in Table 3.15. It should be noted that this Sony camera was modified prior to collection to incorporate the hardware direct feedback approach [32]. This hardware modification drastically reduced the time delay in the system. As we can see in Table 3.15, the estimated time delay for the Sony camera was in the range of -1.25 and -0.5 ms for the direct and indirect approaches, respectively. The components, mean, standard deviation, and RMSE of the differences between the checkpoints and surveyed coordinates of the five checkpoints from the bundle adjustment are illustrated in Table 3.16. All results were comparable. This was expected, since the time delay found for this platform was minimal. However, the $\Delta\omega$ estimated boresight angle for the direct approach was slightly different than that of the other results. This is because the direct approach did not refine the GNSS/INS data in the adjustment whereas the other bundle adjustments did. Additionally, the a-posterior variance factor was higher for the direct approach. This is because the direct approach only used the checkpoints as tie points in the mini bundle adjustment, compared to the bundle adjustments that used both checkpoints and SIFT-based tie points. The checkpoints had an approximate RMSE of 1–4 and 9 times the GSD for the 40 m flying height, in the horizontal and vertical direction, respectively. Table 3.17 shows the mean standard deviation of the checkpoints from the direct approach mini bundle adjustment. The mean standard deviation for the X , Y , and Z components were very low. The direct approach generated orthophoto from DJI M600 dataset is illustrated in Figure 3.25, while statistical

evaluations of checkpoint targets are presented in Table 3.18. All other orthophotos generated were visually similar to that of the direct approach, and therefore are not presented. The orthophoto derived coordinates of the check targets showed horizontal RMSE of approximately 2–5 times the GSD in both X and Y directions for the 40 m flying height.

Table 3.14 Estimated parameter results for the DJI M600 platform, including the standard deviations for the direct results.

	Estimated Time Delay Δt (ms)	Estimated Lever Arm ΔX (m)	Estimated Lever Arm ΔY (m)	Estimated Boresight $\Delta\omega$ ($^\circ$)	Estimated Boresight $\Delta\phi$ ($^\circ$)	Estimated Boresight $\Delta\kappa$ ($^\circ$)	Square Root of A- Posteriori Variance Factor (Pixel) $\hat{\sigma}_o$
<i>Ignoring Time Delay (bundle adjustment)</i>							
May 06 th	NA	NA	NA	178.29	−0.09	−91.12	1.56
<i>Direct Approach (mini bundle adjustment)</i>							
May 06 th	−1.25 ± 0.48	0.267 ± 0.004	0.019 ± 0.004	179.32 ± 0.011	−0.097 ± 0.010	−91.08 ± 0.013	5.61
<i>Indirect Approach (bundle adjustment)</i>							
May 06 th : Operation 1	N/A	0.268	0.026 (constant)	179.29	−0.09	−91.12	1.56
May 06 th : Operation 2	−0.5	0.27	0.002	179.29	−0.09	−91.12	1.56

Table 3.15 Components and mean/standard deviation/RMSE of the differences between checkpoint and surveyed coordinates for the five checkpoints for the DJI M600 platform—Sony RGB.

<i>Ignoring Time Delay</i>				<i>Direct Approach</i>			<i>Indirect Approach</i>		
	$X_{dif} (m)$	$Y_{dif}(m)$	$Z_{dif} (m)$	$X_{dif} (m)$	$Y_{dif}(m)$	$Z_{dif} (m)$	$X_{dif} (m)$	$Y_{dif}(m)$	$Z_{dif} (m)$
N1	−0.04	0.02	−0.00	−0.01	0.02	−0.03	−0.04	0.02	−0.00
N2	−0.03	0.00	−0.05	−0.01	0.01	−0.03	−0.03	0.01	−0.05
N3	−0.03	0.02	−0.06	−0.02	0.02	−0.02	−0.03	0.02	−0.06
N4	−0.01	0.02	−0.07	−0.01	0.01	−0.03	−0.01	0.02	−0.07
N5	0.02	0.01	−0.01	−0.01	−0.00	−0.00	0.02	0.01	−0.01
Mean	−0.02	0.02	−0.04	−0.01	0.01	−0.02	−0.02	0.02	−0.04
Standard Deviation	0.02	0.01	0.03	0.00	0.01	0.01	0.02	0.01	0.03
RMSE	0.03	0.02	0.05	0.01	0.01	0.03	0.03	0.02	0.05

Table 3.16 Mean standard deviation of five checkpoints from direct approach for the DJI M600 platform from bundle adjustment.

<i>Direct Approach</i>			
	X(m)	Y(m)	Z(m)
May 06th	0.003	0.003	0.013

Table 3.17 Derived statistics of horizontal/planimetric coordinates for five check targets derived from orthophoto—DJI M600 platform.

<i>Ignoring Time Delay—Original Trajectory Data</i>			
	Mean—X/Y (m)	Standard Deviation—X/Y (m)	RMSE—X/Y (m)
May 06 th	0.03/−0.02	0.02/0.02	0.04/0.03
<i>Ignoring Time Delay—Adjusted Trajectory Data</i>			
May 06 th	0.02/−0.02	0.02/0.01	0.03/0.02
<i>Direct Approach—Original Trajectory Data</i>			
	Mean—X/Y (m)	Standard Deviation—X/Y (m)	RMSE—X/Y (m)
May 06 th	0.03/−0.02	0.01/0.02	0.03/0.03
<i>Indirect Approach—Original Trajectory Data</i>			
	Mean—X/Y (m)	Standard Deviation—X/Y (m)	RMSE—X/Y (m)
May 06 th	0.03/−0.02	0.02/0.02	0.03/0.03

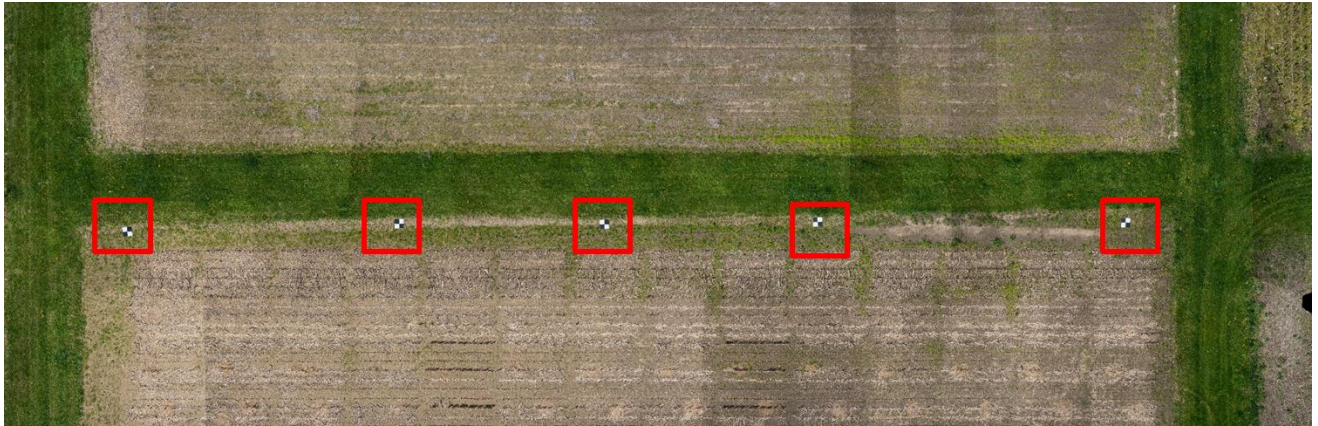


Figure 3.25 Orthophoto result from direct approach for Sony—May 06th data collection (red boxes show the location of the checkpoints, $GSD \approx 0.0056m$).

3.5 Conclusions and Recommendations for Future Work

UAV-based GNSS/INS-assisted imaging systems need proper system calibration for accurate 3-D spatial reconstruction. With consumer-grade systems, a time delay between the GNSS/INS event markers and the actual exposure time may exist. This time delay needs to be modeled and estimated for accurate geospatial products. In this study, two approaches – direct and indirect –

for estimating this time delay were introduced. Optimal flight configuration for system calibration while considering time delay was also derived through bias impact analysis. A modified mathematical model was derived for the direct approach so that the time delay can be directly estimated in a one-step bundle adjustment process. Whereas the indirect approach leveraged the traditional mathematical model and bundle adjustment procedure to estimate the time delay indirectly using the nominal lever arm, speed/time/distance relationship, and bias impact analysis findings. Experimental results were presented for two UAV systems with different imaging sensors and multiple collection dates.

In summary, both the direct and indirect approaches accurately estimate the time delay between the GNSS/INS event marker time and the actual image mid-exposure time. The results show that these approaches are capable of producing reliable estimates of the time delay across multiple platforms and with a variety of sensors. The results show that the direct approach is capable of producing accuracy at approximately the same level as the GSD of the system. This accuracy is achieved using direct geo-referencing, without the use of ground control data and while using the original trajectory data. In addition, the results showed consistency across the dates which allows one to estimate time delay in an initial system calibration then use that estimate for subsequent missions and applications. The results show that attempting a calibration while ignoring the time delay and using the original trajectory data, for a system with time delay, produces poor orthophoto results both visually and absolute accuracy evaluation. Ignoring the time delay but adjusting the trajectory did improve results over ignoring the time delay and using the original trajectory. However, adjusting the trajectory information is time consuming and require an additional bundle adjustment for each dataset. The direct and indirect approaches not only estimate the time delay but are capable of using the original trajectory data for generating orthophotos. The results also show that the direct and indirect approaches increase the horizontal accuracy compared with the bundle adjustment while ignoring the time delay. Overall, the direct approach is recommended over the indirect because it directly estimates the time delay by modifying the bundle adjustment mathematical model, is capable of incorporating the optimal configuration, and improves absolute accuracy. It also is capable of incorporating multiple flying heights and linear/angular velocity which allows users to implement the optimal configuration and therefore estimate and decouple system parameters with the highest accuracy. However, both

direct and indirect approaches covered in this study can be implemented in system calibration to account for a time delay and used without the need for ground control.

In previous works, there have been both software and hardware solutions for estimating and correcting for time delay in an imaging system. Previous software solutions included either a 1-step procedure that required modification to bundle adjustment code or a 2-step procedure that did not require code modification but required two different independent adjustments. All previous software solution studies discussed in this article require ground control points for estimation of the time delay. Furthermore, none of the previous studies presented in this article provide a rigorous derivation of optimal flight configurations. Below is a list of the contributions this study presents:

- Two approaches, direct and indirect, were shown to accurately estimate time delay to accommodate users with and without capability of modifying bundle adjustment software code.
- The indirect approach does not require modification to the bundle adjustment code and it also only needs a single bundle adjustment process.
- Rigorously derived optimal flight configurations were presented.
- The two approaches were shown to be reliable across a variety of platforms and sensors.
- The direct approach is capable of producing accuracy at approximately the same level as the GSD of the system.
- The accuracy achieved were without the use of ground control points.
- The direct and indirect approaches are capable of using the original trajectory data for generating accurate orthophotos.
- Both approaches were shown to handle sensors with relatively large time delay appropriately, therefore no prior hardware modification is necessary.

Future work will focus on incorporating the direct approach into a comprehensive bundle adjustment where one could also use SIFT tie points. Automated extraction of targets will also be

an avenue of future work. Also, an investigation of the internal GNSS/IMU of the FLIR-thermal/RGB sensor will be included to determine whether it also has a time delay. Lastly, using quaternions instead of rotation matrices within the bundle adjustment would allow for better interpolation of platform orientation while considering time delay and will also be investigated.

3.6 Acknowledgements

The information, data, or work presented herein was funded in part by the Advanced Research Project Agency-Energy (ARPA-E), U.S. Department of Energy, under Award Number DE-AR0000593. The work was partially supported by the Nationally Geospatial Intelligence Agency (NGA) The contents of this paper reflect the views of the authors, who are responsible for the facts and the accuracy of the data presented herein, and do not necessarily reflect the official views or policies of the sponsoring organizations.



© 2019 by the authors. Submitted for possible open access publication under the terms and conditions of the Creative Commons Attribution (CC BY) license (<http://creativecommons.org/licenses/by/4.0/>).

4. SYSTEM CALIBRATION INCLUDING TIME DELAY ESTIMATION FOR GNSS/INS-ASSISTED LINE CAMERAS ONBOARD UAV PLATFORMS

This research article is in the final stages of formatting and is planned for submission to the Photogrammetric Engineering & Remote Sensing (PE&RS) journal.

Abstract: Unmanned aerial vehicles (UAVs) equipped with imaging systems and integrated global navigation satellite system/inertial navigation system (GNSS/INS) are used for a variety of applications. Disaster relief, infrastructure monitoring, precision agriculture, and ecological forestry growth monitoring are among some of the applications that utilize UAV imaging systems. For most applications, accurate 3D spatial information from the UAV imaging system is required. Deriving reliable 3D coordinates is conditioned on accurate geometric calibration. Geometric calibration entails both spatial and temporal calibration. Spatial calibration consists of obtaining accurate internal characteristics of the imaging sensor as well as estimating the mounting parameters between the imaging and the GNSS/INS units. Temporal calibration ensures that there is little to no time delay between the image timestamps and corresponding GNSS/INS position and orientation timestamps. Spatial calibration has been successfully accomplished on a variety of platforms and sensors including UAVs equipped with frame and push-broom line cameras. However, temporal calibration has only been demonstrated with frame camera systems. This paper performs spatial and temporal system calibration for a UAV with a GNSS/INS-assisted hyperspectral push-broom line camera. Two approaches, direct and indirect, are applied to hyperspectral line cameras for system calibration while considering time delay. The direct results show that when a time delay exists and spatial and temporal calibration is performed, vertical and horizontal accuracy are approximately that of the ground sample distance (GSD) of the sensor. Also, even when there is a small time delay in the system but an unfavorable tie point distribution, the direct approach shows a huge improvement in vertical accuracy compared to ignoring the time delay. Furthermore, when a large artificial time delay is introduced, the direct approach still achieves accuracy less than the GSD of the system and performs 2.5-8 times better in the horizontal components and up to 18 times better in the vertical component than not performing the temporal calibration. This paper also shows that the indirect approach is not a feasible solution for push-

broom line cameras onboard UAVs due to the limited ability of line cameras to decouple system parameters. This finding provides further support that the direct approach is recommended for temporal calibration on UAV line camera systems. The results in this paper were obtained with UAV line camera imaging systems, however, these findings are general enough to extend to other line camera systems such as satellite push broom and airborne systems.

4.1 Introduction and Related Work

Remote sensing is a highly effective technique for gathering information without needing to make physical contact with the object being mapped and is used for a variety of applications. One major application is in agriculture. Specifically, remote sensing is used for biomass prediction and defining plant locations from UAV-based remote platforms [18, 20, 45]. The ability to predict biomass and define plant locations via a UAV-based imaging system can save substantial time and money. Because of its wide range of spectral bands, hyperspectral imagery is often used for soil content estimation and mineralogy [46-47]. Many times, multiple sensors are combined on one platform to improve the synergy between the collected data. Others have used LiDAR and hyperspectral sensors for modelling vascular plant species richness and mapping coastal environments [48-49]. For all remote sensing applications, geometric system calibration is vital for determining accurate positioning. Geometric calibration includes spatial and temporal calibration. Spatial calibration accurately estimates both internal characteristics and mounting parameters of the system. Previous work has been completed on spatial calibration for frame and hyperspectral line camera systems [9, 50]. In addition to the spatial calibration, one important aspect of geometric calibration for remote sensing systems is the temporal calibration, which is the focus of this study. Image exposure epochs have to be precisely time stamped with the corresponding GNSS time. Temporal calibration eliminates time delay between the timestamps of the image exposure epoch and the corresponding GNSS/INS position and orientation epoch. There have been a few groups that have focused on temporal calibration. Elbahnasawy and Habib [11] focused on two hardware solutions to perform temporal calibration. The authors introduced a simulated feedback approach where a signal is sent to both the GNSS/INS system and the imaging sensor simultaneously. However, this approach does not account for the camera response delay in which a time delay exists between the camera receiving the signal and the camera capturing the image. The authors second approach, the direct feedback, utilized the camera flash hotshoe to

generate a signal at the time the image is captured. This camera feedback signal is then sent to the on-board GNSS/INS and a corresponding event time is recorded thus accounting for the camera response delay between receiving the triggering signal and the actual imaging exposure. While some researchers focus on hardware solutions for temporal calibration, others emphasize software modifications. Gabrlik et al. [13] and Chiang et al. [12] both use a two-step approach for estimating and removing time delay in their systems. First, exterior orientation parameters (EOPs) are estimated using indirect geo-referencing with the help of ground control points (GCPs). Next, the difference in estimated EOPs and GNSS/INS trajectory at the time of exposure is computed where they then solve for the lever arm components, boresight angles, and time delay. Lastly, the calibration parameters can be used in direct geo-referencing. Both Gabrlik et al. [13] and Chiang et al. [12] depend on GCPs and a two-step approach to estimate time delay in their systems. Blazaquez, M. [15] presents a one-step approach for temporal calibration. This approach focuses on adjusting the sensor model to include time delay as a system parameter. Blazaquez, M. [15] uses the GNSS/INS-based linear and angular velocities to consider the impact of time delay on the position and orientation. This approach also depends on the availability of GCPs for accurate time delay estimation. Rehak and Skaloud [10] have also addressed temporal calibration. First, they used the direct feedback hardware approach to reduce time delay in their system to a minimum. Then, they tested two separate methods for temporal calibration. First, they conducted a two-step approach which analyzed the residuals between the observed camera position and orientation and those estimated through indirect geo-referencing. Their second method consisted of a one-step approach that modified the mathematical model to include the GNSS/INS position, rotation, and linear and angular velocity as observations. Optimal flight configurations were presented which included the use of GCPs. Furthermore, the study suggested that the lever arm components be estimated in a laboratory setting instead of during an in-situ system calibration. LaForest et al. [50] presented two separate one-step approaches. The first, the direct approach, modified the existing mathematical model to include time delay as a system parameter, which can then be estimated. An optimal flight configuration was rigorously derived to suggest the most ideal collection for simultaneously estimating system parameters. The second approach, the indirect, exploited the optimal flight configuration and corresponding system parameter correlations to estimate the time delay indirectly from the flying speed and estimated lever arm component in the flying direction.

Both approaches successfully estimated time delay and mounting system parameters without the use of control points.

In this paper, the direct and indirect approaches are used for geometric system calibration including time delay estimation. Compared to all other previous work that only focused on frame camera systems, this paper introduces and performs spatial and temporal calibration for line camera systems. First, the modified mathematical model for line camera systems is presented in the methodology section. Then the direct approach is introduced for line camera systems. The optimal flight configuration is derived for line camera systems and compared to that for frame camera systems. Using the optimal flight configuration conclusions, a discussion of the indirect approach's ability to estimate time delay for line camera systems is also presented. Next, a description of the imaging platforms and data collection is presented. The results and analysis are then presented for each system and experiment. The paper concludes with a summary and future work section.

4.2 Methodology

This section begins with a review and discussion of the collinearity equations and bundle block adjustment for both frame and line camera systems. Next, the direct approach and the modified mathematical model will be covered specifically for line camera systems. A detailed discussion of optimal configurations for both frame and line cameras will follow along with a comparison of the two. Finally, details of the indirect approach method for line camera systems conclude this section.

4.2.1 Collinearity Equations for Frame and Line Camera Systems

For remote sensing imaging platforms, photogrammetric models are used to derive 3D coordinates from the system's 2D imagery. The collinearity constraint equations are a well-known mathematical model that represents the relationship between the 2D image coordinates and the 3D ground coordinates. To express these equations, it should first be stated that the following notations are used throughout this paper: a vector connecting point 'b' to point 'a' relative to a coordinate system associated with point 'b' is represented as r_a^b and a rotation matrix transforming from coordinate system 'a' to coordinate system 'b' is represented as R_a^b . The collinearity equations

expressing the relationship between 3D ground coordinates and the 2D image coordinates are shown in Equation (4.1).

$$r_I^m = r_{b(t)}^m + R_{b(t)}^m r_c^b + \lambda(i, c, t) R_{b(t)}^m R_c^b r_i^{c(t)} \quad (4.1)$$

Where:

r_I^m : ground coordinates of the object point I

$r_i^{c(t)}$: vector connecting perspective center to the image point i captured by the camera at the actual time t

t : actual time of exposure

$r_{b(t)}^m$: position of IMU body frame relative to the mapping reference frame at time t derived from the GNSS/INS integration process

$R_{b(t)}^m$: rotation matrix from the IMU body frame to the mapping reference frame at the actual time t derived from GNSS/INS integration process

r_c^b : lever arm from IMU body frame to camera frame

R_c^b : rotation (boresight) matrix from camera to IMU body frame

$\lambda(i, c, t)$: scale factor for point i captured by camera c at the actual time t

Equation (4.1) is a generic form of the collinearity equations and can be used for frame and push-broom line camera imaging systems. An illustration of the collinearity equations is shown in Figure (4.1), with frame camera in Figure (4.1a) and line camera in Figure (4.1b). The main difference between frame camera and line camera is that the frame camera's scene is captured in one instance by a single image whereas the line camera's scene is built by multiple images captured sequentially. A scene is considered a 2D coverage area of the ground. Given this geometry, frame camera's image coordinates, $r_i^{c(t)}$, will consist of both x and y values that are variable depending on image point location which is bounded by the sensor's angular field of view (AFOV). However, line camera's x image coordinates will have variable values but y will always be constant depending on the camera alignment on the sensor's focal plane.

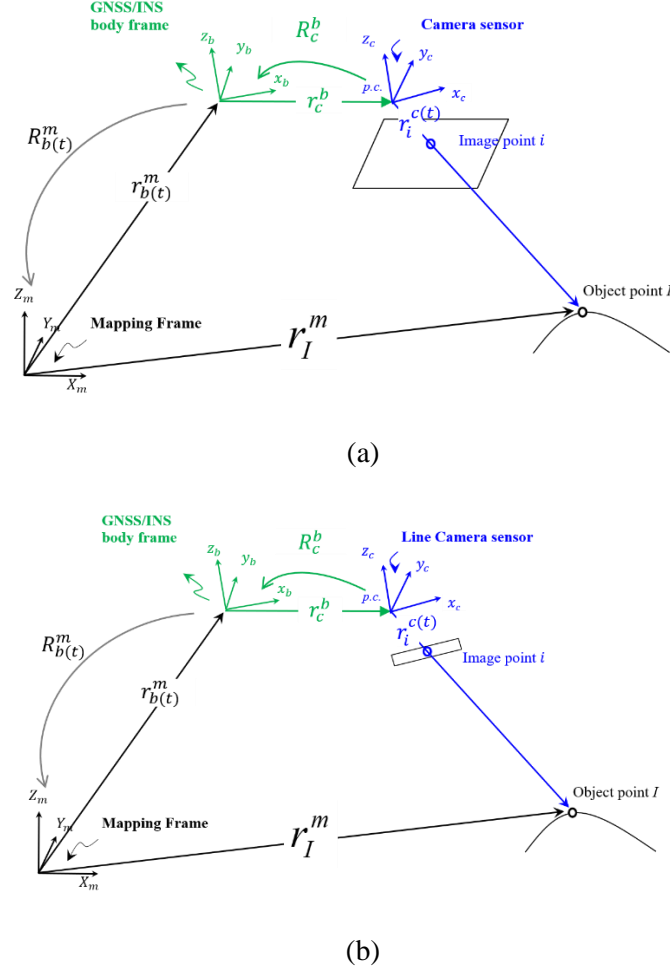


Figure 4.1 Illustration of collinearity equations for (a) frame camera and (b) push-broom line camera.

4.2.2 Direct Approach for Time Delay Estimation in Line Camera Systems

The direct approach was first presented by LaForest et al. [50] where the mathematical model was modified to incorporate time delay as a system parameter for frame camera systems. This section introduces the modified mathematical model for line camera systems. Examining Equation (4.1), there are three terms that are affected by time delay – position $r_{b(t)}^m$ of the platform, orientation $R_{b(t)}^m$ of the platform, and scale, $\lambda(i, c, t)$. However, the scale factor is routinely eliminated by dividing the first and second equations by the third, therefore leaving only the position and orientation as the components directly affected by the time delay. The goal is to modify the mathematical model in Equation (4.1) to account for the potential time delay affecting

the position and orientation components. First, definitions of the different times involved are provided. Throughout this manuscript, we will refer to the term “event marker”, which is used to indicate the time of exposure based on feedback signals received by the GNSS/INS unit from the camera. The initial GNSS/INS event marker time is denoted by t_0 . The time delay is denoted by Δt . Lastly, combining those terms, the actual sensor exposure time is $t = t_0 + \Delta t$. Using those time definitions, the position that accounts for time delay, $r_{b(t)}^m$, can be expressed by the position at the initial event marker, $r_{b(t_0)}^m$ and adding the displacement cause by the time delay, $\Delta t \dot{r}_{b(t_0)}^m$, where $\dot{r}_{b(t_0)}^m$ is the instantaneous linear velocity and comprised of three components $\dot{r}_{b(t_0)}^m(x)$, $\dot{r}_{b(t_0)}^m(y)$, and $\dot{r}_{b(t_0)}^m(z)$ in the x, y, and z directions, respectively. The instantaneous linear velocity is expressed in Equation (4.2), where dt is a user specified time interval based on the specifications of the GNSS and INS data rates. The final form of the position equation that accounts for time delay is expressed in Equation (4.3).

$$\dot{r}_{b(t_0)}^m = \frac{1}{dt} [r_{b(t_0+dt)}^m - r_{b(t_0)}^m] \quad (4.2)$$

$$r_{b(t)}^m = r_{b(t_0)}^m + \Delta t \dot{r}_{b(t_0)}^m \quad (4.3)$$

The second term affected by a time delay in the system is the orientation of the IMU body frame, $R_{b(t)}^m$. The changes in the attitude (i.e., angular velocity) of the IMU body frame at different times is needed for establishing an expression for the correct IMU body frame orientation in the presence of time delay. The user defined time orientation change within the dt time interval is denoted by $R_{b(t_0+dt)}^{b(t_0)}$ and is used to compute the angular velocity. The angular velocity is derived by using the rotation at the initial GNSS/INS event time and the incremental orientation change, and is shown in Equation (4.4) where $d\omega_{b(t_0)}$, $d\phi_{b(t_0)}$, and $d\kappa_{b(t_0)}$ are the changes in the attitude angles over the user-defined time interval. From there, the changes in the orientation are expressed with an incremental rotation matrix since the angular changes caused by time delay are relatively small, and are expressed in Equation (4.5) where $\dot{\omega}_{b(t_0)}$, $\dot{\phi}_{b(t_0)}$, and $\dot{\kappa}_{b(t_0)}$ are the instantaneous angular velocities at t_0 . Lastly, using the IMU body frame at the initial event marker along with the attitude changes caused by the time delay, the IMU body orientation at the actual exposure time is derived in Equation (4.6).

$$R_{b(t_0+dt)}^{b(t_0)} = R_m^{b(t_0)} R_{b(t_0+dt)}^m = \text{Rotation}(d\omega_{b(t_0)}, d\phi_{b(t_0)}, d\kappa_{b(t_0)}) \quad (4.4)$$

$$R_{b(t_0+\Delta t)}^{b(t_0)} = \text{Rotation}(\dot{\omega}_{b(t_0)}\Delta t, \dot{\phi}_{b(t_0)}\Delta t, \dot{\kappa}_{b(t_0)}\Delta t) \quad (4.5)$$

$$\cong \begin{bmatrix} 1 & -\dot{\kappa}_{b(t_0)}\Delta t & \dot{\phi}_{b(t_0)}\Delta t \\ \dot{\kappa}_{b(t_0)}\Delta t & 1 & -\dot{\omega}_{b(t_0)}\Delta t \\ -\dot{\phi}_{b(t_0)}\Delta t & \dot{\omega}_{b(t_0)}\Delta t & 1 \end{bmatrix}$$

$$R_{b(t)}^m = R_{b(t_0)}^m R_{b(t_0+\Delta t)}^{b(t_0)} \quad (4.6)$$

The collinearity equations expressed in Equation (4.1) can now be modified to include the time delay as a system parameter and are expressed in Equation (4.7). The image coordinate measurements are now a function of the trajectory information, IOPs, lever arm components, boresight angles, ground coordinates, and time delay and can all be estimated during a bundle block adjustment procedure. A bundle block adjustment procedure enforces intersection of the light rays connecting the perspective centers of the images encompassing corresponding image points of the tie feature and the respective conjugate image points. The target function is to ensure the best intersection of conjugate light rays from images along the same or different flight lines. In this study, the unknowns consist of the lever arm in the X and Y components, boresight angles, time delay, and XYZ ground coordinates of tie and checkpoints where checkpoints are used to assess the quality. The lever arm in the Z component will not cause discrepancies in the light ray intersections (i.e., will not affect the precision of the reconstruction process) and therefore cannot be estimated [51]. The linear and angular velocities as well as the position and orientation are considered as prior information available from the GNSS/INS system. The image coordinates are the observations which are manually-measured. For each observation or image point measurement, the collinearity equations will produce two equations. In general, for an object point that is visible in n -images, there will be $2n$ collinearity equations after eliminating the scale factors.

$$r_i^c = \frac{1}{\lambda(i, c, t)} R_b^c \left[R_{b(t_0)}^{b(t_0+\Delta t)} R_m^{b(t_0)} (r_l^m - r_{b(t_0)}^m - \dot{r}_{b(t_0)}^m \Delta t) - r_c^b \right] \quad (4.7)$$

4.2.3 Optimal Flight Configuration for Line Camera System Calibration while Considering Time Delay

In order to determine the calibration parameters, an optimal flight configuration that maximizes the impacts of deviations from the true values for the system parameters, denoted as systematic error or biases, must be derived. Determining the optimal flight configuration allows for the systematic errors to be more easily detected and removed, resulting in a more accurate estimation of system parameters. To obtain the best flight configuration, a bias impact analysis of system parameters is analyzed. A systematic shift in ground coordinates will be produced by changes in the system parameters. The bias impact is derived by examining the partial derivatives of the collinearity equations with respect to each system parameter. A few assumptions are made for deriving the partial derivations. These assumptions are to simplify the derivations and deviations from these assumptions would have a more favorable effect on the ability to decouple the impact of various system parameters. The assumptions are: i) the sensor and IMU body frame coordinate systems are almost parallel – i.e., small boresight angles; ii) the sensor and IMU body frame coordinate systems are vertical; iii) the sensor is travelling with a constant attitude in the south-to-north and north-to-south directions; iv) the terrain is flat horizontal; and v) the lever arm components are relatively small.

To begin deriving the partial derivatives, the modified collinearity equations expressed in Equation (4.7) are rewritten and shown in Equation (4.8) so that the ground coordinates are a function of system parameters and image measurements. From Equation (4.8), the three terms comprised of system parameters needed for partial derivatives for bias impact analysis are $\dot{r}_{b(t_0)}^m \Delta t$, $R_{b(t)}^m r_c^b$, and $\lambda(i, c, t) R_{b(t)}^m R_c^b r_i^c$. The partial derivatives are then derived following the assumptions made above and are expressed in Table 4.1 for both frame and line camera systems. The main difference between frame cameras and line cameras is that for line cameras the y image measurements, y_i , equal 0, where the camera is vertically below the perspective center. This affects several system parameter's impact on ground coordinates which in turn affects decoupling the terms.

$$r_I^m = r_{b(t_0)}^m + \dot{r}_{b(t_0)}^m \Delta t + R_{b(t_0)}^m R_{b(t_0+\Delta t)}^{b(t_0)} r_c^b + \lambda(i, c, t) R_{b(t_0)}^m R_{b(t_0+\Delta t)}^{b(t_0)} R_c^b r_i^c \quad (4.8)$$

Table 4.1 Impact of bias in system parameters on 3D point coordinates for frame and line camera systems

Bias in System Parameters	Impact on Ground Coordinates					
	δX		δY		δZ	
	Frame	Line Camera	Frame	Line Camera	Frame	Line Camera
$\delta \Delta X$	$\pm \delta \Delta X$		0		0	
$\delta \Delta Y$	0		$\pm \delta \Delta Y$		0	
$\delta \Delta Z$	0		0		$\delta \Delta Z$	
$\delta \Delta \omega$	$\pm \frac{x_i y_i}{c^2} H \delta \Delta \omega$	0	$\pm \left(1 + \frac{y_i^2}{c^2}\right) H \delta \Delta \omega$	$\pm H \delta \Delta \omega$	0	
$\delta \Delta \varphi$	$\mp H \left(1 + \frac{x_i^2}{c^2}\right) \delta \Delta \varphi$		$\mp \frac{x_i y_i}{c^2} H \delta \Delta \varphi$	0	0	
$\delta \Delta \kappa$	$\mp \frac{y_i}{c} H \delta \Delta \kappa$	0	$\pm \frac{x_i}{c} H \delta \Delta \kappa$		0	
$\delta \Delta t$	$\begin{aligned} & \dot{r}_{b(t_0)}^m(x) \delta \Delta t \\ & + \lambda(i, c, t) \left[\pm \frac{H}{c} \dot{\omega}_{b(t_0)} x_i y_i \mp c \left(1 + \frac{x_i^2}{c^2}\right) \dot{\varphi}_{b(t_0)} \mp y_i \dot{\kappa}_{b(t_0)} \right] \delta \Delta t \end{aligned}$	$\begin{aligned} & \dot{r}_{b(t_0)}^m(x) \delta \Delta t \\ & \mp \lambda(i, c, t) c \left(1 + \frac{x_i^2}{c^2}\right) \dot{\varphi}_{b(t_0)} \delta \Delta t \end{aligned}$	$\begin{aligned} & \dot{r}_{b(t_0)}^m(y) \delta \Delta t \\ & + \lambda(i, c, t) \left[\pm c \left(1 + \frac{y_i^2}{c^2}\right) \dot{\omega}_{b(t_0)} \mp \frac{1}{c} \dot{\varphi}_{b(t_0)} x_i y_i \pm x_i \dot{\kappa}_{b(t_0)} \right] \delta \Delta t \end{aligned}$	$\begin{aligned} & \dot{r}_{b(t_0)}^m(y) \delta \Delta t \\ & \pm \lambda(i, c, t) \left[c \dot{\omega}_{b(t_0)} \pm x_i \dot{\kappa}_{b(t_0)} \right] \delta \Delta t \end{aligned}$	$\dot{r}_{b(t_0)}^m(z) \delta \Delta t$	

The partial derivatives are now used to assess the impact of each system parameter. The focus will be on the system parameters that have the possibility of being highly correlated or more difficult to decouple. Analyzing rows 1 and 5 of Table 4.1, for frame cameras, the lever arm ΔX affects the X direction only and the boresight roll $\Delta\phi$, affects both the X and Y directions. Because of these effects on both the X and Y directions, the $\delta\Delta X$ and $\delta\Delta\phi$ can be decoupled. However, for line cameras, the lever arm ΔX and the boresight angle roll $\Delta\phi$ affects only the X direction. Therefore, this creates an increased probability of $\delta\Delta X$ and $\delta\Delta\phi$ being highly correlated or harder to decouple. This is especially true when there is a single flying height and when the angular field of view, defined by $\frac{x_i}{c}$, is small. Examining rows 2 and 4 of Table 4.1, a similar difference for frame cameras and line cameras can also be observed in the Y direction. For frame cameras, the lever arm ΔY affects the Y direction only. The boresight roll angle $\Delta\omega$, affects both the X and Y directions. Therefore, $\delta\Delta Y$ and $\delta\Delta\omega$ can easily be decoupled. However, for line cameras, the lever arm ΔY and boresight angle roll $\Delta\omega$ affects the only Y direction. Therefore, this creates high probability of $\delta\Delta Y$ and $\delta\Delta\omega$ being highly correlated or harder to decouple. This is especially true when there is a single flying height. There is also an expected correlation among $\delta\Delta\kappa$, $\delta\Delta Y$, and $\delta\Delta\omega$ specifically for line camera systems since all the impact on ground coordinates will only be seen in the δY direction. This will be true when there is a single flying height and when the angular field of view is small. Frame cameras will not have as much correlation among $\delta\Delta\kappa$, $\delta\Delta Y$, and $\delta\Delta\omega$ because $\delta\Delta\kappa$ and $\delta\Delta\omega$ effect both the X and Y directions and can rely on larger AFOV to help decoupling such parameters. Analyzing row 7 of Table 4.1, both for frame camera and line camera systems, it is important to have a variability of the linear and angular velocity components to ensure that the time delay can be decoupled effectively. For frame camera systems, having variability in the linear velocity or any of the angular velocity components, $\dot{\omega}_{b(t_0)}$, $\dot{\phi}_{b(t_0)}$, $\dot{\kappa}_{b(t_0)}$, will ensure that the time delay is decoupled from other system parameters. However, for line camera systems, since the y image coordinates, y_i , equal 0, $\delta\Delta t$'s impact on the X direction – i.e., $\delta X|_{\delta\Delta t}$ – is only affected by the $\dot{r}_{b(t_0)}^m(x)$ linear velocity component and the $\dot{\phi}_b$ angular velocity component. The $\delta\Delta t$'s impact on the Y direction – i.e., $\delta Y|_{\delta\Delta t}$ – is only affected by the $\dot{r}_{b(t_0)}^m(y)$ linear velocity component and the $\dot{\omega}_b$ and $\dot{\kappa}_b$ angular velocity components. Therefore, linear camera systems rely more on the variability of the angular velocity in each component than that of frame cameras. Moreover, if the line camera system has a small AFOV, $\frac{x_i}{c}$ variability is limited

which further restricts the possibility of decoupling system parameters. Using this bias impact analysis, it can be concluded that the optimal flying configuration for line camera systems are opposite flying directions at different flying heights as well as having a variation in linear and angular velocities with good point distribution of the image points across the scan line.

The bias impact analysis will now be analyzed for the use of the indirect approach for line camera systems. The indirect approach uses the bias impact analysis by exploiting the fact that the time delay is correlated with the lever arm, ΔY , along the flying direction given a single ground speed and minor changes in angular velocities, shown in Table 4.1. The time delay is not directly derived, but indirectly estimated using the lever arm deviation in the along flying direction and speed/time/distance relation. As presented for frame cameras, the indirect approach is meant for special cases in which an existing bundle adjustment cannot be modified to incorporate the modified mathematical model that accounts for time delay [50]. To exploit the correlation between the time delay and lever arm in the flying direction, a single flying speed, constant attitude, and a single flying height is needed. However, as discussed in the impact analysis for line camera systems, if there is a single flying height, the lever arm component ΔX will be highly correlated with the boresight angle $\Delta\phi$ and therefore produce inaccurate estimates of the system parameters. Also, with a single flying height, the lever arm component ΔY and boresight angle $\Delta\omega$ will also be highly correlated. Furthermore, the field of view for line camera systems is much less than that of frame camera systems and cannot assist as much to decouple the system parameters. More specifically, for line cameras the y image measurements, y_i , equal 0, this imposes more reliance on the AFOV to decouple parameters. For a small AFOV, $\frac{x_i}{c}$ is small, and therefore $\frac{x_i^2}{c^2}$ is even smaller which will then impose more challenges in decoupling system parameters. Therefore, using the impact bias analysis, it is concluded that the indirect approach should not be used for line camera systems. The experimental results show an example of the indirect approach for line camera systems to emphasize this conclusion.

4.3 Experimental Results

First, a description of the platforms and imaging systems used in this study is discussed. Next, the dataset description, including checkpoints, is provided. Lastly, the experimental results and analysis are discussed.

4.3.1 Data Acquisition

In this study, several remote sensing imaging platforms were used and equipped with a GNSS/INS system and imaging sensor. The DJI Matrice 600 Pro (M600P) was the UAV platform used [40]. This system included the Applanix APX-15 UAV v2 GNSS/INS unit for direct georeferencing with a predicted positional accuracy of 2-5 cm and heading and roll/pitch accuracy of 0.080 and 0.025°, respectively [41].

The DJI M600P platforms were equipped with three different line camera sensors. Two of the line cameras used were Headwall's Nano-hyperspectral sensors operating at the visible and near-infrared. In this study, the Nano-hyperspectral sensors will be referred to as 'nHS', along with their corresponding ending serial number – nHS-70 and nHS-199. These Nano-hyperspectral sensors cover 270-273 spectral bands ranging between 398 – 1000 nm with a band width of 2.2 nm. The scan line consist of 640 pixels and has a detector pitch of 7.5 µm [52]. The sensor has a focal length of 8.2 mm resulting in a field of view of approximately 31° (horizontal). The approximate GSD values of the sensors are 1.79 and 3.58 cm when flying at 20 and 40 m flying height, respectively. The third line camera aboard the DJI M600P was the shortwave infrared (SWIR) sensor, referred to as uVS-307 in this study. The uVS-307 covers 166 spectral bands ranging between 900 and 2500 nm with a band width of 9.6 nm. The uVS-307 consists of 384 pixels along the scan line and has a pixel pitch of 24 µm [53]. The focal length of the uVS-307 is 24.6 mm resulting in a field of view of 21° (horizontal). The approximate GSD values at a flying height of 20 and 40 m are 1.95 and 3.89 cm, respectively. It should be noted that the nHS-70 and the uVS-307 were installed simultaneously on the DJI M600P during the flight collections. For the nHS-199, the DJIM600P was also equipped with both a LiDAR and RGB imaging sensor on-board. However, for this study the nHS-199 Nano and the APX unit were the only systems used during collections. An image of the DJI M600P equipped with the nHS-70 and uVS-307, along with the sensor and vehicle coordinate system orientation is shown in Figure 4.2. An image of the DJI M600P equipped with the nHS-199 along with the sensor and vehicle coordinate system alignment is shown in Figure 4.3. Table 4.2 outlines the nominal boresight and lever arm values for the systems. All three push-broom line cameras flown on the DJI M600P were equipped with the APX. The system records a pulse per second (PPS), frame index count per line, and position and orientation along with the UTC (at 100 Hz), and Nano/SWIR clock count. The link between the pulse per second from the APX, frame index count, and UTC time is used to acquire the

timestamp for each scan line needed to find the corresponding position and orientation. However, a time delay can still exist between these signals and the recorded times.

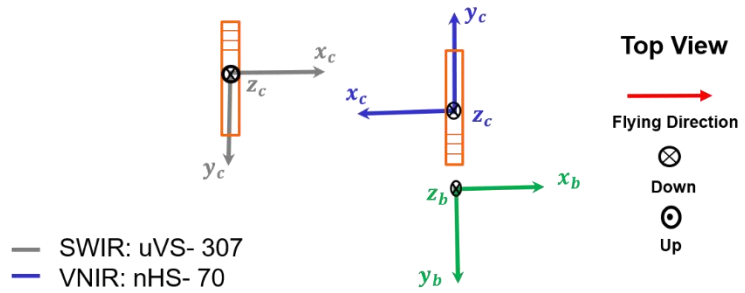


Figure 4.2 DJI M600P equipped with nHS-70 and uVS-307 system configuration

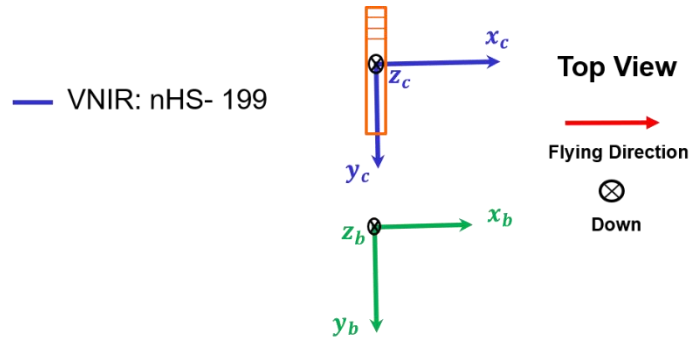


Figure 4.3 DJI M600P equipped with nHS-199 system configuration

Table 4.2 Headwall nominal boresight angles and lever arm components

<i>Sensor</i>	$\Delta\omega$ (degree)	$\Delta\phi$ (degree)	$\Delta\kappa$ (degree)	Δx (mm)	Δy (mm)	Δz (mm)
<i>nHS-70</i>	0	0	180	-20	60	80
<i>uVS-307</i>	0	0	0	-110	60	110
<i>nHS-199</i>	0	0	0	73	39	90

4.3.2 Dataset Description

There is a total of three push-broom line cameras and four flight collection dates used in this study. Table 4.3 shows the collection date, sensor, and corresponding flight parameters for each collection. For all the collection dates, there are between 4 and 5 ground control points, which are used as checkpoints for accuracy assessment in the experimental results. Figure 4.4 shows an example of the configuration of ground control points with the flight lines for the July 09th, 2019 nHS-70/uVS-307 data collection. The configuration of ground control points and trajectory are similar for all other collection dates. The five ground control targets are highly reflective checkerboard targets and were surveyed by a Topcon GR-5 GNSS receiver with an accuracy of 2-3cm. A sample of the raw uVS-307 SWIR and nHS-70 VNIR imagery over the calibration field with the reflective ground control targets is shown in Figure 4.5a and 4.5b respectively.

Table 4.3 Flight parameters for the different systems and collection dates

<i>Date</i>	<i>Sensor</i>	<i>Altitude Above Ground</i>	<i>Ground Speed</i>	<i>GSD</i>	<i>Side lap</i>	<i>Number of Flight Lines</i>
<i>July 09 2019</i>	<i>nHS-70</i>	<i>20 m</i>	<i>3 m/s</i>	<i>1.79 cm</i>	<i>60%</i>	<i>8</i>
		<i>40 m</i>	<i>6 m/s</i>	<i>3.58 cm</i>	<i>80%</i>	<i>10</i>
<i>Aug. 14 2019</i>		<i>20 m</i>	<i>3 m/s</i>	<i>1.79 cm</i>	<i>60%</i>	<i>6</i>
		<i>40 m</i>	<i>6 m/s</i>	<i>3.58 cm</i>	<i>80%</i>	<i>6</i>
<i>July 09 2019</i>	<i>uVS-307</i>	<i>20 m</i>	<i>3 m/s</i>	<i>1.95 cm</i>	<i>60%</i>	<i>8</i>
		<i>40 m</i>	<i>6 m/s</i>	<i>3.89 cm</i>	<i>80%</i>	<i>10</i>
<i>Aug. 14 2019</i>		<i>20 m</i>	<i>3 m/s</i>	<i>1.79 cm</i>	<i>60%</i>	<i>6</i>
		<i>40 m</i>	<i>6 m/s</i>	<i>3.58 cm</i>	<i>80%</i>	<i>6</i>
<i>May 29 2019</i>	<i>nHS-199</i>	<i>20 m</i>	<i>3 m/s</i>	<i>1.79 cm</i>	<i>60%</i>	<i>6</i>
		<i>40 m</i>	<i>6 m/s</i>	<i>3.58 cm</i>	<i>80%</i>	<i>6</i>
<i>July 11 2019</i>		<i>20 m</i>	<i>3 m/s</i>	<i>1.79 cm</i>	<i>60%</i>	<i>10</i>
		<i>40 m</i>	<i>6 m/s</i>	<i>3.58 cm</i>	<i>80%</i>	<i>8</i>

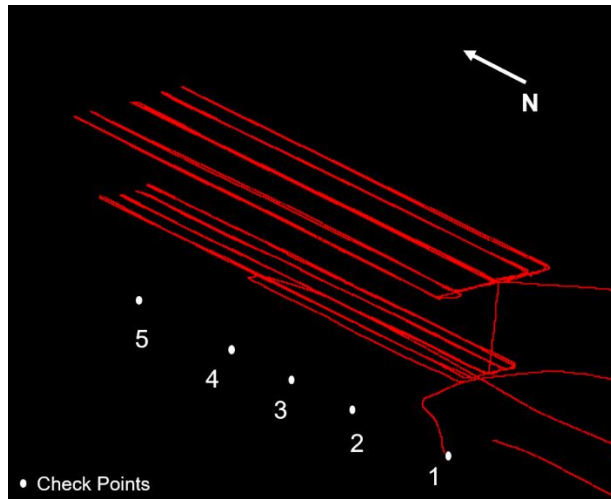


Figure 4.4 Ground control point locations and trajectory for the July 09th nHS-70/uVS-307 platform

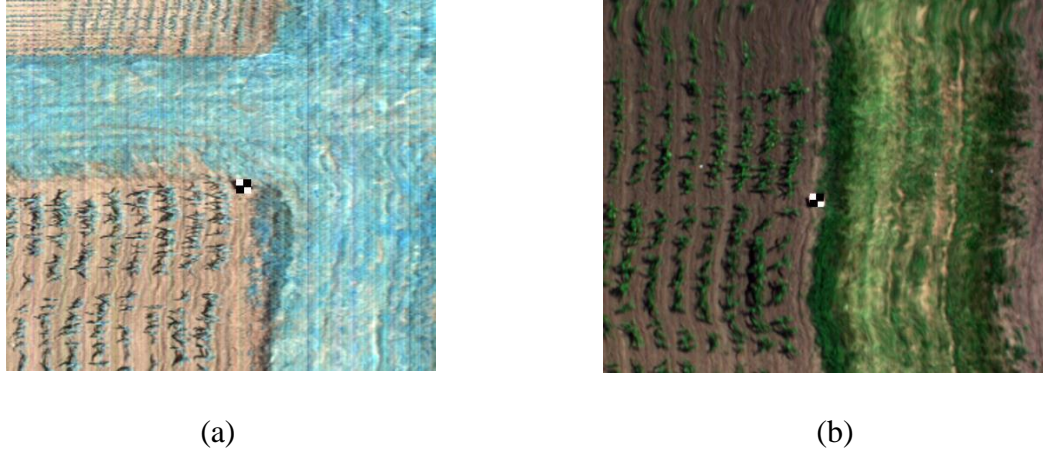


Figure 4.5 (a) Sample of the raw (a) uVS-307 SWIR and (b) nHS-70 VNIR imagery in the calibration field with enhanced representation of the targets.

4.3.3 Experimental Results and Analysis

In this section, the experimental objectives and results are discussed. The first objective of the experimental results is to evaluate the direct approach's ability to accurately estimate system calibration parameters and ground coordinates of checkpoints. The system parameters estimated include the X and Y components of the lever arm, boresight angles, and time delay. All imaging sensors, nHS-70, UVS-307, and nHS-199, along with all the collection dates are included in testing this objective. The next objective of the experimental results is evaluating the feasibility of the direct approach to handle a larger time delay while accurately estimating system parameters and ground coordinates of checkpoints. To test this objective, an artificial time delay of 200 ms is introduced to the nHS-70 and nHS-199 datasets. A 200 ms time delay was chosen because previous work indicated this was the amount found in other consumer-grade remote sensing platforms [50]. For the first two objectives, a comparison while considering/ignoring time delay is assessed. Relative accuracy is evaluated by examining the standard deviations of the checkpoints from the bundle adjustment. The absolute accuracy is evaluated by comparing the checkpoint XYZ ground coordinates to the survey reported XYZ ground coordinates. The last objective tests the feasibility of the indirect approach to accurately estimate system parameters and ground coordinates of checkpoints for line camera systems and is evaluated using the nHS-70 dataset.

4.3.3.1 Objective 1 – Feasibility of using the Direct Approach to Estimate Time Delay for Line Camera Systems

The results for the direct approach for the nHS-70, uVS-307, and nHS-199 are presented below. The results include experiments while considering/ignoring time delay. The estimated parameters while considering/ignoring time delay results for the nHS-70, uVS-307, and nHS-199 are shown in Table 4.4. The time delay estimated for each system and collection date ranges between and 4.1 and 10.4 ms. Although this does affect results, a time delay of this magnitude is considered relatively small. The lever arm components, ΔX and ΔY , and the boresight angles are also estimated during these calibrations and the nominal values are shown for comparison. Table 4.5 shows the correlation matrix produced from the direct approach bundle adjustment for the nHS-70 July 09th dataset. The correlations highlighted in red are above a chosen ± 0.85 threshold and are flagged as high. The lever arm ΔX and the boresight angle $\Delta\varphi$ as well as the lever arm ΔY and boresight angle $\Delta\omega$ have the highest correlation. This is expected based on the bias impact analysis. Furthermore, the time delay, Δt , is not correlated with any of the parameters which is an indication of sufficient variability in the angular and linear velocities. The correlation matrices for the remaining datasets as well as the scenarios for ignoring time delay have similar results.

Table 4.4 Estimated system parameter including the standard deviation and a-posteriori variance factor

	Time delay Δt (ms)	Lever arm ΔX (m)	Lever arm ΔY (m)	Boresight $\Delta\omega$ (°)	Boresight $\Delta\varphi$ (°)	Boresight $\Delta\kappa$ (°)	Square root of a-posteriori variance factor (pixel) $\hat{\sigma}_o$
Nominal Values							
nHS-70	0	-0.02	0.06	0	0	180	NA
uVS-307	0	-0.14	0.06	0	0	0	NA
nHS-199	0	0.07	0.04	0	0	0	NA
Estimated System Parameters while Ignoring Time Delay							
nHS-70 July 09th	NA	0.011 ± 0.008	0.067 ± 0.008	0.211 ± 0.016	0.013 ± 0.017	179.959 ± 0.030	0.820
nHS-70 Aug 14th	NA	-0.002 ± 0.009	0.057 ± 0.009	0.175 ± 0.021	0.026 ± 0.023	-179.904 ± 0.041	0.897

Table 4.4 continued

uVS-307 July 09th	NA	-0.108 \pm 0.01	0.060 \pm 0.010	0.293 \pm 0.020	0.419 \pm 0.026	0.389 \pm 0.701	0.604
uVS-307 Aug 14th	NA	-0.097 \pm 0.013	0.040 \pm 0.013	0.236 \pm 0.034	0.371 \pm 0.033	0.031 \pm 0.109	0.777
nHS-199 May 29th	NA	0.062 \pm 0.011	0.040 \pm 0.011	0.289 \pm 0.023	-1.232 \pm 0.023	-0.450 \pm 0.043	0.772
nHS-199 July 11th	NA	0.086 \pm 0.013	0.035 \pm 0.013	0.460 \pm 0.029	-1.126 \pm 0.030	-0.460 \pm 0.064	1.245
<i>Estimated System Parameters while Considering Time Delay (Direct Approach)</i>							
nHS-70 July 09th	5.912 \pm 0.340	0.030 \pm 0.006	0.066 \pm 0.006	0.210 \pm 0.012	-0.094 \pm 0.015	179.977 \pm 0.023	0.624
nHS-70 Aug 14th	10.464 \pm 0.851	0.007 \pm 0.008	0.050 \pm 0.008	0.163 \pm 0.017	-0.098 \pm 0.021	-179.938 \pm 0.035	0.727
uVS-307 July 09th	4.146 \pm 0.383	-0.097 \pm 0.008	0.060 \pm 0.007	0.295 \pm 0.015	0.309 \pm 0.028	0.0309 \pm 0.549	0.473
uVS-307 Aug 14th	9.876 \pm 0.903	-0.097 \pm 0.009	0.037 \pm 0.009	0.242 \pm 0.022	0.273 \pm 0.024	-0.021 \pm 0.072	0.514
nHS-199 May 29th	9.824 \pm 0.788	0.0787 \pm 0.011	0.050 \pm 0.011	0.316 \pm 0.022	-1.351 \pm 0.024	-0.480 \pm 0.040	0.729
nHS-199 July 11th	10.328 \pm 0.530	0.109 \pm 0.010	0.029 \pm 0.009	0.451 \pm 0.021	-1.315 \pm 0.027	-0.471 \pm 0.046	0.890

Table 4.5 Correlation matrix of system parameters for July 09th nHs-70 direct approach results

	ΔX	ΔY	ΔZ (not estimated)	$\Delta\omega$	$\Delta\varphi$	$\Delta\kappa$	Δt
ΔX	1						
ΔY	-0.025	1					
ΔZ (not estimated)	0	0	1				
$\Delta\omega$	-0.019	0.945	0	1			
$\Delta\varphi$	-0.880	0.075	0	0.042	1		
$\Delta\kappa$	-0.021	-0.041	0	-0.017	-0.071	1	
Δt	0.121	-0.158	0	-0.091	-0.480	0.271	1

A summary of the mean standard deviation of the checkpoints derived from the bundle adjustment as well as the mean, standard deviation, RMSE for the checkpoints when compared to surveyed ground coordinates for the nHS-70, uVS-307, and nHS199 are shown in Table 4.6. The relative accuracy while considering/ignoring time delay for the horizontal components shows minimal differences. The vertical relative accuracy shows a slight improvement while considering time delay. The overall horizontal components of the RMSE differences while considering/ignoring time delay are no more than 2 cm. The overall vertical component of the RMSE difference while considering and ignoring time delay is 1.2 cm for the nHS-70 August 14th dataset. Considering time delay showed only a slight improvement for the nHS-70 August 14th dataset in the vertical component. Overall, the horizontal and vertical component of the RMSE comparison while considering and ignoring time delay are minimal and can be expected in systems with relatively a small time delay. However, the vertical component for the uVS-307 July 09th dataset shows a 28.1 cm improvement while considering time delay compared to ignoring time delay. Even though there is minimal time delay in the uVS-307 system, there is still a huge improvement in the vertical direction for July 09th because of the tie point distribution of the dataset.

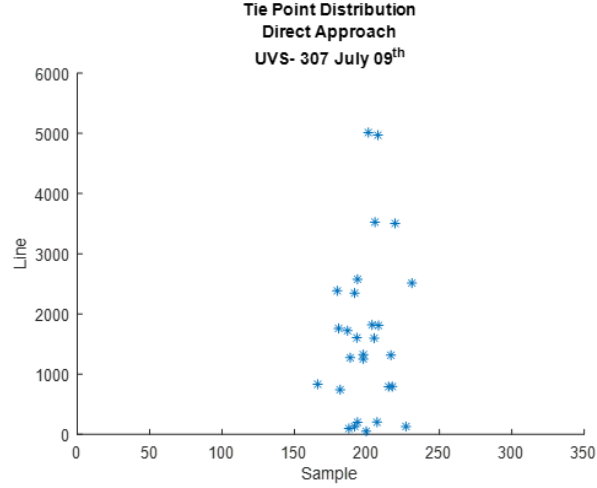
Figure 4.6a and 4.6b show the tie point distribution of the uVS-307 July 09th and August 14th dataset, respectively. The uVS- 307 July 09th dataset has an unfavorable tie point distribution for system calibration which leads to poor results while not considering time delay.

Table 4.6 Relative accuracy evaluated through the mean standard deviation of checkpoints derived from the bundle adjustment and the absolute accuracy measured through the Mean/Standard Deviation/RMSE of the differences between checkpoint and surveyed coordinates of the five checkpoints from direct approach

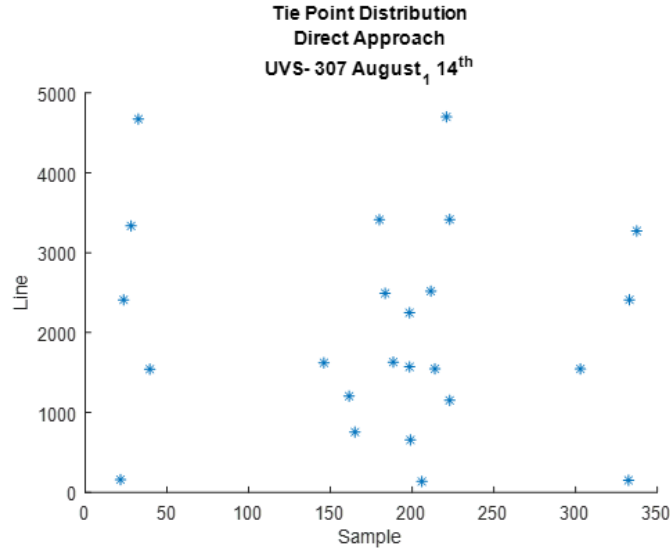
	Relative Accuracy			Absolute Accuracy								
	Mean STD X/Y/Z (m)			Mean X/Y/Z (m)			STD X/Y/Z (m)			RMSE X/Y/Z (m)		
nHS-70 July 09th (Δt estimated)	0.004	0.004	0.022	-0.018	0.011	-0.006	0.006	0.008	0.029	0.019	0.013	0.026
nHS-70 July 09th (Ignoring Δt)	0.005	0.006	0.030	-0.017	0.010	0.004	0.007	0.010	0.029	0.018	0.013	0.026
RMSE Difference (time delay estimated – ignoring)										0.001	0	0
nHS-70 August 14th (Δt estimated)	0.005	0.005	0.030	-0.007	0.007	-0.036	0.005	0.007	0.035	0.008	0.008	0.048
nHS-70 August 14th (Ignoring Δt)	0.006	0.006	0.037	-0.005	0.007	-0.048	0.007	0.008	0.040	0.008	0.010	0.060
RMSE Difference (time delay estimated – ignoring)										0	-0.002	-0.012
uVS-307 July 09th (Δt estimated)	0.006	0.007	0.190	-0.020	0.010	-0.093	0.005	0.008	0.114	0.020	0.012	0.138
uVS-307 July 09th (Ignoring Δt)	0.007	0.009	0.209	-0.018	0.003	0.365	0.006	0.011	0.231	0.019	0.010	0.419
RMSE Difference (time delay estimated – ignoring)										0.001	0.002	-0.281

Table 4.6 continued

uVS-307 August 14th (Δt estimated)	0.005	0.005	0.043	-0.006	0.006	-0.051	0.005	0.004	0.060	0.008	0.007	0.074
uVS-307 August 14th (Ignoring Δt)	0.008	0.007	0.065	-0.006	0.006	-0.035	0.004	0.006	0.057	0.007	0.008	0.062
RMSE Difference (time delay estimated – ignoring)										0.001	-0.001	0.012
nHS-199 May 29th (Δt estimated)	0.007	0.007	0.041	-0.003	0.032	0.024	0.004	0.009	0.029	0.005	0.033	0.036
nHS-199 May 29th (Ignoring Δt)	0.008	0.008	0.043	0.001	0.031	0.034	0.004	0.009	0.042	0.004	0.032	0.051
RMSE Difference (time delay estimated – ignoring)										0.001	0.001	-0.015
nHS-199 July 11th (Δt estimated)	0.008	0.007	0.041	0.017	0.006	-0.036	0.013	0.008	0.059	0.021	0.009	0.064
nHS-199 July 11th (Ignoring Δt)	0.011	0.009	0.057	0.014	0.008	-0.023	0.009	0.010	0.036	0.017	0.012	0.040
RMSE Difference (time delay estimated – ignoring)										0.004	-0.003	0.024



(a)



(b)

Figure 4.6 Tie point distribution for (a) uVS-307 July 09th dataset and (b) uVS-August 14th dataset.

4.3.3.2 Objective 2 – Feasibility of using the Direct Approach with Larger Artificial Time Delay for Line Camera Systems

The next section presents results for the direct approach while introducing a 200 ms artificial time delay for the nHS-70 and nHS-199 systems. The purpose of introducing this artificial time delay is to analyze the direct approach's performance when having a larger time delay in line camera systems. The estimated parameters while considering/ignoring time delay for the nHS-70

and nHS-199 are displayed in Table 4.7. The time delay estimated for July 09th and August 14th datasets without the artificial time delay introduced was 5.912 and 10.464 ms, respectively. The time delay estimated for the July 09th and August 14th with a 200 ms artificial time delay introduced are -194.088 and -189.535 ms, respectively. The time delay estimated for May 29th and July 11th datasets without the artificial time delay introduced was 9.824 and 10.328 ms, respectively. The time delay estimates for the July 09th and August 14th with a 200 ms artificial time delay introduced are -190.160 and -189.672 ms, respectively. These results show that the direct approach is accurately estimating the time delay in the system. Furthermore, for all datasets while ignoring time delay after introducing the 200 ms artificial time delay show a very large increase (and further from the nominal values) in the estimated lever arm in the flying direction (lever arm X) with the remaining system parameters very close to the values produced before introducing the artificial time delay.

Table 4.7 Estimated system parameter including the standard deviation and a-posteriori variance factor with 200 ms artificial time delay introduced

	Time delay Δt (ms)	Lever arm ΔX (m)	Lever arm ΔY (m)	Boresight $\Delta \omega$ (°)	Boresight $\Delta \phi$ (°)	Boresight $\Delta \kappa$ (°)	Square root of a-posteriori variance factor (pixel) $\hat{\sigma}_o$
<i>Previously Estimated Parameters using the Direct Approach (without artificial time delay)</i>							
nHS-70 July 09th	5.912 ± 0.340	0.030 ± 0.006	0.066 ± 0.006	0.210 ± 0.012	-0.094 ± 0.015	179.977 ± 0.023	0.624
nHS-70 Aug 14th	10.464 ± 0.851	0.007 ± 0.008	0.050 ± 0.008	0.163 ± 0.017	-0.098 ± 0.021	-179.938 ± 0.035	0.727
nHS-199 May 29th	9.824 ± 0.788	0.0787 ± 0.011	0.050 ± 0.011	0.316 ± 0.022	-1.351 ± 0.024	-0.480 ± 0.040	0.729
nHS-199 July 11th	10.328 ± 0.530	0.109 ± 0.010	0.029 ± 0.009	0.451 ± 0.021	-1.315 ± 0.027	-0.471 ± 0.046	0.890
<i>Estimated System Parameters while Ignoring Time Delay (Artificial time delay of 200 ms introduced)</i>							
nHS-70 July 09th	NA	0.516 ± 0.158	-0.060 ± 0.158	0.060 ± 0.334	-3.215 ± 0.343	179.751 ± 0.620	17.094
nHS-70 Aug 14th	NA	0.091 ± 0.103	-0.059 ± 0.099	0.138 ± 0.230	-1.965 ± 0.245	179.416 ± 0.440	9.569
nHS-199 May 29th	NA	0.411 ± 0.160	0.112 ± 0.164	0.617 ± 0.340	-3.587 ± 0.334	-0.839 ± 0.616	11.200
nHS-199 July 11th	NA	0.720 ± 0.201	-0.005 ± 0.196	0.412 ± 0.443	-5.046 ± 0.451	-0.408 ± 0.960	18.754
<i>Estimated System Parameters while Considering Time Delay (Direct Approach) (Artificial time delay of 200 ms introduced)</i>							
nHS-70 July 09th	-194.088 ± 0.340	0.030 ± 0.006	0.066 ± 0.006	0.210 ± 0.012	-0.094 ± 0.015	179.977 ± 0.023	0.624
nHS-70 Aug 14th	-189.535 ± 0.851	0.006 ± 0.007	0.050 ± 0.007	0.163 ± 0.017	-0.097 ± 0.021	-179.938 ± 0.034	0.727
nHS-199 May 29th	-190.160 ± 0.785	0.080 ± 0.0105	0.050 ± 0.011	0.316 ± 0.022	-1.351 ± 0.024	-0.480 ± 0.040	0.727
nHS-199 July 11th	-189.672 ± 0.530	0.109 ± 0.010	0.029 ± 0.009	0.451 ± 0.021	-1.315 ± 0.027	-0.471 ± 0.046	0.890

The relative accuracy is evaluated by the standard deviations reported from the bundle adjustment and the absolute accuracy is evaluated by comparing the ground coordinates of the

checkpoints to the surveyed ground coordinates and both are shown in Table 4.8. The differences in the RMSE values while considering/ignoring time delay are much larger now. When the artificial time delay of 200 ms was introduced, there is an overall horizontal and vertical improvement while considering time delay compared to ignoring time delay. The RMSE horizontal component improvement from using the direct approach to estimate time delay is approximately 2.9 and 9.6 cm for the July 09th and August 14th dataset, respectively. These differences are approximately 2-5 times that of the GSD of the system at the 20 m flying height. The vertical component shows an even larger improvement by using the direct approach for estimating time delay, with as much as 43.2 cm difference. The horizontal components of the RMSE differences range from 3.9 to 14 cm for the May 29th and July 11th datasets. The vertical component of the RMSE differences are 49.2 and 105 cm for the May 29th and July 11th datasets, respectively. This shows a very large improvement for the direct approach over ignoring time delay when a system has an approximate 200 ms time delay. Furthermore, even though there was a large time delay to estimate in the system, the overall mean, standard deviation, and RMSE of the direct approach with the artificial 200 ms time delay was almost the same as the direct approach without an artificial time delay. For example, the RMSE XYZ components while considering time delay for the nHA-199 July 11th without the artificial time delay, shown in Table 4.6, are identical to the RMSE XYZ components while considering time delay with the artificial time delay introduced. This shows that the direct approach accurately estimates the time delay and achieves similar absolute accuracy whether the time delay in the system is minimal or significant.

Table 4.8 Relative accuracy evaluated through the mean standard deviation of checkpoints derived from the bundle adjustment and the absolute accuracy measured through the Mean/Standard Deviation/RMSE of the differences between checkpoint and surveyed coordinates of the five checkpoints from direct approach

	Relative Accuracy			Absolute Accuracy								
	Mean STD X/Y/Z (m)			Mean X/Y/Z (m)			STD X/Y/Z (m)			RMSE X/Y/Z (m)		
nHS-70 July 09th (Δt estimated)	0.004	0.004	0.022	-0.018	0.011	-0.006	0.006	0.008	0.029	0.019	0.013	0.026
nHS-70 July 09th (Ignoring Δt)	0.114	0.115	0.568	-0.013	0.048	-0.169	0.051	0.109	0.476	0.048	0.109	0.458
RMSE Difference (time delay estimated – ignoring)										-0.029	-0.096	-0.432
nHS-70 August 14th (Δt estimated)	0.005	0.005	0.030	-0.007	0.007	-0.036	0.005	0.007	0.035	0.008	0.009	0.048
nHS-70 August 14th (Ignoring Δt)	0.064	0.065	0.380	-0.027	-0.011	0.146	0.035	0.081	0.165	0.041	0.073	0.207
RMSE Difference (time delay estimated – ignoring)										-0.033	-0.064	-0.159
nHS-199 May 29th (Δt estimated)	0.007	0.007	0.040	-0.003	0.032	0.024	0.004	0.009	0.030	0.005	0.033	0.036
nHS-199 May 29th (Ignoring Δt)	0.111	0.111	0.581	-0.021	0.058	0.067	0.043	0.057	0.573	0.044	0.078	0.528
RMSE Difference (time delay estimated – ignoring)										-0.039	-0.045	-0.492
nHS-199 July 11th (Δt estimated)	0.017	0.006	-0.036	0.017	0.006	-0.036	0.013	0.008	0.059	0.021	0.009	0.064
nHS-199 July 11th (Ignoring Δt)	0.062	0.013	0.194	0.062	0.013	0.194	0.097	0.166	1.227	0.107	0.149	1.114
RMSE Difference (time delay estimated – ignoring)										-0.086	-0.140	-1.050

4.3.3.3 Objective 3 – Feasibility of using the Indirect Approach to Estimate Time Delay for Line Camera Systems

The feasibility of the indirect approach to estimate time delay for line camera systems is discussed in this section. The objective was tested on the nHS-70. Recall from the bias impact analysis, that the indirect approach requires a single flying height so that the correlation between the lever arm in the flying direction and the time delay is exploited. The estimated parameters for the indirect approach for the nHS-70 July 09th and August 14th 40 m flight lines are presented in Table 4.9. The estimated lever arm in the flying direction are extremely large compared to the nominal values. This is expected since the time delay is being absorbed. The correlation matrix of system parameters for the July 09th dataset is shown in Table 4.10. Here, a problem was identified with ΔX and $\Delta\phi$ being 100% correlated. With this extreme correlation, system parameters cannot accurately be estimated and step 2 of the indirect approach was not performed. Even though there is variation in x_i , which helps to decouple lever arm ΔX and $\Delta\phi$, the variation in ground coordinates from changes in $\frac{x_i^2}{c^2}$ are minimal compared to the changes in ground coordinates produced by changes in the flying height. The range in $\frac{x_i}{c}$ directly relates to the AFOV of the system. For line cameras, the AFOV is relatively small. The bias impact analysis reveals that this correlation was expected and changes in flying height are needed to decouple the lever arm and boresight angles. Therefore, the indirect approach should not be used for line camera system since a single flying height is needed and the AFOV is too small. The direct approach is recommended for estimating time delay during system calibration for line camera systems.

Table 4.9 Estimated system parameter including the standard deviation and a-posteriori variance factor

	Time delay Δt (ms)	Lever arm ΔX (m)	Lever arm ΔY (m)	Boresight $\Delta\omega$ (°)	Boresight $\Delta\phi$ (°)	Boresight $\Delta\kappa$ (°)	Square root of a-posteriori variance factor (pixel) $\hat{\sigma}_o$
Nominal Values							
nHS-70	0	-0.02	0.06	0	0	180	NA
<i>Indirect Approach</i>							
July 09th 40 m flight line Operation 1	NA	1.667 \pm 0.845	0.06 (fixed)	-0.050 \pm 0.283	-2.297 \pm 1.189	179.934 \pm 0.0401	0.789
Aug. 14th 40 m flight line Operation 1	NA	-1.612 \pm 1.025	0.06 (fixed)	1.049 \pm 0.609	2.291 \pm 1.438	-179.953 \pm 0.054	0.881

Table 4.10 Correlation matrix of system parameters for July 09th nHS-70 indirect approach results

	ΔX	ΔY (not estimated)	ΔZ (not estimated)	$\Delta\omega$	$\Delta\phi$	$\Delta\kappa$	Δt
ΔX	1						
ΔY (not estimated)	0	1					
ΔZ (not estimated)	0	0	1				
$\Delta\omega$	0.316	0	0	1			
$\Delta\phi$	-1.000	0	0	-0.316	1		
$\Delta\kappa$	0.055	0	0	0.232	-0.055	1	
Δt	0	0	0	0	0	0	1

4.4 Conclusions and Recommendations for Future Research

UAVs equipped with GNSS/INS-assisted imaging systems are often used for accurate 3D reconstruction. Spatial and temporal system calibration is crucial for deriving accurate 3D spatial information. In this paper, the direct and indirect approaches were presented and analyzed for line camera systems. Optimal flight configurations were derived through a thorough bias impact analysis for line camera systems. It was determined through the bias impact analysis that the indirect approach was not appropriate due to the small AFOV of line camera systems and single flying height requirement. This hypothesis was then confirmed through the experimental results. The direct approach results for all systems used in this study showed that the time delay can be accurately estimated both for small and larger delays. The results show that even when there is a relatively small time delay in the system, and the time delay is ignored and there is not favorable tie point distribution, then the accuracy of the results will suffer. Therefore, it is suggested that even when a small time delay in the system is suspected that the direct approach is used and time delay is considered and estimated. The results also show that when a larger time delay is present in line camera systems, (which was shown through introducing an artificial time delay in the systems used), ignoring time delay will result in poor system calibration parameter estimates and degrade absolute and relative accuracy significantly. In conclusion, the direct approach is capable of accurately estimating the time delay in line camera systems as well as improving absolute accuracy both when small and large time delays are present in the system. Additionally, all of these results were conducted without the use of ground control points. Hence, the direct approach can produce highly accurate system calibration parameters for line camera systems without the use of GCP.

Future work will focus on automating the tie point measurement process. In this study, the results show that tie point distribution is extremely important for accurate estimates of system parameters. It can be difficult to ensure both a large number and good distribution while using manually-identified tie points. Therefore, future work will concentrate on both extracting automated tie point from frame and line camera imagery as well as incorporating those tie points into the direct approach bundle adjustments. Also, future work will focus on verifying the direct approach for line camera sensors onboard a variety of platforms such as satellite and airborne.

5. SYSTEM CALIBRATION WITH TIME DELAY ESTIMATION FOR UAV-BASED FRAME AND LINE CAMERAS USING AUTOMATICALLY-DERIVED TIE POINTS

This research article is in the internal review stages and is planned for submission to the International Society for Photogrammetry and Remote Sensing journal.

Authors: LaForest, L.; Hasheminasab, S.M.; Zhou, T.; Habib, A.

Author Contributions: All authors contributed to the work. Conceptualization, L.L., S.M.H., T.Z. and A.H.; Formal analysis, L.L., S.M.H., T.Z. and A.H.; Methodology, Imaging Matching- S.M.H., T.Z., and A.H. System Calibration Adjustment- L.L and A.H.; Software, L.L., S.M.H. and T.Z.; Writing – original draft, L.L. and S.M.H.; Writing – review & editing, A.H.

Abstract: Unmanned aerial vehicles (UAVs) equipped with global navigation satellite systems/inertial navigation systems (GNSS/INS) and imaging systems are used for a variety of applications requiring accurate 3D reconstruction of object space. Geometric system calibration is crucial for producing accurate 3D data from UAV imaging systems. Geometric system calibration is comprised of two objectives – spatial and temporal calibration – and has been conducted with and without the need for ground control points (GCPs) and with and without automatically-derived tie points. However, research has yet to focus on automated spatial and temporal calibration for frame and line camera systems without the need for GCPs. This paper presents an automated spatial and temporal calibration approach that produces highly accurate system calibration parameters without the need for GCPs or manually-measured tie points for both frame and line camera systems. The matching strategy used in this study to establish conjugate features among overlapping frame camera images, is based on a traditional Structure from Motion (SfM) technique. On the other hand, a new strategy which takes advantages of ortho-rectified images generated for each flight line is introduced for automated feature matching for line cameras. The automatically-extracted tie points are used in a bundle adjustment with self-calibration (while considering spatial and temporal system parameters) to produce highly accurate system parameters. The results show that the bundle adjustment with self-calibration and matching approach presented in this research was capable of producing the same level of absolute accuracy compared to using manually-measured tie points for both frame camera and line camera systems. However, relative accuracy was worse for the automatically-derived tie points. The also results show that the automated system calibration approach presented in this paper can be applied to systems with either significant or

minimal time delay and still achieve accurately reconstructed 3D object space and produce reliable estimates of system parameters.

5.1 Introduction

Unmanned aerial vehicles (UAVs) equipped with global navigation satellite systems/inertial navigation systems (GNSS/INS) and imaging systems are used in a variety of industries for accurate 3D reconstruction. UAVs provide ease of deployment and variety of choices for imaging and GNSS/INS sensors while collecting high temporal and spatial resolution data [24]. The use of UAVs in agricultural applications has expanded rapidly in recent years due to their relatively low cost and improved spatial and temporal resolution [16]. In addition, it is possible to equip UAVs with a variety of imaging sensors. These factors have increased the effectiveness of UAVs as a tool for precision agriculture and crop monitoring [18-21]. However, to produce highly accurate 3D data, system calibration is needed for consumer-grade UAV imaging systems. In this paper, ‘consumer-grade’ refers to cameras that require system calibration by the user instead of by the manufacturer or other high-end laboratory settings and UAV systems that are equipped with relatively low-cost GNSS/INS units.

Geometric system calibration includes estimating internal characteristics of the sensor and system mounting parameters as well as time delay in the system, known as spatial and temporal calibration, respectively. Due to the fact that geometric system calibration is vital to achieving higher levels of accuracy by a given system, it has been a major focus in existing research. Spatial and temporal system calibration has been performed on a variety of frame camera imaging sensors with many requiring ground control points (GCPs) to achieve the level of desired accuracy [10, 15]. Establishing such ground targets is expensive and labor intensive, and more importantly, the distribution and number of GCPs are usually less than optimal to provide adequate control for determining system calibration parameters. To overcome this limitation, there has also been recent research focusing on spatial and temporal calibration for frame cameras without the need for GCPs [50]. Yet, even without the need for GCPs, many techniques have only been applied with manually-measured tie points in overlapping images. Manual tie point measurements is known to be accurate but is also very time consuming and labor intensive. Consequently, recent research has focused on producing high quality, automatically-derived tie points from frame camera systems [32, 45]. Furthermore, when incorporating a large amount of automatically-derived tie points,

close attention must be given to the least squares adjustment implemented in the bundle adjustment process. There are several methods of least squares adjustments that will lead to the same solution. However, depending on the application or implementation, one method may have advantages over another. Therefore, a variety of least squares adjustment solutions with large numbers of observations and/or unknowns have been described in previous literature [1, 54, 55]. However, even with previous work in system calibration, automated tie point generation, and adjustment implementation, there is still a gap in research that focuses on a fully-automated spatial and temporal bundle adjustment with self-calibration without the need for GCPs for both frame and line camera systems.

Frame and line camera systems capture imagery with different procedures. The difference in how frame and line cameras capture imagery greatly affects the image matching process. The data acquisition mechanisms and sample imagery for frame and line cameras are depicted in Figure 5.1. As shown in Figure 5.1a-b, the main difference between frame and line camera is that the frame camera's scene is captured in one instance by a single image whereas the line camera's scene is built by multiple scan lines captured sequentially. Here, a scene is considered as a 2D coverage area of the ground. Given this geometry, frame camera's image coordinates will consist of both x and y values that are variable depending on image point location which is bounded by the sensor's angular field of view (AFOV). However, line camera's y image coordinates will have variable values but x will always be constant depending on the camera alignment to the sensor's focal plane. These differences cause the system calibration and automated tie point generation process to differ for frame and line camera systems. Due to the turbulence in the UAV's trajectory, concatenating sequential scan lines in line cameras results in wavy pattern in raw scenes compared to frame camera systems whose scene is captured in one instance. Figures 5.1c and 5.1d show a sample overlapping images/scenes for frame/line cameras. From Figures 5.1c and 5.1d, one can observe that unlike frame cameras images, in line camera scenes, corresponding features look different among raw scenes, impeding the process of automatically finding conjugate features in overlapping scenes.

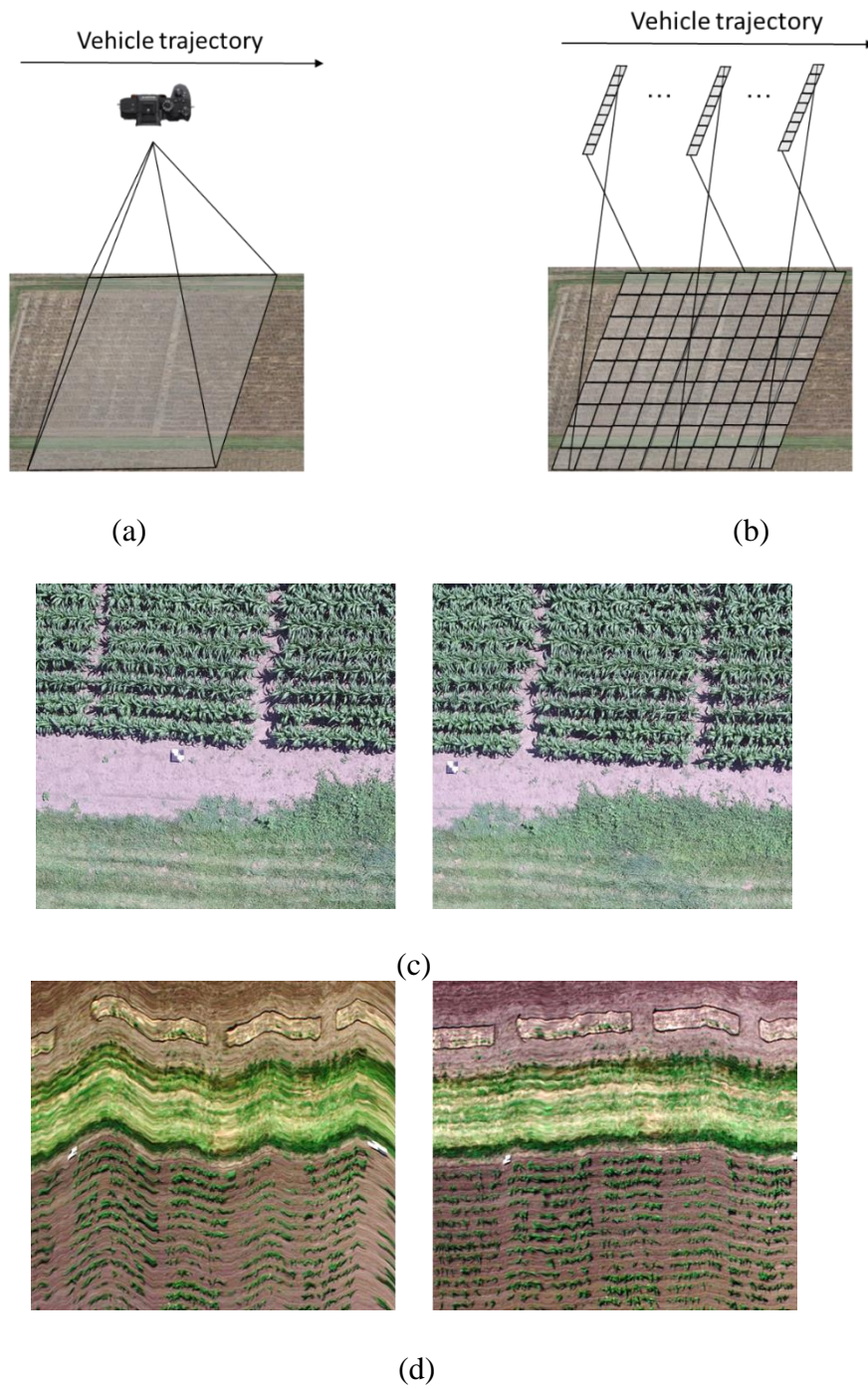


Figure 5.1 Illustration of (a) frame camera and (b) line camera sensor data acquisition and overlapping sample scenes for frame (c) and line (d) camera imagery

For a robust estimation of system calibration parameters with minimum possible correlation between such parameters, specific flight missions are required. As discussed in [50], to conduct spatial and temporal calibration, it is recommended to derive the system parameters using opposite flying directions at different flying heights, as well as having a variation in the linear and angular velocities. Data acquisition at multiple flying heights results in imagery with differing scales, which in turn adversely affects the automatic feature extraction and matching in both frame and line cameras. Figure 5.2 illustrates raw imagery acquired from two different flying heights, i.e., 20 m and 40 m, for both frame and line cameras. As shown in this figure, conjugate features look different in overlapping images/scenes with significant scale difference.

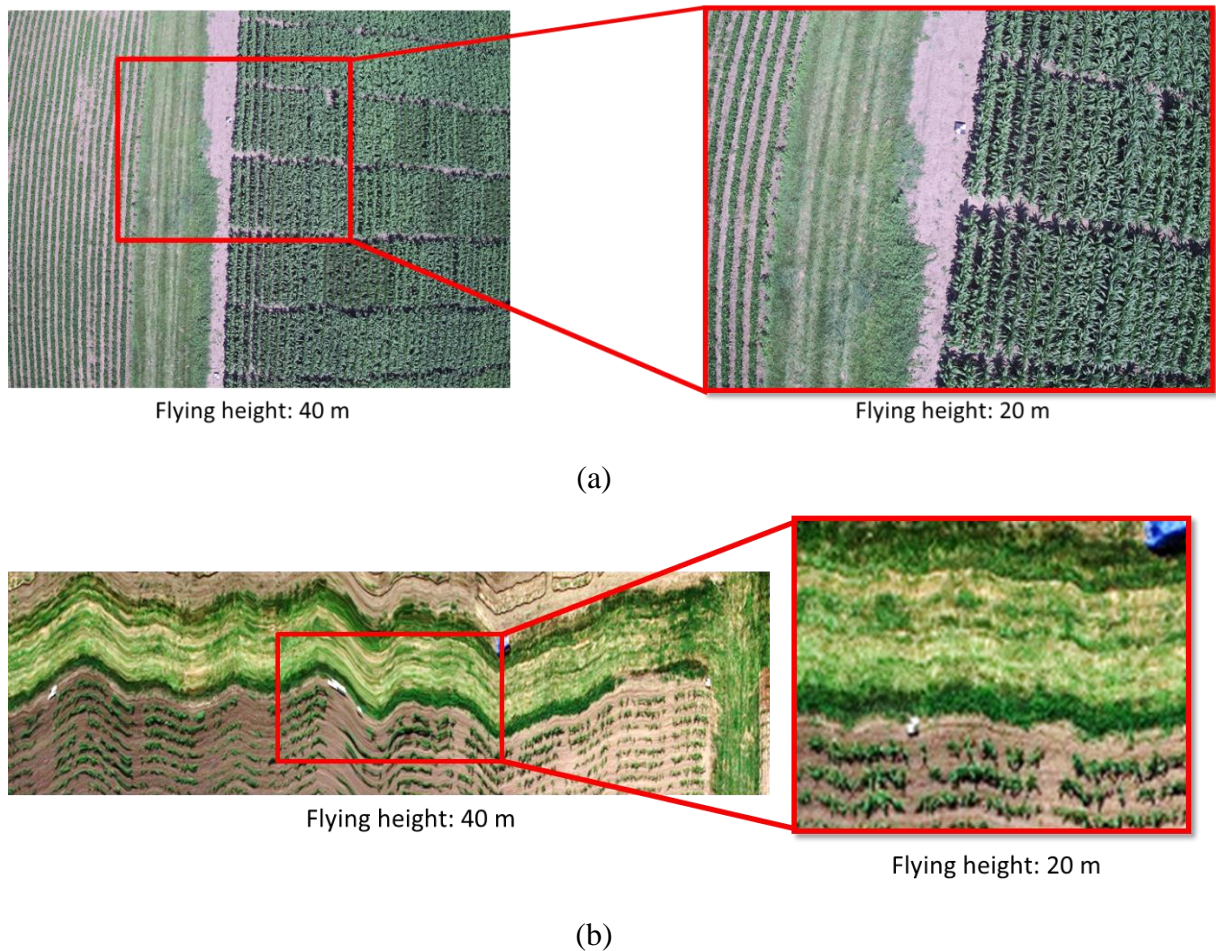


Figure 5.2 Scale difference in sample overlapping imagery captured from 40 m and 20 m flying heights, (a) frame images, and (b) line scenes.

Most of the existing body of literature uses GCPs with the help of manually-measured tie points for conducting bundle adjustment with self-calibration. In recent years, several automated feature extraction and matching algorithms have been developed for both frame [44, 54] and line cameras [55, 56]. However, the majority of these techniques show poor performance when dealing with frame camera images with significant scale difference, or UAV-based line camera scenes where the wavy pattern in raw imagery is pronounced.

This study focuses on fully-automated spatial and temporal calibration of frame and line cameras onboard UAV-based imaging systems without the need for GCPs. First, a review of previous work dealing with spatial and temporal calibration for frame and line camera systems, automated tie point generation, and adjustment implementation are presented. Next, the system specifications and dataset description are provided. The methodology starts by presenting the Structure from Motion (SfM) approach used for automated feature extraction and matching for frame cameras. Next, a new automated feature extraction and matching strategy for line camera systems is presented which applies SIFT algorithm on partially ortho-rectified images instead of raw images. Here, the term “partially”, refers to the fact that only nominal system calibration parameters, e.g. lever-arm components, boresight angles, and time delay between the camera and GNSS/INS unit, are used in this procedure. Then, the mathematical model used for spatial and temporal calibration as well as the implemented bundle adjustment to incorporate a large number of tie points is presented. The experimental results for frame and line camera UAV systems is then presented. Lastly, conclusions and recommendations for future work are discussed.

5.2 Related Work

Spatial and temporal system calibration is essential for accurate 3D reconstruction of consumer-grade UAV imaging systems leading to much research over the years. Spatial calibration has been extensively covered in past research [1, 30, 4, 5, 7]. However, temporal calibration has been addressed to a lesser extent. Chiang et al. [12] proposed a calibration method to estimate the magnitude of exposure time delay for a UAV-based imaging system. The authors introduced a two-step approach for estimating time delay. First, exterior orientation parameters (EOPs) were obtained through indirect geo-referencing with the help of GCPs. Then, the differences between such EOPs and the interpolated GNSS/INS position and orientation of the inertial measurement unit (IMU) body frame were derived. Those differences were then used in a calibration algorithm

to solve for lever arm components, boresight angles, and time delay. Blazaquez, M. [15] introduced a one-step approach for ‘spatio-temporal’ calibration of multi-sensor systems. This approach focused on modifying the sensor model to include a time synchronization parameter. Rehak and Skaloud [10] worked on time synchronization of consumer-grade cameras on micro aerial vehicles (MAVs). The authors also introduced a one-step approach to modify the mathematical model to include time delay as a parameter in the bundle adjustment. Yet, for the above temporal calibration research, all required GCPs for acceptable absolute accuracy and focused on frame camera systems. LaForest et al. [50] presented two one-step approaches – direct and indirect – for estimating time delay during system calibration for frame camera systems without the need for GCPs. The direct approach modified existing collinearity equations to incorporate time delay as a system parameter. The indirect approach exploited the impact of bias analysis for system parameters and their correlations to solve for time delay indirectly using existing bundle block adjustment software. Even though frame camera systems have been researched for spatial and temporal calibration, line camera system calibration has primarily focused on spatial calibration. Kocaman et al. [57] focused on modifying the adjustable parameters for self-calibration triangulation of airborne linear array cameras. Habib et al. [9] performed rigorous boresight calibration for a hyperspectral line camera equipped with a GNSS/INS unit onboard a UAV. Current research in system calibration for line camera consumer-grade systems have neglected temporal calibration.

System calibration using a bundle block adjustment requires image coordinates measurements of tie points, among other potential observations and unknowns. Manual tie points are known to be accurate but very time consuming. To address this challenge, some research has focused on self-calibration so that manual measurements can be decreased or eliminated. Habib et al. [5, 6] focused on camera and LiDAR self-calibration using straight lines and planar patches. Recent research has focused on image matching to address this challenge. He et al. [32] focused on using SfM for automated aerial triangulation for frame UAV- based systems. Hasheminasab et al. incorporated GNSS/INS information to aid the SfM process for images captured over agricultural fields consisting of repetitive texture patterns. Yet, there is still a gap for fully-automated spatial and temporal calibration for line camera systems without the need for GCPs.

Special attention must be given to the least squares adjustment implemented in the bundle block adjustment when incorporating a large amount of automatically-derived tie points. Different least squares adjustments can lead to the same solution but depending on the application and

implementation, one may have advantages over another. Two methods of least squares solutions considered for bundle block adjustments are the Gauss-Markov model and the mixed least squares model, sometimes referred to as Gauss-Helmert or condition equations with parameters [58]. The main difference in these adjustment solutions are how the observations, unknowns, and prior uncertainties are treated. For the Gauss-Markov model, any unknown parameter with prior information adds corresponding pseudo observations. In the case of system calibration, this may be parameters such as GNSS/INS-based trajectory information or GCPs. It should be noted that using this model increases the size of the normal equations dramatically since all parameters with prior information are considered as unknowns. The Gauss-Helmert model does not consider parameters with prior information as unknowns but instead they are treated as weighted observations. This drastically decreases the size of the normal equations. This decrease in the size of the normal equations is important when incorporating large amount of tie points. Lastly, as discussed by Mikhail [59], if the adjustment is dealing with block diagonal matrices then the normal equations may be sequentially formed. This is essential when incorporating a large amount of automatically-derived tie points.

Spatial calibration has been investigated for both frame and line camera systems. However, temporal calibration has not been demonstrated for consumer-grade line camera systems. Furthermore, past research requires the use of GCPs to achieve an acceptable absolute accuracy. Past research has focused on automated spatial system calibration but only for frame camera systems and neglected temporal calibration. This research focuses on a fully-automated bundle adjustment with self-calibration including spatial and temporal system parameters for frame and line camera systems without the use of GCPs.

5.3 System Specifications and Dataset Description

This study implemented an RGB frame camera and hyperspectral line camera equipped with GNSS/INS units onboard UAV platforms. Both systems relied on the Applanix APX-15 UAV v2 GNSS/INS unit for direct geo-referencing with a predicted positional accuracy of 2-5 cm and heading and roll/pitch accuracy of 0.080 and 0.025°, respectively [41]. The Dà-Jiāng Innovations (DJI) M200 [39] frame camera imaging system employed a FLIR Duo Pro R 640 combined thermal and RGB image sensor. The Uncooled VOx Microbolometer thermal sensor array was 640×512 with a pixel size of 17 μm and had a nominal focal length of 19mm. The RGB visible

sensor array size was 4000×3000 , with a pixel size of $1.85 \mu\text{m}$ and a nominal focal length of 8 mm and has a field of view of 56° [42]. Figure 5.3 shows the FLIR Duo Pro R and APX-15 configuration onboard the M200 UAV, and illustrates the coordinate systems for the IMU and camera and body frames. The FLIR Duo Pro R utilized a mobile-phone based app to set camera parameters via Bluetooth. The mobile-phone based app provides the ability to set the capture interval for the camera and to start and stop triggering. Event feedback to the APX was provided directly by the FLIR Duo Pro R using the “Frame Sync” option. This option output a low voltage transistor to transistor logic (3.3V) pulse that was wired directly to the event input of the APX-15.

The Matrice 600 Pro (M600P) was the hyperspectral line camera UAV platform used [40]. The DJI M600P platform was equipped with two different line camera sensors. The Headwall’s Nano-hyperspectral and shortwave infrared sensors. The shortwave infrared sensor was not used in this study. The Nano-hyperspectral sensor will be referred to as ‘nHS’ along with the serial number ‘70’ – nHS-70. The nHS-70 line camera sensor operates at the visible and near-infrared. The nHS-70 sensor covers 270-273 spectral bands ranging between 398 – 1000 nm with a band width of 2.2 nm. The scan line consists of 640 pixels and has a detector pitch of $7.5 \mu\text{m}$ [52]. The sensor has a focal length of 8.2 mm resulting in a field of view of approximately 31° along the scan line. The approximate ground sampling distance (GSD) values of the nHS-70 sensor are 1.79 and 3.58 cm when flying at 20 and 40 m flying height, respectively. An image of the DJI M600P equipped with the nHS-70, along with the orientation of the sensor and body coordinate system of the platform is shown in Figure 5.4. The system records a pulse per second (PPS), frame index count per line, and position and orientation along with the UTC (at 100 Hz), and Nano clock count. The link between the pulse per second from the APX, frame index count, and UTC time is used to evaluate the timestamp for each scan line. However, a time delay can still exist between the GNSS/INS timestamp and the image exposure time. Table 5.1 outlines the nominal boresight and lever arm values for the FLIR RGB frame camera and nHS-70 line camera systems. The FLIR RGB frame camera system and the nHS-70 hyperspectral line camera system each had one collection date used in this study. Table 5.2 shows the flight parameters and dataset description for each imaging system. For both the collection dates, there are 5 ground control points, which are used as checkpoints for accuracy assessment in the experimental results. The five ground control targets are checkerboard targets and were surveyed by a Topcon GR-5 GNSS receiver with an

accuracy of 2-3cm. It should be noted that the image coordinate measurements for checkpoints were manually-measured.

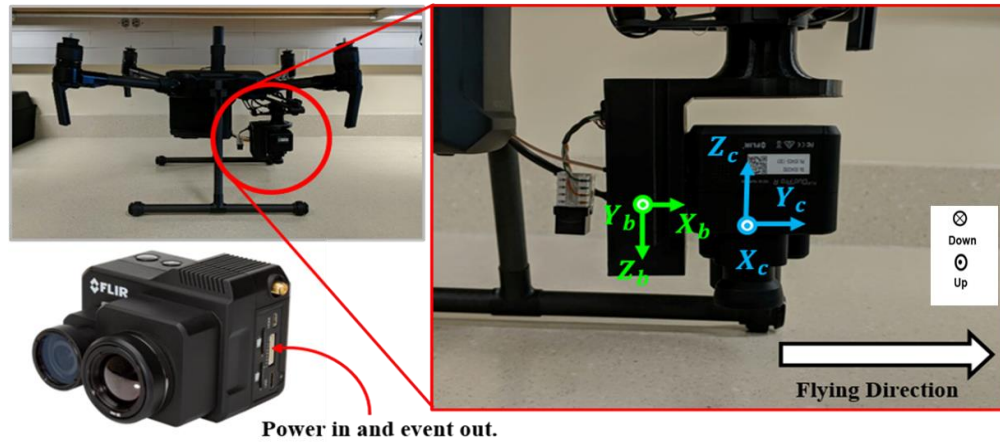


Figure 5.3 System configuration for the DJI M200 equipped with the FLIR RGB frame sensor



Figure 5.4 System configuration for the DJI M600P equipped with the nHS-70 line sensor

Table 5.1 FLIR RGB and Headwall nHS-70 platform's nominal boresight angles and lever arm components

<i>Sensor</i>	$\Delta\omega$ (degree)	$\Delta\phi$ (degree)	$\Delta\kappa$ (degree)	Δx (mm)	Δy (mm)	Δz (mm)
<i>FLIR- RGB</i>	180	0	-90	45	25	50
<i>nHS-70</i>	0	0	180	-20	60	80

Table 5.2 Flight parameters and dataset description for the imaging systems

Date	Sensor	Altitude Above Ground	Ground Speed	GSD	Overlap & Side lap	# of Flight Lines
July 25 th 2018	FLIR Duo Pro R (RGB)	20 m	2.7 m/s	0.7 cm	80%	6
		40 m	5.4 m/s	1.4 cm	80%	6
July 09 th 2019	nHS-70	20 m	3 m/s	1.79	60%	8
		40 m	6 m/s	3.58	60%	10

5.4 Methodology for Automated Feature Extraction and System Calibration

In this section, the proposed strategies for automated image feature extraction and matching for frame and line cameras onboard UAV remote sensing systems are introduced. The matching strategy used in this study to establish conjugate features among overlapping frame camera images, is based on a traditional Structure from Motion (SfM) technique. On the other hand, a new strategy for line cameras, which takes advantages of ortho-rectified images generated for each flight line, is introduced for automated feature matching. Lastly, the bundle block adjustment methodology for system calibration for frame and line camera systems using automatically-derived tie points is presented.

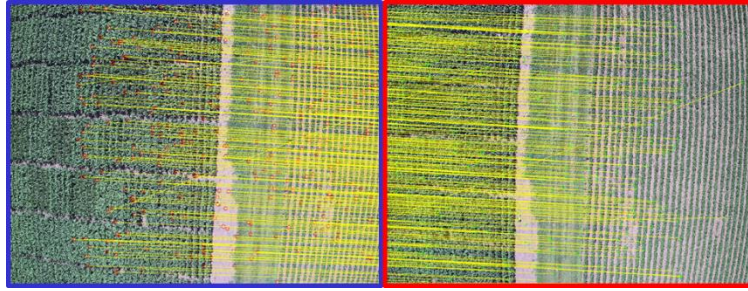
5.4.1 Automated Feature Extraction and Matching for Frame Camera Systems

In this study a graphic processing unit (GPU)-based implementation of the SIFT algorithm, known as SiftGPU [62], is used to efficiently conduct image matching among a large set of frame camera images. Although the SIFT algorithm is designed to be invariant against scaling, in practice this algorithm results in a high percentage of outliers when dealing with images with repetitive patterns or significant scale differences. Repetitive patterns – due to crop nature and mechanized planting – as well as scale difference – due to collecting images from two different flying heights, i.e., 20 m and 40 m – are the two common characteristics of the frame camera dataset used in this study.

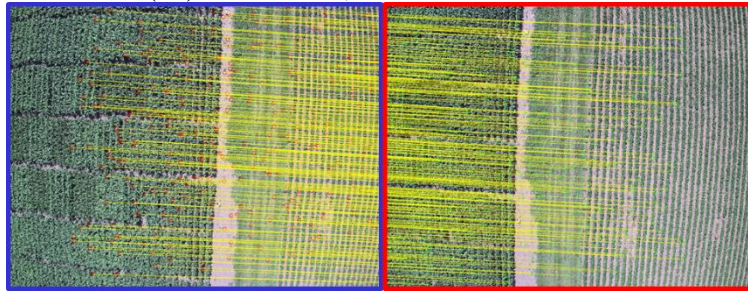
In order to increase the reliability of the established conjugate features when dealing with images with challenging conditions – i.e., repetitive patterns and scale difference – this study uses a Structure from Motion (SfM) framework where the SIFT image matching step is followed by four layers of matching outlier removal. The first layer consists of a forward/backward consistency check for removing obvious matching outliers. Then, relative orientation parameters (ROPs) estimation is conducted while removing potential matching outliers. In the third layer, exterior orientation parameters (EOPs) recovery is carried out wherein more matching outliers are detected and removed. Finally, a bundle adjustment process is conducted for parameters refinement and further matching outlier removal.

More specifically, in the forward/backward consistency check, considering two overlapping images, hereafter denoted as left image and right image, first left-to-right (forward) matching is conducted and an initial set of conjugate features are established. Then, a given pair $(p1, p2)$ is considered to be valid if the same pair is established in the right-to-left (backward) matching. This step helps with initial removal of obvious matching outliers.

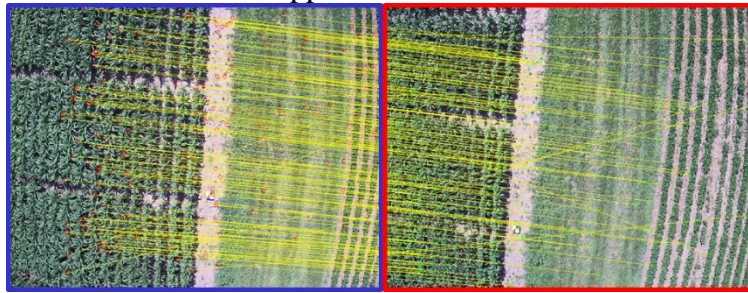
In the next step, the Nister five-point algorithm [63] is augmented with a RANdom SAmple Consensus (RANSAC) [64] framework to simultaneously estimate ROPs and remove potential matching outliers while using epipolar geometry constraints. Figure 5.5 illustrates remaining established matches after forward/backward consistency check, denoted as initial matches, (Figure 5.5a) and after Nister/RANSAC step (Figure 5.5b) for overlapping images in different flying heights. As can be seen in this figure, applying SIFT on images with different scales results in smaller set of initial matches when compared with matching results of overlapping images with same scale. Also, considering Figure 5.5b one can note that when overlapping images are from different flying heights, a higher percentage of outliers are detected and removed through the Nister/RANSAC approach.



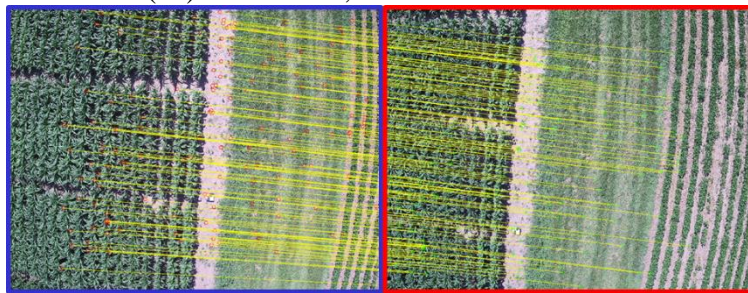
(a1) 40 m/40 m, 3063 initial matches



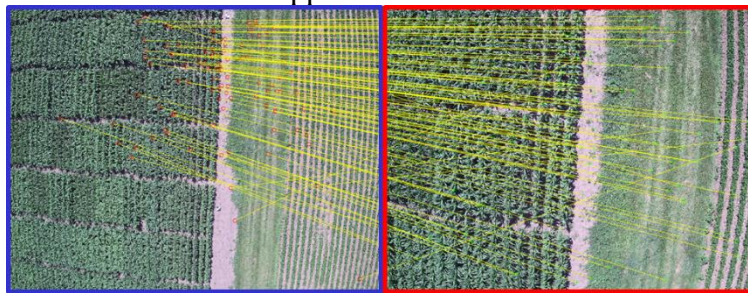
(b1) 40 m/40 m, 2629 (86%) remaining matches after applying Nister/RANSAC approach



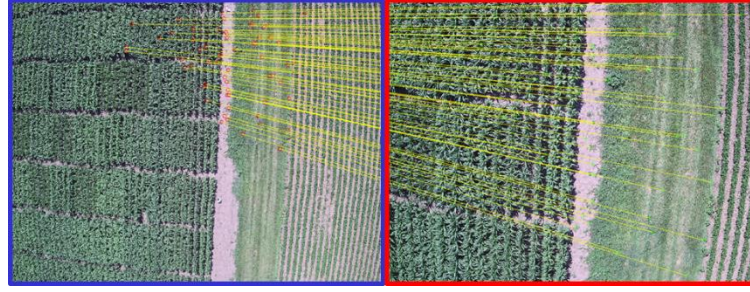
(a2) 20 m/20 m, 1873 initial matches



(b2) 20 m/20 m, 1465 (78%) remaining matches after applying Nister/RANSAC approach



(a3) 40 m/20 m, 973 initial matches



(b3) 40 m/20 m, 612 (63%) remaining matches after applying Nister/RANSAC approach

Figure 5.5 Sample SIFT matching results, (a) initial matches, and (b) remaining matches after Nister/RANSAC step* (*for a better visualization, only 10% of total matched features are plotted)

In order to remove more matching outliers arising from the repetitive patterns and scale differences in the imagery, next step of the proposed SfM technique implements an incremental EOP recovery process based on the work presented by He et al. [32]. This EOP recovery step starts with establishing a local coordinate system by selecting a stereo-pair, and then sequentially augmenting the remaining images into the final image block while considering geometric compatibility among overlapping images. Image augmentation is achieved using the linear rotation averaging and translation averaging techniques introduced by He et al [32]. Another matching outlier removal step is conducted within the translation averaging process where conjugate points that exhibit large back-projection residuals are detected and removed. Interested readers can refer to [32] for more detailed information about the employed incremental EOP recovery strategy.

In the last step of the SfM framework employed in this study, a bundle adjustment process is incorporated within an iterative procedure for detecting and removing more matching outliers. Prior to conducting the bundle adjustment process, first all remaining SIFT features are tracked among all the involved imagery, and their approximate object coordinates are derived using a multi light-ray intersection procedure. Next, using the SIFT features, their corresponding object coordinates, and the camera EOPs, a BA process is conducted to minimize the back-projection residuals for all image tie points. Then, these image points are sorted in descending order according to their residuals and points with residual larger than a predefined threshold t are detected and removed as matching outliers. After removing these outliers, BA will be executed again to refine

image EOPs as well as reconstructed object points. This procedure is repeated until no points with residuals above the threshold t remain.

5.4.2 Automated Feature Extraction and Matching for Line Camera Systems

As mentioned earlier, line cameras operating through push-broom mechanism use a line of detectors arranged perpendicular to the flight direction. As the platform flies, the scene is collected one line at a time (depending on camera frame rate), with simultaneously sampling of all pixels in a line [9]. A scene is formed by successive exposures along the flight trajectory and concatenating the acquired scan lines. Figure 5.6, shows two samples of raw line camera scenes generated from two different flight lines along with a corresponding zoomed-in region on the two scenes. As can be seen in Figure 5.6, raw scenes exhibit a wavy pattern due to the turbulence in UAV's trajectory between successive scan lines. Consequently, corresponding features look different in overlapping raw scenes, impeding the process of automatically established conjugate features for line camera imagery (see Figure 5.6c and 5.6d).

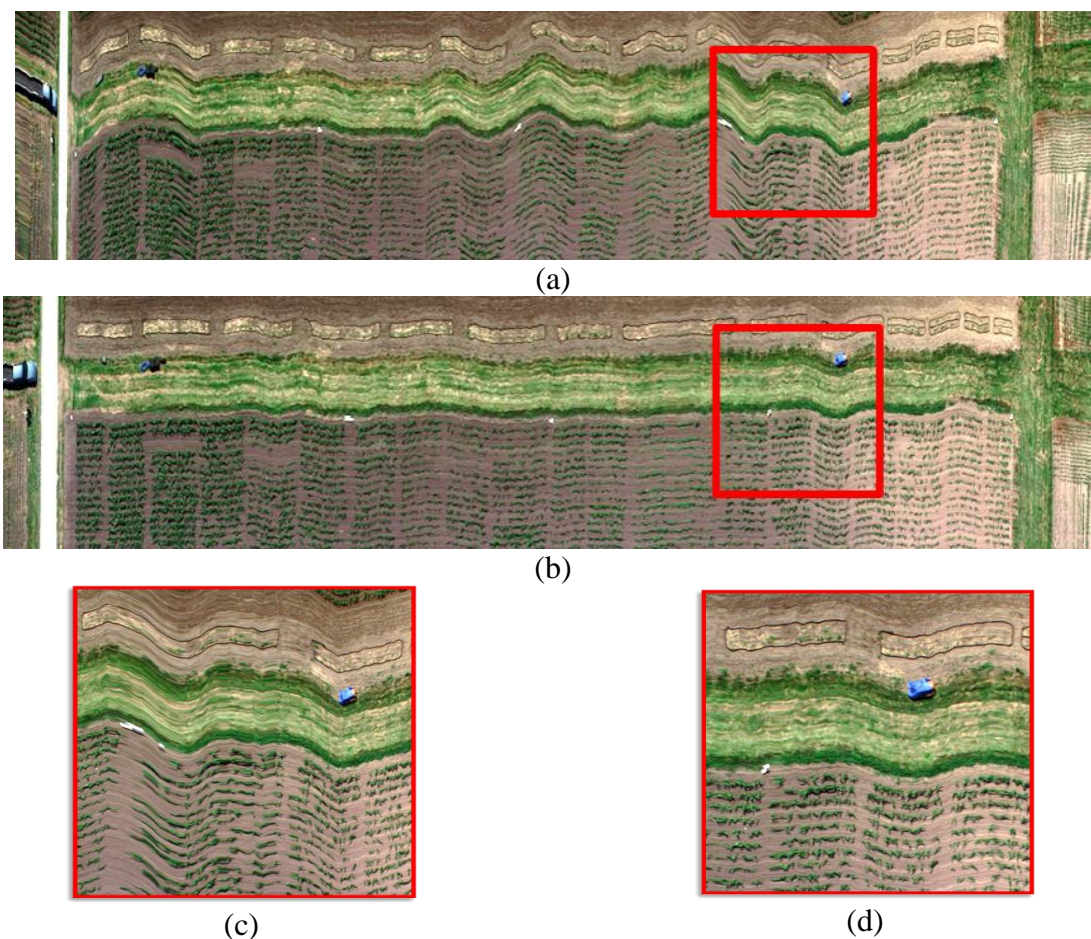


Figure 5.6 Samples of raw scenes for nHS-70 VNIR 20190709 dataset, (a) and (b) raw scenes and (c) and (d) zoomed-in regions.

The proposed strategy for automated generation of tie features among line camera scenes is presented in Figure 5.7. In order to overcome the feature extraction and matching problem on raw scenes with wavy patterns – caused by instability of the trajectory – the proposed framework establishes the feature correspondences on partially ortho-rectified scenes of each flight line. An ortho-rectified scene is obtained by correcting the raw scenes for non-smooth trajectory as well as perspective and camera distortions such that the generated scene is true to scale and corresponds to a map projection throughout the scene. Generation of partially ortho-rectified scenes is shown in the first procedure in Figure 5.7. This step aims at removing the wavy pattern of the raw scenes, so that corresponding features in different flight lines show similar appearance. Also, in this step, a look-up table, which establishes the mapping function between raw and rectified coordinates, is generated. The second procedure deals with applying SIFT matching on all pairs of partially ortho-

rectified scenes. In this step, geo-location information of each partially ortho-rectified scene is used to reduce the search space and consequently the matching ambiguity caused by repetitive patterns in the imagery. Next, similar to what was explained in the previous section, a feature tracking procedure is conducted to track all SIFT matches among all scenes. One should note that coordinates of the established conjugate features have been determined with respect to coordinate systems associated with the ortho-rectified scenes. Hence, in the next step of the proposed strategy the generated look-up table in the first step is used to convert the rectified coordinates to raw coordinates.

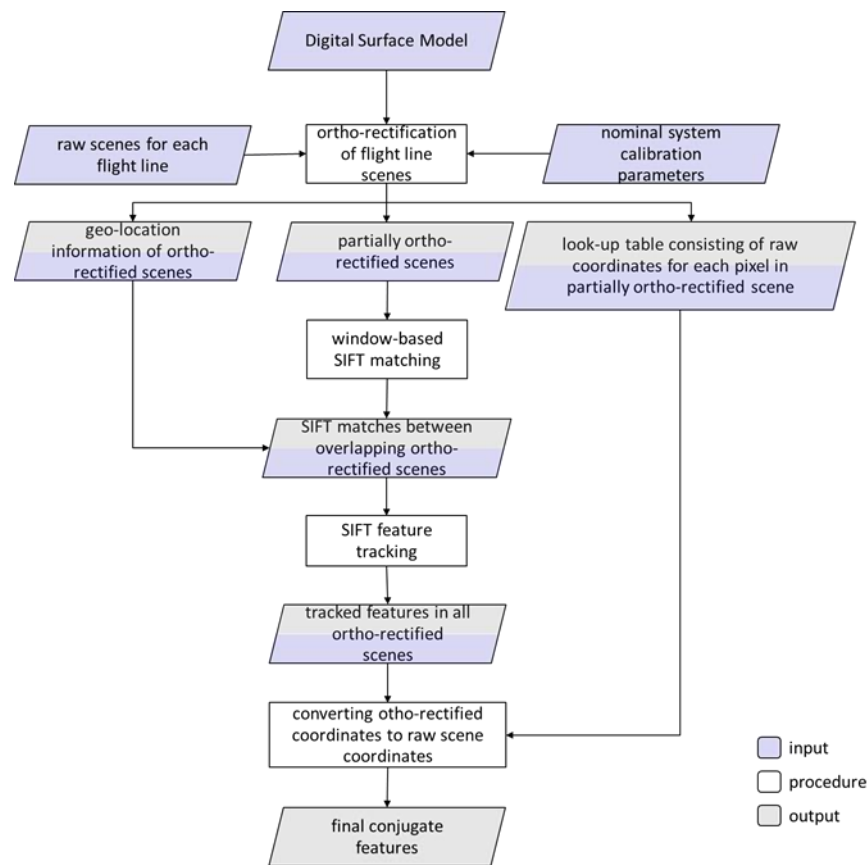


Figure 5.7 Flowchart of the proposed approach for automatically establishment of conjugate features in line cameras

In order to appropriately map intensities observed by the camera to their location in the ortho-rectified scene, an elevation model (DSM) of the scene in question is required. In this study, the DSM is generated using the available LiDAR data of the scene. Then, using GNSS/INS

trajectory information, for each DSM cell, its closest scan line (in 2D) is determined and denoted as initial scan line. In the next step, scan line EOPs and camera IOPs are used to project each DSM cell onto the initial scan line using collinearity equations. One should note that as the scan line is vertically below the perspective center of the utilized camera, for a DSM cell to be visible in a scan line, the projected point has to have the image coordinate component along flight direction – e.g., x coordinate – as close as possible to 0. The correct scan line corresponding to a given DSM cell is derived iteratively, where in each iteration, the projected point coordinate along flight direction is used to determine the scan line for the next iteration. Once the correct scan line is determined, RGB values of the raw scene at the projected point are assigned to the corresponding cell in the ortho-rectified scene. Also, raw scene information – i.e., the derived coordinate across flight direction and the scan line index – for each cell of the ortho-rectified scene is stored in a look-up table and will be used later in the last step of the proposed matching strategy. This ortho-rectification process is depicted in Figure 5.8. Also, Figure 5.9, shows the partially-rectified scenes corresponding to the raw scenes illustrated in Figure 5.6. As shown in Figure 5.9, the wavy pattern of the raw scenes depicted in Figure 5.5, is removed in the ortho-rectified scenes. This can significantly help the image matching algorithm in identifying conjugate points among overlapping scenes of different flight lines.

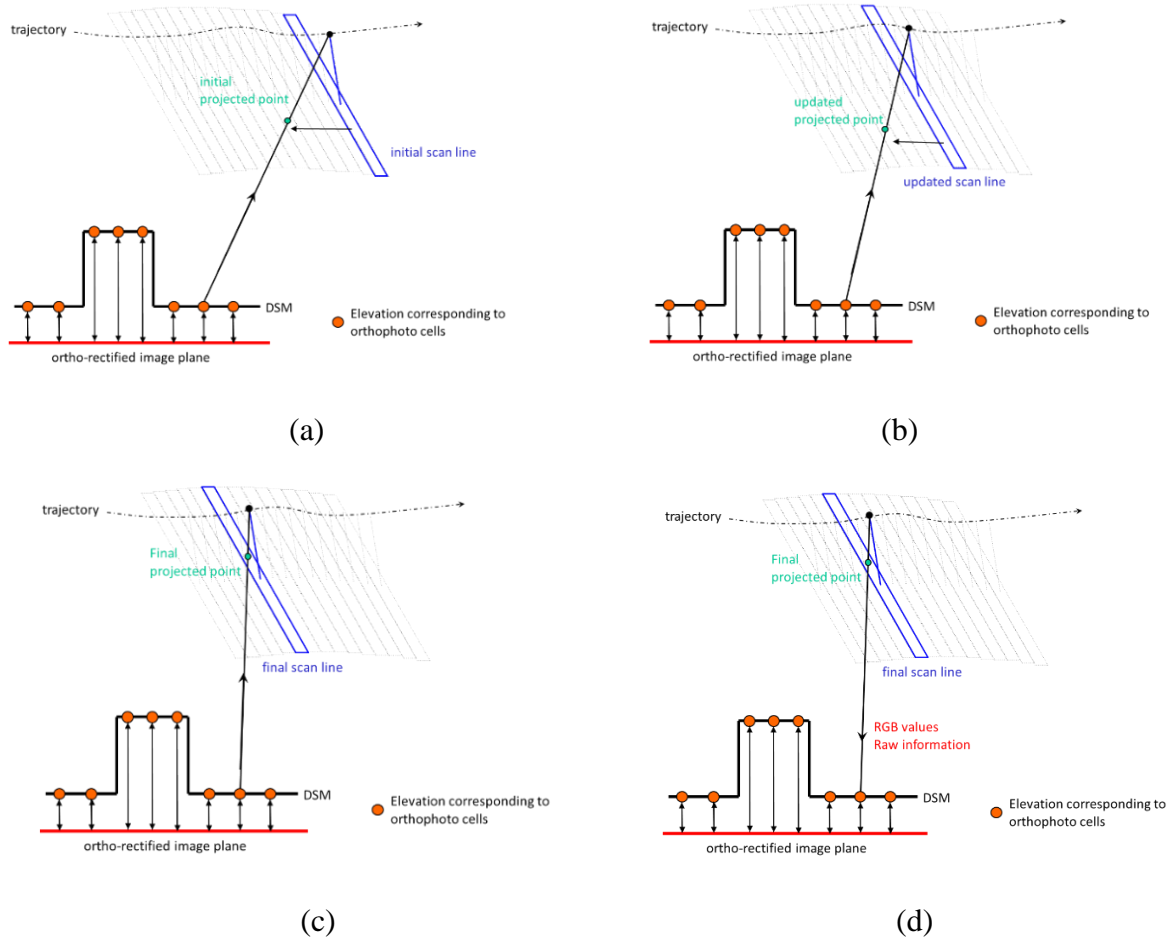
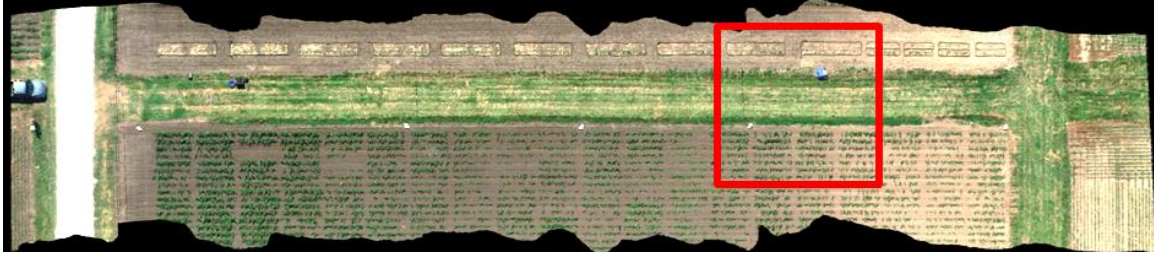
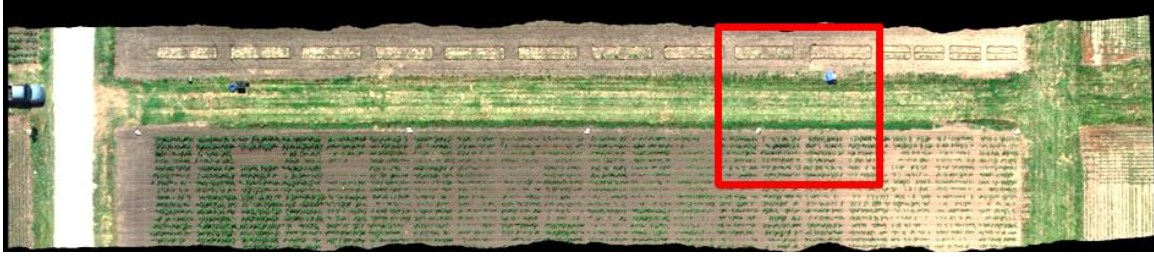


Figure 5.8 Schematic illustration of the iterative ortho-rectification process for line camera scenes, (a) projection of a given DSM cell onto the initial scan line, (b) iterating the projection process using an updated scan line, (c) final projection, and (d) assigning RGB values from the projected point to the ortho-rectified cell.



(a)



(b)



©



(d)

Figure 5.9 Samples of partially ortho-rectified scenes for the nHS-70 VNIR 20190709 dataset, (a) and (b) partially ortho-rectified scenes and (c) and (d) zoomed-in regions.

In the next step of the proposed framework, the SIFT detector and descriptor algorithm is applied on the all partially ortho-rectified scenes. As mentioned earlier, the traditional matching strategy establishes conjugate features between two overlapping images by comparing each feature descriptor in one image with all feature descriptors in the other image. In some applications such as digital agriculture, due to repetitive image patterns, traditional feature matching algorithms often result in insufficient number of matched features and/or matches with high percentage of outliers [45]. To mitigate some of the matching ambiguity problems caused by repetitive patterns, rather than conducting exhaustive search among the feature descriptors, this study exploits the geo-location information of the partially ortho-rectified scenes to reduce the matching search space and consequently the matching ambiguity. More specifically, considering two overlapping ortho-rectified scenes, given a SIFT feature in the first scene, its corresponding planimetric (X and Y)

coordinates in the mapping reference frame are derived, and then used to predict an approximate location of its conjugate feature in the second scene. Next, the predicted point in the second ortho-rectified scene is used to define a search window with a user defined size. The search window size can be determined according to the accuracy of the trajectory information and nominal system calibration parameters. Consequently, among all SIFT features in the second scene, only those which are located inside the search window are considered as candidate conjugate features. Finally, feature matching between the two ortho-rectified scenes is conducted by evaluating the similarity between the feature descriptor in the first scene and its potential conjugate feature descriptors in the second ortho-rectified scene. Figure 5.10 illustrates a sample result of the above-mentioned process for two overlapping partially ortho-rectified scenes.

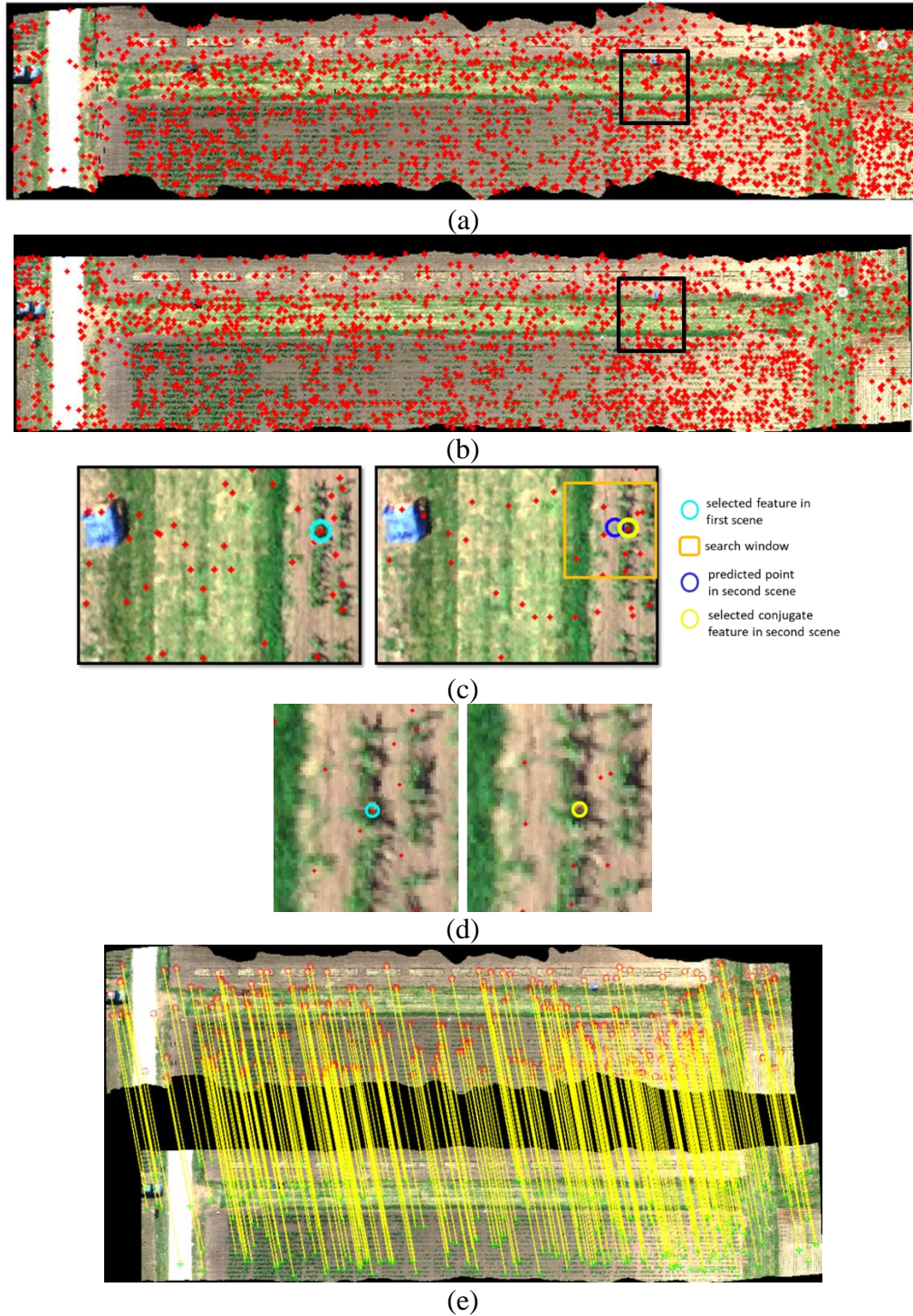
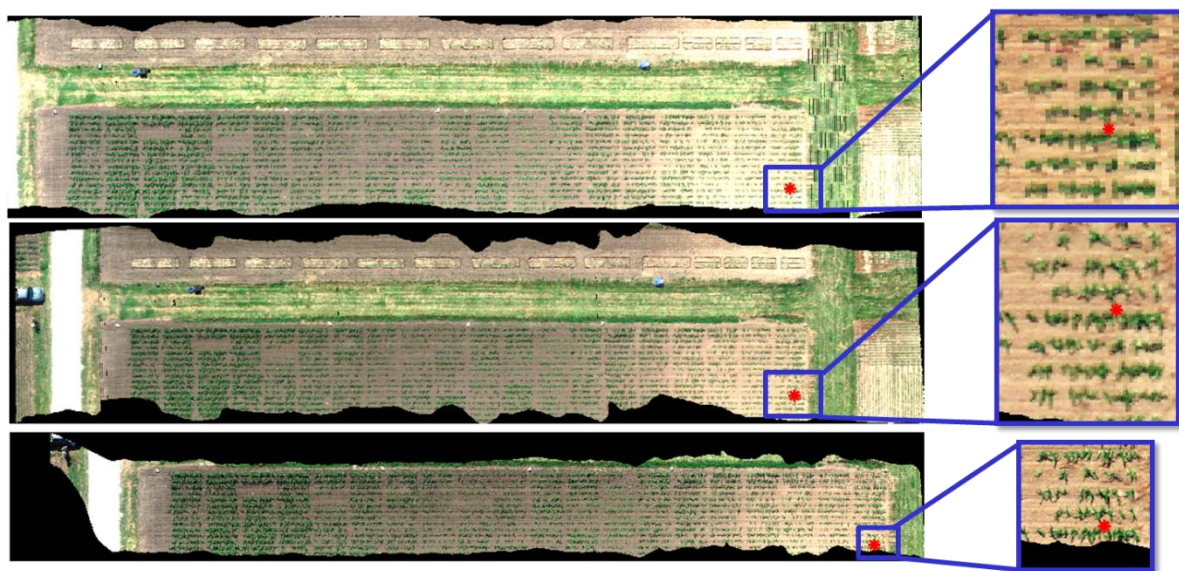
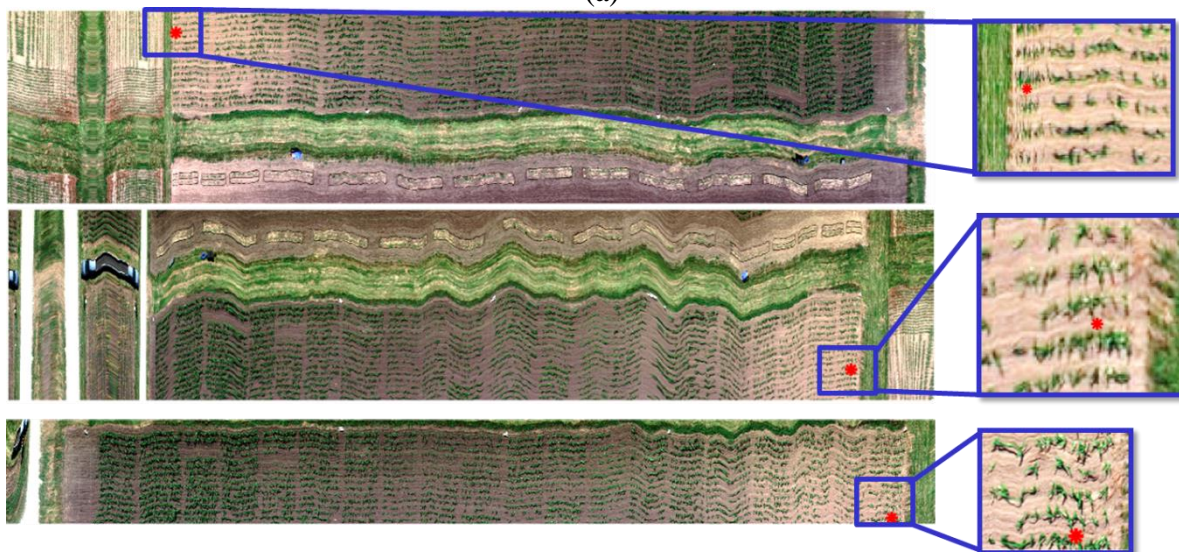


Figure 5.10 Illustration of the proposed feature matching strategy using the nHS-70 VNIR 20190709 dataset, (a) detected SIFT features (red dots) on partially ortho-rectified scene, denoted as first scene, (b) detected SIFT features (red dots) on partially ortho-rectified scene, denoted as second scene, (c) selected feature in first scene (left image) and its corresponding search window and established conjugate feature in second scene (right image), (d) zoomed-in views of the established conjugate features, and (e) final 558 matched features between the two ortho-rectified scenes.

Now that conjugate features are established among all overlapping pairs of ortho-rectified scenes, similar to what was described in the previous section, using a graph-based structure all SIFT matches are tracked among all involved flight lines. In the last step of the proposed matching framework for push-broom cameras, using the look-up table generated in the ortho-rectification stage, for each tracked SIFT feature, its corresponding scanner index and raw scene coordinate across flight direction are derived. Figure 5.11 shows a sample tracked SIFT feature on ortho-rectified scenes as well as corresponding raw scenes.



(a)



(b)

Figure 5.11 A sample tracked SIFT feature, (a) tracked feature (in red) is shown on three different partially-orthorectified scenes, and (b) illustration of the tracked feature on the corresponding raw scenes.

5.4.3 System Calibration for Frame and Line Camera using Automatically-Derived Tie Points

This section presents the bundle adjustment with self-calibration methodology for frame and line camera systems using automatically-derived tie points. LaForest et al. [50] first introduced two approaches for estimating time delay during system calibration for frame camera systems – direct and indirect. The direct approach modifies the mathematical model to incorporate time delay as a system parameter for frame camera systems. The indirect approach uses existing bundle block adjustment software and exploits the correlation among the time delay and lever arm mounting parameter in the flying direction to indirectly solve for time delay. The indirect approach was meant as a special case for those without the capability of modifying bundle adjustment software. This study implements the direct approach for frame and line camera systems to estimate time delay during system calibration.

The mathematical model of the collinearity principle describes the collinearity of the camera perspective center, image point, and corresponding object point. Time delay in a system between the mid-exposure and the recorded event marker by the GNSS/INS unit will affect the position and orientation of the body frame. Therefore, the mathematical model is modified to compensate for changes in position and orientation caused by the time delay [50]. The modified mathematical model is shown in Equation (5.1). The following notations are used throughout this study: a vector connecting point ‘ b ’ to point ‘ a ’ relative to a coordinate system associated with point ‘ b ’ is represented as r_a^b , and a rotation matrix transforming from coordinate system ‘ a ’ to coordinate system ‘ b ’ is represented as R_a^b . LaForest et al. [50] presented the modified mathematical model for the direct approach for frame camera systems. This research focuses on both frame and line camera systems. As mentioned in the introduction, there are important differences in frame and line camera systems. Frame camera’s image coordinates, $r_i^{c(t)}$, will have variable x, y coordinates depending on image point location. However, line camera’s y image coordinates will have variable values but x will always be constant, depending on the camera alignment to the sensor’s focal plane. This causes differences in the image coordinates, $r_i^{c(t)}$, for frame and line camera systems but the overall collinearity equations shown in Equation (5.1) remain unchanged. An illustration of the collinearity equations is presented in Figure 5.12 for frame (a) and line (b) camera systems.

$$r_i^{c(t)} = \frac{1}{\lambda(i,c,t)} R_b^c \left[R_{b(t_0)}^{b(t_0+\Delta t)} R_m^{b(t_0)} (r_l^m - r_{b(t_0)}^m - \dot{r}_{b(t_0)}^m \Delta t) - r_c^b \right] \quad (5.1)$$

Where:

r_l^m : ground coordinates of the object point l

t_0 : initial event marker time

Δt : time delay

$r_i^{c(t)}$: vector connecting perspective center to the image point i captured by the camera at the actual exposure time t , where $t = t_0 + \Delta t$

$\dot{r}_{b(t_0)}^m$: instantons linear velocity at the initial event marker

$r_{b(t_0)}^m$: position of IMU body frame relative to the mapping reference frame at time t_0 derived from the GNSS/INS integration process

$R_m^{b(t_0)}$: rotation matrix from the mapping reference frame to the IMU body frame at time t_0 derived from GNSS/INS integration process

$R_{b(t_0)}^{b(t_0+\Delta t)}$: rotation matrix from the IMU body frame at time t_0 to the IMU body frame at time $t_0 + \Delta t$

r_c^b : lever arm from IMU body frame to camera frame

R_b^c : rotation (boresight) matrix from IMU body frame to camera

$\lambda(i, c, t)$: scale factor for point i captured by camera c at the actual exposure time t

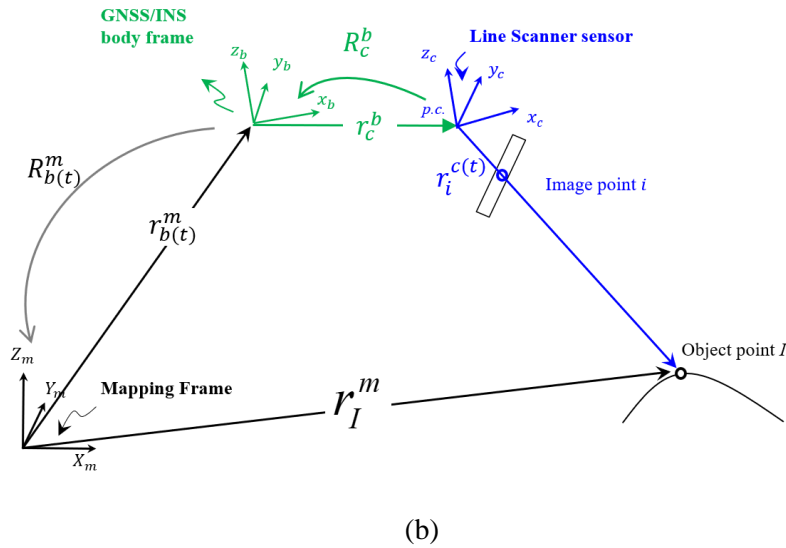
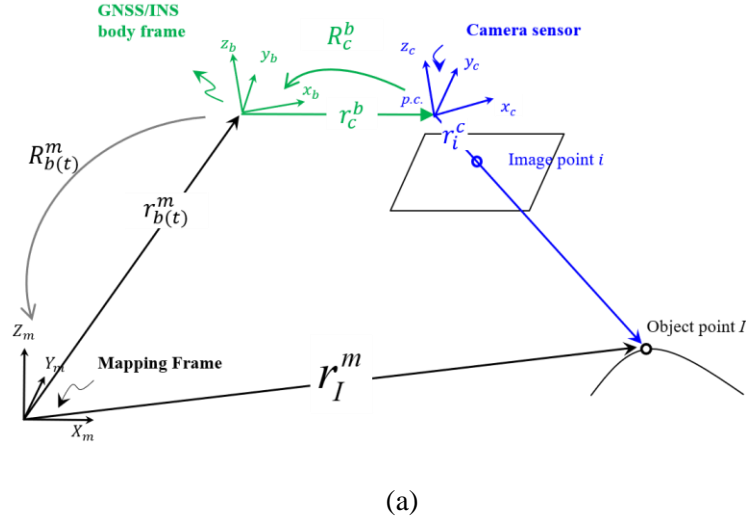


Figure 5.12 Illustration of collinearity equations for (a) frame and (b) line camera.

The bundle block adjustment procedure is used to estimate the unknown parameters in the modified collinearity equations. The target function is to ensure the best intersection of conjugate light rays from images along the same or different flight lines, i.e., ensuring precision. For tie points that correspond to GCPs, the goal is so that the tie points intersect as close as possible to the GCP location, i.e., ensuring accuracy. The bundle adjustment implements a least squares solution to determine the best estimates of unknown parameters. The objective is to estimate the system calibration parameters as accurately as possible with the least amount of ground control points, and preferably without GCPs. In order to estimate the system parameters with the least

amount of control, previous research has been completed on deriving the optimal/minimal flight configuration which considers any small changes in the system parameters that would impact the target function of the bundle adjustment. If for some of the system parameters, changes in the lateral distance between flight lines, flying height, or image point location do not impact the precision, i.e., the light ray intersection of the bundle adjustment, they cannot be estimated in the absence of control. All of the system parameter with the exception of the lever arm Z component will impact the precision of the bundle adjustment [51]. Therefore, in this study, the unknown parameters are the lever arm components in the X and Y directions, boresight angles, time delay, and XYZ ground coordinates of the check and/or tie points. For this study, the observations include the image coordinate measurements of the check and tie points as well as the position and orientation of the GNSS/INS unit event markers. The image coordinate measurements for checkpoints were manually-measured whereas the image coordinate measurements for the tie points were automatically-derived, as explained in the previous section.

Two primary methods of least squares solutions that were considered for this study was the Gauss Markov model and the mixed least squares model, sometimes referred to as Gauss-Helmert or condition equations with parameters [58]. In the Gauss Markov model, any parameter with prior information adds corresponding pseudo observations [65]. In the case of system calibration, this may be parameters such as the GNSS/INS-based position and orientation for scan lines or GCPs. However, it should be noted that in this model, all parameters with prior information are considered as unknowns. This model increases the size of the normal equation matrix dramatically. Therefore, the mixed least squares model is implemented. First, the implemented non-linear function is expressed in Equation (5.2). Here, Y are the observations, X are the unknowns, e are the random errors containing the observations, and P is the weight matrix of observations. The corresponding least squares adjustment model is expressed in Equation (5.3). Here, y is the estimated values of the function evaluated using the approximate values of unknowns and the observations, A is the partial derivative matrix with respect to the unknowns, x are the corrections to the approximate values of unknowns, B is the partial derivatives matrix with respect to the observations, and e is the associated error vector for the observations. The equation for deriving the corrections to the approximate values of the unknowns for each iteration, \hat{x} , is shown in Equation (5.4). The corrections to the approximate unknowns are applied for each iteration until the corrections are sufficiently small for the given convergence criteria. Lastly, the a-posteriori variance factor used

to scale the resulting dispersion matrix is expressed in Equation (5.5). The a-posteriori variance factor, $\hat{\sigma}_o^2$, is used to assess both the bundle adjustment performance and the accuracy of the a-priori weighting of the observations. In the case of mixed observations when the weights are the inverse of the variance/covariance matrix, the a-posteriori variance factor would be expected to be approximately 1. The mixed model does not consider parameters with prior information as unknowns but instead as weighted observations. In the case of system calibration, this allows GNSS/INS-based position and orientation for scan lines and GCPs with prior information to be treated as weighted observations instead of unknowns. This reduces the size of the normal matrix substantially. However, in this case, the bundle adjustment will have a set of mixed observations and weighting the set of mixed observations correctly becomes crucial. For each type of observation, an a-priori weight is assigned based on the uncertainty. For example, for the image measurements a weight, σ_{xy} , is assigned based on the confidence of the image measurement. For the case of manually-measured image coordinates, this weight may be higher (more confidence) than in the case of automatically-derived image coordinates. Other observations, such as GCPs or trajectory information, are also given a weighting based on the uncertainty. The weighting for the GCPs, $\sigma_{XYZ_{GCP}}$, will depend on the GNSS-RTK accuracy and the weighting for the trajectory information, $\sigma_{XYZ_{Traj}}$ and $\sigma_{\omega\phi\kappa_{Traj}}$ will depend on the GNSS/INS unit accuracy. It is essential to correctly assigned realistic weighting for all observations in the model.

$$f(Y - e, X) = 0 \quad e \sim (0, \sigma_o^2 P^{-1}) \quad (5.2)$$

$$y = Ax + Be = Ax + \bar{e} \quad \bar{e} \sim (0, \sigma_o^2 BP^{-1}B^T) \quad (5.3)$$

$$\hat{x} = (A^T (BP^{-1}B^T)^{-1}A)^{-1} (A^T (BP^{-1}B^T)^{-1}y \quad (5.4)$$

$$\hat{\sigma}_o^2 = \frac{\bar{\tilde{e}}^T (BP^{-1}B^T)^{-1}\bar{\tilde{e}}}{n-m} \quad (5.5)$$

where: n is number of equations and m is the of unknowns

Incorporating large numbers of automatically-derived tie points made it essential to include the position and orientation prior GNSS/INS information as weighted observations instead of

unknown values. Implementing the mixed model decreased the normal matrix to only the size of the remaining unknowns which were the system parameters mentioned above and the XYZ ground coordinates of the check/tie points. Furthermore, because of the large number of automatically-derived tie points, the bundle adjustment least squares solution is implemented such that the normal matrix is sequentially built on a per-point basis. This not only increased the speed of the implementation dramatically but is also computationally less expensive. The normal matrix is broken up into sub-blocks to incorporate the sequential building. The first sub-block, $N_{11_{i,j}}$, consists of contributions towards the system parameters from the image coordinates and is of size $m \times m$, where m is the number of unknown system parameters, i is total number of image observations, and j is the total number of images. The second sub-block, $N_{12_{j_i}}$, is the interaction between system parameters and ground coordinates of tie points where j_i is the total number of images where point i is visible. The size of $N_{12_{j_i}}$ is $m \times 3$. The sub-block consisting of ground coordinates of tie points is $N_{22_{j_i}}$ and is of size 3×3 for each object point. These sub-blocks are filled by a sequential summation from each contributing image measurement. The total summation for the normal matrix is shown in Equation (5.6). Incorporating the mixed model as well as sequentially building the normal matrix was essential for implementing the fully-automated spatial and temporal system calibration using a large number of SIFT-based tie points.

$$N = \begin{bmatrix} \sum_{i,j} N_{11_{i,j}} & \sum_{j_i} N_{12_{j_i}} \\ \sum_{j_i} N_{12_{j_i}}^T & \sum_{j_i} N_{22_{j_i}} \end{bmatrix} \quad (5.6)$$

where: i is total number of image observations, j is the total number of images, and j_i is the total number of images where point i is visible

5.5 Experimental Results

In this section, the experimental results for the FLIR RGB frame camera and the nHS-70 hyperspectral line camera are presented. The objective of this section is to compare the system calibration results while using manually-measured checkpoints versus that of using automatically-derived tie points. The results are first evaluated by comparing values of the estimated system parameters. The relative accuracy of the points are also compared by examining the standard deviation of the XYZ ground coordinates produced from the variance-covariance matrix resulting

from the bundle adjustment with self-calibration. Lastly, the absolute accuracy are compared by computing the difference between the derived XYZ ground coordinates of checkpoints to the RTK GNSS measurements. It should be noted that for the checkpoint case, the XYZ ground coordinates are derived by the bundle adjustment with self-calibration and directly compared to the RTK GNSS measurements. Whereas, for the SIFT point case, the estimated system parameters from the bundle adjustment are used in a multi-ray intersection solution to derive the XYZ ground coordinates of the checkpoints and then compared to the RTK GNSS measurements.

5.5.1 DJI M200 integrated with FLIR Duo Pro R – FLIR RGB Frame Sensor

The DJI M200 integrated with the FLIR RGB frame camera sensor results are presented in this section. The checkpoint case had 5 object tie points that correspond to 329 manually-measured image measurements. The SIFT point case had 2,722 object tie points that correspond to 16,095 automatically-derived image measurements. The nominal values, estimated system parameters, and a-posteriori variance factor for the system calibration using checkpoints and using SIFT points are presented in Table 5.3. The a-posteriori variance factor is lower for the SIFT system calibration due to the extremely high redundancy produced by the large number of automatically-derived tie points. The system parameters are very similar in the case of using checkpoints compared to using SIFT points with the only difference seen in the a-posteriori variance factor. The correlation matrix for system parameters for the checkpoint and the SIFT point results are shown in Table 5.4. The correlations highlighted in red are above the chosen ± 0.85 threshold and are flagged as high. The lever arm ΔX and the boresight angle $\Delta\phi$ as well as the lever arm ΔY and boresight angle $\Delta\omega$ have the highest correlations. This is expected based on the bias impact analysis presented in section 4.2.3. The correlation matrix values are relatively the same for the check and SIFT point case. The relative accuracy is also compared. The mean standard deviations of check and SIFT points derived from the bundle adjustment are presented in Table 5.5. There is an increase in the XYZ component standard deviation for the SIFT case. The relative accuracy, i.e., precision, of ground coordinates derived in a bundle adjustment is determined by the number of intersecting light rays and intersection angle. The estimated precision of the X and Y ground coordinates can be determined from the flying height, H and the precision of the image coordinate measurement, σ_{xy} . The estimated precision of the Z ground coordinates can be determined from the flying height, H and

the precision of the image coordinate measurement, σ_{xy} , as well as the magnitude of the baseline between image exposure stations. The larger the magnitude of the base-to-height ratio, the better the intersection geometry will be. The estimated precision of a bundle adjustment based on intersection geometry is illustrated in Figure 5.13. Here, the estimated precision error ellipse is shown for both an example where the base-to-height produces an intersection geometry of 45° and for a base-to-height ratio that produces an intersection geometry of 15° . As shown in the Figure 5.13 illustration, the potential error ellipse associated with a smaller intersection geometry leads to an increase of uncertainty, i.e., degradation in relative accuracy. The intersection geometry for the FLIR RGB check and SIFT object points is calculated for each object point. The check points had a mean intersection geometry of approximately 47° whereas the SIFT points had a mean intersection geometry of approximately 15° . The maximum intersection geometry of the FLIR RGB SIFT object points as well as the mean intersection geometry for the check and SIFT points are shown in Figure 5.14. For the SIFT points, having a significant decrease in geometric intersection compared to the check points geometric intersection is the cause of the increase in mean standard deviation. Absolute accuracy measured through the mean, standard deviation, and RMSE of the differences between checkpoint and surveyed coordinates are reported in Table 5.6. For the checkpoint case, the differences are derived from the ground coordinates derived from the bundle adjustment are compared to the surveyed coordinates. For the SIFT case, the system parameters derived from the bundle adjustment are used in a multi-ray light intersection to derive the ground coordinates of the checkpoints and then compared to the surveyed coordinates. The absolute accuracy from the check and SIFT points case are very similar. However, the XYZ RMSE for the SIFT point case did show a relatively small improvement. Table 5.6 results show that similar absolute accuracy is achieved for the small number of manually-measured check points with ideal geometry and the large number of less precise automatically-derived SIFT points with weaker intersection geometry.

Table 5.3 Estimated system parameters including the standard deviation and a-posteriori variance factor for FLIR RGB system

	Time delay Δt (ms)	Lever arm ΔX (m)	Lever arm ΔY (m)	Boresight $\Delta \omega$ ($^\circ$)	Boresight $\Delta \varphi$ ($^\circ$)	Boresight $\Delta \kappa$ ($^\circ$)	Square root of a- posteriori variance factor (pixel) $\hat{\sigma}_o$
Nominal Values							
FLIR RGB	0	0.045	0.025	180	0	-90	NA
Checkpoints	-205.712 ± 1.291	0.110 ± 0.019	0.015 ± 0.019	178.598 ± 0.035	0.168 ± 0.035	-91.068 ± 0.048	3.591
SIFT Points	-202.007 ± 0.168	0.062 ± 0.001	0.001 ± 0.001	178.542 ± 0.003	0.088 ± 0.003	-90.962 ± 0.009	1.210

Table 5.4 Correlation matrix for system parameters of the checkpoint and the SIFT point results for FLIR RGB system

	ΔX		ΔY		$\Delta \omega$		$\Delta \varphi$		$\Delta \kappa$		Δt	
	Check k	SIFT	Check	SIFT	Check	SIFT	Check	SIFT	Check	SIFT		
ΔX	1	1										
ΔY	0.011	0.033	1	1								
$\Delta \omega$	0.908	0.893	0.014	0.026	1	1						
$\Delta \varphi$	0.008	-0.019	-0.942	-0.930	0.002	-0.012	1	1				
$\Delta \kappa$	0.002	0.006	0.004	0.129	-0.003	-0.02	-0.021	-0.28	1	1		
Δt	-0.005	-0.075	-0.038	-0.041	0.254	0.234	0.028	0.022	0.068	.080	1	1

Table 5.5 Mean standard deviation of check/SIFT points derived from the bundle adjustment for the FLIR RGB system

Mean Standard Deviations			
	X (m)	Y (m)	Z (m)
Checkpoints Only	0.015	0.015	0.061
SIFT Points Only	0.106	0.119	0.431

Table 5.6 Statistics of the differences between the RTK/GNSS measurements of the checkpoints and those derived either by the bundle adjustment when using only check points or by multi-light ray intersection using the derived system parameters from the SIFT-based bundle adjustment for the FLIR RGB system

	Mean $X/Y/Z$ (m)			STD $X/Y/Z$ (m)			RMSE $X/Y/Z$ (m)		
Checkpoints	-0.003	0.033	0.115	0.016	0.01	0.086	0.014	0.034	0.139
SIFT Points	-0.003	0.025	0.116	0.007	0.010	0.045	0.007	0.027	0.123

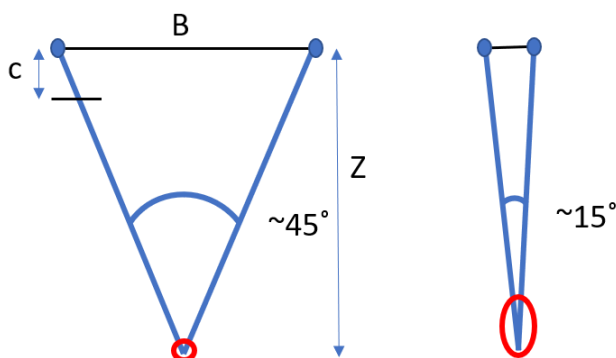


Figure 5.13 Illustration of estimated precision of a bundle adjustment based on intersection geometry

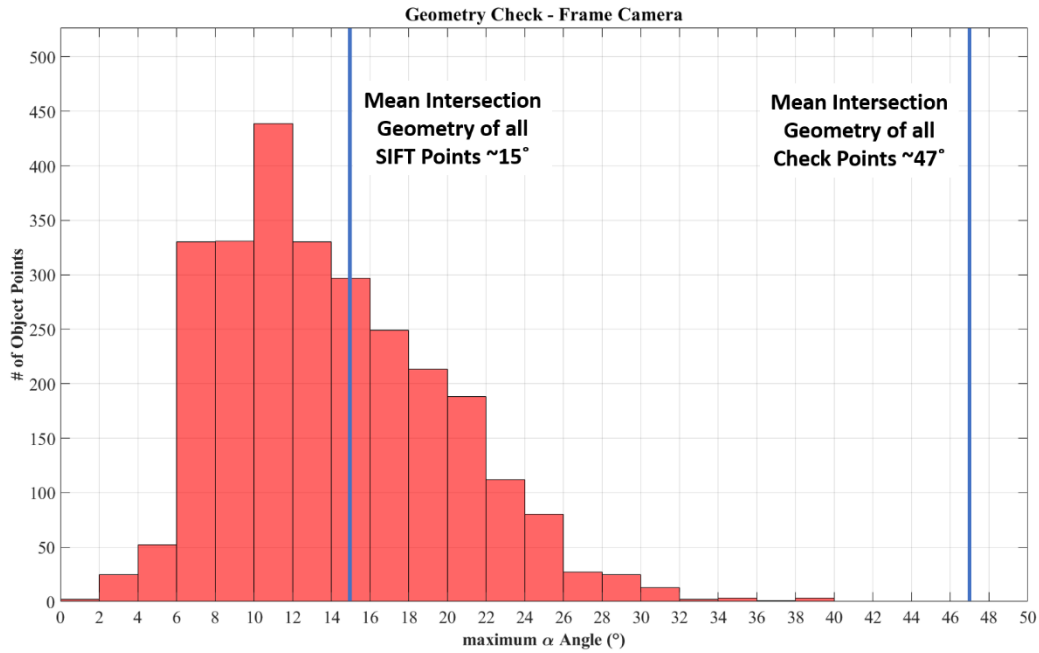


Figure 5.14 Mean intersection geometry for the check points and mean and maximum intersection geometry of the FLIR RGB SIFT object points

5.5.2 DJI M600 integrated with nHS-70 Hyperspectral Line Camera Sensor

The DJI M600 integrated with the nHS-70 hyperspectral line camera sensor results are presented in this section. The checkpoint case had 5 object tie points that correspond to 64 manually-measured image measurements. The SIFT point case had had 3,889 object tie points that correspond to a total of 15,165 automatically-derived image measurements. The nominal values, estimated system parameters, and a-posteriori variance factor for the nHS-70 system calibration using checkpoints and using SIFT points are presented in Table 5.7. The system parameters are very similar in the case of using checkpoints only compared to using SIFT points. The time delay was estimated to be 5.9 and 7.3 ms for the checkpoint and SIFT point case, respectively. This is considered a relatively minimal time delay compared to the approximately -205 ms significant time delay found in the frame FLIR RGB sensor. The a-posteriori variance factor is lower for the SIFT system calibration due to the extremely high redundancy of using automatically-derived tie points over the smaller number of manually-measured checkpoints. The correlation matrix of system parameters for the checkpoint and the SIFT point results are shown in Table 5.8. The correlations highlighted in red are above a chosen ± 0.85 threshold and are flagged as high. The

lever arm ΔX and the boresight angle $\Delta\phi$ as well as the lever arm ΔY and boresight angle $\Delta\omega$ have the highest correlations. Again, this is expected based on the bias impact analysis presented in section 4.2.3. The correlation matrix values are relatively the same for checkpoints and SIFT points. The relative accuracy is also compared. The mean standard deviations of check and SIFT points derived from the bundle adjustment are presented in Table 5.9. Although, the X and Y components comparison between the check and SIFT tie points are on a similar magnitude there is an increase in the Z component standard deviation for the SIFT case. This again is due to the geometry of the SIFT tie points compared to the checkpoints. Similarly to the frame FLIR RGB sensor the check points had a much better mean intersection geometry than the SIFT points. The mean intersection geometry of the check points was approximately 99° whereas the SIFT points had a mean intersection geometry of 15° . Having such a significant decrease in geometric intersection compared to the check points geometric intersection is the cause of the increase in mean standard deviation. Lastly, the absolute accuracy is presented. Absolute accuracy measured through the mean, standard deviation, and RMSE of the differences between checkpoint and surveyed coordinates are reported in Table 5.10. The absolute accuracy from the check and SIFT points case are very similar. The RMSE values show a minimal difference of 0.05 cm or less for the check and SIFT points.

Table 5.7 Estimated system parameters including the standard deviation and a-posteriori variance factor for nHS-70 line camera system

	Time delay Δt (ms)	Lever arm ΔX (m)	Lever arm ΔY (m)	Estimated boresight $\Delta\omega$ ($^\circ$)	Boresight $\Delta\phi$ ($^\circ$)	Boresight $\Delta\kappa$ ($^\circ$)	Square root of a- posteriori variance factor (pixel) $\hat{\sigma}_o$
Nominal Values							
nHS-70	0	-0.02	0.06	0	0	180	NA
Checkpoints	5.901 ± 0.292	0.030 ± 0.006	0.065 ± 0.006	0.210 ± 0.011	-0.094 ± 0.013	179.967 ± 0.021	0.473
SIFT Points	7.2637 ± 0.049	0.013 ± 0.001	0.055 ± 0.001	0.181 ± 0.002	-0.084 ± 0.002	-179.947 ± 0.005	0.208

Table 5.8 Correlation matrix of system parameters for the checkpoint and the SIFT point results for nHs-70

	ΔX		ΔY		$\Delta \omega$		$\Delta \varphi$		$\Delta \kappa$		Δt	
	Check	SIFT	Check	SIFT	Check	SIFT	Check	SIFT	Check	SIFT	Check	SIFT
ΔX	1	1										
ΔY	-0.011	0.014	1	1								
$\Delta \omega$	-0.007	0.017	0.946	0.943	1	1						
$\Delta \varphi$	-0.900	-0.896	0.022	-0.023	0.012	-0.038	1	1				
$\Delta \kappa$	-0.017	-0.062	-0.010	-0.023	-0.014	0.013	0.024	0.107	1	1		
Δt	0.222	0.114	-0.041	0.013	-0.024	0.032	-0.515	-0.376	-0.003	0.002	1	1

Table 5.9 Mean standard deviations of check/SIFT points derived from the bundle adjustment for the nHS-70 system

Mean Standard Deviations			
	X (m)	Y (m)	Z (m)
Checkpoints Only	0.005	0.005	0.026
SIFT Points Only	0.033	0.025	0.219

Table 5.10 Statistics of the differences between the RTK/GNSS measurements of the checkpoints and those derived either by the bundle adjustment when using only check points or by multi-light ray intersection using the derived system parameters from the SIFT-based bundle adjustment for the nHS-70 system

	Mean $X/Y/Z$ (m)			STD $X/Y/Z$ (m)			RMSE $X/Y/Z$ (m)		
Checkpoints	-0.019	0.008	-0.004	0.006	0.008	0.026	0.020	0.011	0.024
SIFT Points	-0.018	0.011	-0.014	0.006	0.008	0.028	0.019	0.013	0.029

5.6 Conclusions and Recommendations for Future Work

Unmanned aerial vehicles (UAVs) equipped with global navigation satellite systems/inertial navigation systems (GNSS/INS) and imaging systems provide accurate 3D reconstruction for a variety of applications. Geometric system calibration – which consists of spatial and temporal calibration – is crucial for producing accurate 3D data from UAV imaging systems. This research presented a methodology for reliable automated feature extraction and matching for both frame and line camera systems. The automatically-derived tie points were then used in a bundle adjustment with self-calibration – capable of estimating spatial and temporal system parameters – to produce highly accurate system calibration parameters. The results showed that the matching approach paired with the automated system calibration presented in this research was capable of producing the same level of absolute accuracy compared to using manually-measured tie points for both frame and line camera systems. However, relative accuracy was worse for the automatically-derived tie points. This was found to be due to the intersection geometry of the generated SIFT points. Additionally, the results showed that the automated system calibration approach presented in this paper can be applied to systems with significant and minimal time delay discrepancies and still achieve reliable estimates of system parameters and absolute accuracy. In conclusion, this paper presented an automated spatial and temporal calibration approach that produce highly accurate system calibration parameters without the need for GCPs or manually-measured tie points for both frame and line camera systems. Future work will focus on simultaneously integrating frame and line camera sensors in the bundle adjustment and matching procedure. Also, other algorithms such as speeded up robust features (SURF) will be explored as matching alternatives. Future work will also include testing a larger variety of sensors and datasets.

6. CONCLUSIONS AND RECOMMENDATIONS FOR FUTURE WORK

6.1 Research Conclusions

This research focused on spatial and temporal system calibration for frame and line camera systems equipped with GNSS/INS units onboard UAVs. This research specifically studied calibration strategies capable of estimating time delay between timestamps of GNSS/INS event markers and the image mid-exposure timestamps while simultaneously estimating system mounting parameters.

For frame camera systems, two one-step algorithms – direct and indirect – were presented. Contrary to previous research, the direct approach evaluated the linear and angular velocities directly and did not rely on raw data from the GNSS/INS. Also, the direct approach did not assume that the platform rotation to be constant during the time delay period. An optimal flight configuration was then derived so that one can estimate the system parameters, including the lever arm components, boresight angles, and time delay simultaneously. The optimal flight configuration presented maximizes the impact of biases or any possible errors in the system parameters while also decoupling those parameters. Using the bias impact analysis, the indirect approach was introduced as an alternative for those without the capability of modifying bundle adjustment software. The indirect approach exploits the correlation between the time delay in the system and the lever arm component in the flying direction to estimate time delay. The approaches were tested on systems with sensors that were modified to both incorporate the flash hot-shoe time synchronization – which significantly reduces the time delay – and also a sensor that only makes use of the manufactured internal “frame sync” option, which had more significant time delay. Furthermore, the approaches presented were tested and evaluated in an integrated sensor orientation (ISO) and direct geo-referencing adjustments, without the need for GCPs. The results showed that the direct and indirect approaches were capable of handling and correcting time delay in frame camera systems. Furthermore, horizontal accuracy of 1–3 times the GSD were achieved without the use of any GCPs or adjusting the original GNSS/INS trajectory information.

Spatial and temporal calibration was then investigated for UAV line camera systems, which was not covered in previous research. The direct approach was used for geometric system calibration including time delay estimation. First, the modified mathematical model for line

camera systems was presented in the methodology section. Then, the direct approach was introduced for line camera systems. This research rigorously derived the optimal flight configuration for system calibration while estimating time delay for line camera systems and compared it to that for frame camera systems. The optimal flight configuration and bias impact analysis for line camera systems differed from frame cameras due to the difference in imaging geometry (i.e., frame cameras capture 2D images at one time whereas line cameras capture a 1D image). Therefore, the ability to decouple system parameters will be limited for line cameras compared to frame cameras. The bias impact analysis for line camera systems showed that the indirect approach is not a feasible solution for push-broom line cameras onboard UAVs due to the limited ability of line cameras to decouple system parameters and was confirmed with experimental results. The direct results showed that when a time delay exists and spatial and temporal calibration was performed, vertical and horizontal accuracy are approximately that of the GSD of the sensor. Furthermore, when a large artificial time delay was introduced for line camera systems, the direct approach still achieved accuracy less than the GSD of the system and performs 2.5-8 times better in the horizontal components and up to 18 times better in the vertical component than not performing the temporal calibration.

Lastly, this research demonstrated fully-automated spatial and temporal calibration for frame and line camera systems. In past research, spatial and temporal calibration has been conducted with and without the need for GCPs and with and without automatically-derived tie points for frame camera. However, research has yet to focus on automated spatial and temporal calibration without the need for GCPs for both frame and line camera systems. This research presented a methodology for reliable automated feature extraction and matching for both frame and line camera systems. First, the automated feature extraction and matching for frame cameras was presented and implements a SfM technique. Then, a new automated feature extraction and matching strategy for line camera systems was presented which applies SIFT algorithm on partially ortho-rectified scenes instead of raw scenes. Lastly, the mathematical model used for spatial and temporal calibration, as well as the implemented bundle adjustment to incorporate a large number of tie points, was presented. The results showed that the automated system calibration and matching approach presented in this research was capable of producing the same level of absolute accuracy compared to using manually-measured tie points for both frame and line camera systems. However, relative accuracy was worse for the automatically-derived tie points. This was found to

be due to the intersection geometry of the generated SIFT points. Furthermore, the results showed that the automated system calibration approach presented in this research can be applied to systems with significant and minimal time delay discrepancies and still achieve reliable estimates of system parameters and absolute accuracy.

In summary, below is the list of contributions this dissertation presented:

1. Frame Cameras – New strategies for time delay estimation during system calibration for UAV-based, GNSS/INS-assisted imaging systems were developed
 - A modified mathematical model that included time delay as an unknown system parameter during the bundle block adjustment procedure for frame camera systems was developed and incorporated
 - The optimal flight configuration was established for frame camera systems such that system parameters can be simultaneously estimated as accurately as possible without the use of GCPs
 - An alternative approach was established for users without capability of updating software to accurately estimating time delay for system calibration in frame camera systems
2. Line Cameras – Spatial and temporal calibration for UAV-based, GNSS/INS-assisted line camera imaging systems was developed
 - A modified mathematical model that included time delay as an unknown system parameter during the bundle block adjustment procedure for line camera systems developed and incorporated
 - The optimal flight configuration for line camera systems was established to accurately estimate spatial and temporal system parameters
 - The bias impact analysis for line camera systems showed that the indirect approach is not a feasible solution for line cameras onboard UAVs due to the limited ability of line cameras to decouple system parameters

3. Developed a fully-automated bundle adjustment with self-calibration capable of estimating spatial and temporal system parameters for frame and line camera systems
 - Automatically-derived tie point features from both frame and line camera systems
 - Modified the bundle adjustment system calibration to successfully incorporate a large amount of automatically-derived tie points for frame and line camera systems

6.2 Recommendations for Future Work

Recommendations for future work relating to spatial and temporal calibration and the specific research completed here are as follows:

- Focus on implementing a combined bundle adjustment with self-calibration for frame and line camera systems that apply the modified mathematical model to incorporate time delay as an optional system parameter. Combining frame and line cameras in a bundle adjustment exploit the geometric and radiometric benefits of both imaging systems and could therefore lead to more accurate system calibration.
- Apply the modified mathematical model to commercial-grade satellite frame and line camera systems (i.e. small satellites). Contrary to more robust spaceborne satellites, the commercial-grade small satellites may need even more system calibration, including time delay estimation, after launch.
- Perform stability analysis on the time delay system parameter over the course of time and storage changes. A time delay stability analysis for UAV systems would be particularly important since lightweight UAVs system parameters may not be as stable after transport or storage.
- Investigate further blunder detection techniques for the automatically-derived tie points. When time delay exists in the system, and is unknown, blunder detection conducted prior to the system calibration may not be effective at removing all necessary blunders. An additional blunder detection, potentially within the system calibration bundle adjustment, could improve calibration results from automatically-derived tie points.

- Focus on generating automatically-derived tie points with intersection geometry similar to that of manually-measured check/tie points. The system calibration results may then improve even further when using a large number of tie points with ideal intersection geometry.
- Investigate incorporating ‘folding’ the normal equations into the bundle adjustment software – invert sub-blocks of normal matrix. Inverting sub-blocks of the normal matrix would further improve the implementation of a bundle adjustment with self-calibration using a large amount of automatically-derived tie points.

APPENDIX

This Appendix is meant to further expand details of the derived equations in section 3.3.3 Optimal Flight Configuration for System Calibration while Considering Time Delay. More specifically, this Appendix is meant to address details leading to the derivation of Equation 3.17b.

The goal is to derive the partial derivatives of the collinearity equations with respect to the system parameters to evaluate their impact on the change in ground coordinates, ΔX , ΔY , and ΔZ . Equation 3.17b is the partial derivatives of the modified collinearity equations with respect to the boresight angles, $\Delta\omega$, $\Delta\phi$, $\Delta\kappa$. The first step in deriving these partial derivatives is examining the collinearity equations in Equation 3.11 for terms comprised of the boresight angles. The term $\lambda(i, c, t)R_{b(t_0)}^m R_{b(t_0+\Delta t)}^{b(t_0)} R_c^b r_i^{c(t)}$ is comprised of boresight angles and is needed to derive the partial derivatives. An evaluation of the change in the scale as a result of the angular sensor tilt which can be caused either by changes in boresight angles or time delay must be addressed. An illustration of the change in scale as a result of an angular sensor tilt is displayed in Figure A.1. Here, P denotes the perspective center of the imaging system, H is the flying height, c is principal distance, i is the image point, and I and I' are the corresponding object points, depending on angular sensor tilt. The scale can be defined as $\lambda = \frac{PI}{Pi}$ and $\frac{PI'}{Pi}$ and with an angular sensor tilt $\frac{PI}{Pi} \neq \frac{PI'}{Pi}$. The change in scale is represented by $\Delta\lambda$. Assuming a vertical sensor and incorporating the change in scale, the term comprised of boresight angles needed for partial derivatives can be expressed in Equation (A.1). Now, assuming that variations in the angular parameters would not change the elevation and after ignoring second order terms, then the change in ground coordinate ΔZ will be zero and can be expressed as Equation (A.2). Reordering Equation (A.2), an expression for the change in scale, $\Delta\lambda$, can be shown in Equation (A.3). Lastly, Equation (A.3) can be substituted back into Equation (A.1) and is expressed in Equation (A.4) which is then used to derive Equation 3.17b.

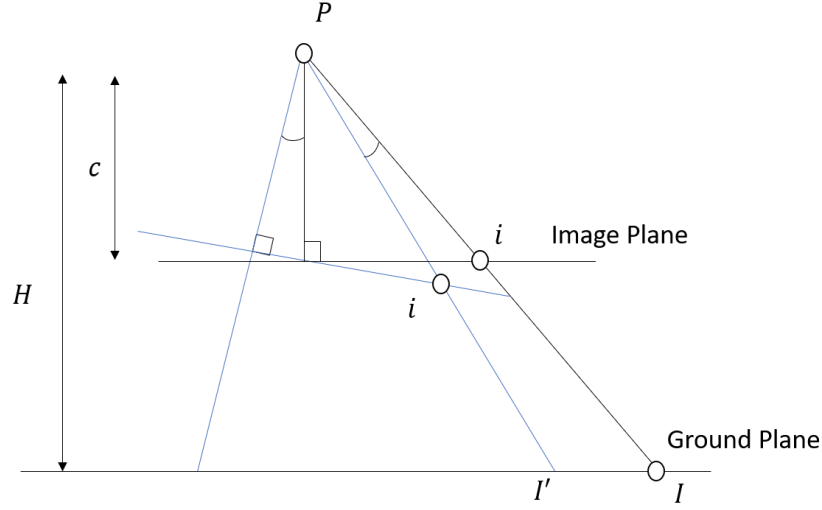


Figure A.1 Illustration of the change in the scale as a result of angular sensor tilt

$$\begin{aligned}
 & (\lambda + \Delta\lambda) R_{b(t_0)}^m R_{b(t_0+\Delta t)}^{b(t_0)} R_c^b r_i^{c(t)} = \\
 & (\lambda + \Delta\lambda) \begin{bmatrix} \pm 1 & \mp(\Delta\kappa + \Delta t\dot{\kappa}_b(t_0)) & \pm(\Delta\varphi + \Delta t\dot{\varphi}_b(t_0)) \\ \pm(\Delta\kappa + \Delta t\dot{\kappa}_b(t_0)) & \pm 1 & \mp(\Delta\omega + \Delta t\dot{\omega}_b(t_0)) \\ -(\Delta\varphi + \Delta t\dot{\varphi}_b(t_0)) & (\Delta\omega + \Delta t\dot{\omega}_b(t_0)) & 1 \end{bmatrix} \begin{bmatrix} x_i \\ y_i \\ -c \end{bmatrix} \quad (\text{A.1})
 \end{aligned}$$

* dropping the indices on scale during this derivation for simplification: $\lambda(i, c, t) = \lambda$

$$\Delta Z = \lambda[(\Delta\omega + \Delta t\dot{\omega}_b(t_0))y_i - (\Delta\varphi + \Delta t\dot{\varphi}_b(t_0))x_i] - \Delta\lambda c = 0 \quad (\text{A.2})$$

$$\Delta\lambda = \frac{\lambda}{c}[(\Delta\omega + \Delta t\dot{\omega}_b(t_0))y_i - (\Delta\varphi + \Delta t\dot{\varphi}_b(t_0))x_i] \quad (\text{A.3})$$

$$\begin{aligned}
 & \left(\lambda + \frac{\lambda}{c}[(\Delta\omega + \Delta t\dot{\omega}_b(t_0))y_i - (\Delta\varphi + \Delta t\dot{\varphi}_b(t_0))x_i] \right) \\
 & \begin{bmatrix} \pm 1 & \mp(\Delta\kappa + \Delta t\dot{\kappa}_b(t_0)) & \pm(\Delta\varphi + \Delta t\dot{\varphi}_b(t_0)) \\ \pm(\Delta\kappa + \Delta t\dot{\kappa}_b(t_0)) & \pm 1 & \mp(\Delta\omega + \Delta t\dot{\omega}_b(t_0)) \\ -(\Delta\varphi + \Delta t\dot{\varphi}_b(t_0)) & (\Delta\omega + \Delta t\dot{\omega}_b(t_0)) & 1 \end{bmatrix} \begin{bmatrix} x_i \\ y_i \\ -c \end{bmatrix} \quad (\text{A.4})
 \end{aligned}$$

REFERENCES

1. Mikhail, E. M., Bethel, J. S., & McGlone, J. C. (2001). *Introduction to modern photogrammetry*. New York, NY: Wiley.
2. Furukawa, Y., & Ponce, J. (2009). Accurate camera calibration from multi-view stereo and bundle adjustment. *International Journal of Computer Vision*, 84(3), 257-268.
3. Zhou, G., Tang, X., & Yuan, B. (1996). Distortion model selecting and accuracy evaluation for CCD camera calibration. In *Proceedings of Third International Conference on Signal Processing (ICSP'96)* (Vol. 2, pp. 875-878). IEEE.
4. Rathnayaka, P., Baek, S. H., & Park, S. Y. (2017, February). Calibration of a Different Field-of-view Stereo Camera System using an Embedded Checkerboard Pattern. In *International Conference on Computer Vision Theory and Applications* (Vol. 5, pp. 294-300).
5. Habib, A. F., Morgan, M., & Lee, Y.R. (2002). Bundle adjustment with self-calibration using straight lines. *The Photogrammetric Record*, 17(100), 635-650.
6. Habib, A.F., Bang, K. I., Shin, S. W., & Mitishita, E. (2007). LiDAR system self-calibration using planar patches from photogrammetric data. In *The 5th International Symposium on Mobile Mapping Technology*, [CD-ROM] (pp. 28-31).
7. Ravi, R., Lin, Y., Elbahnasawy, M., Shamseldin, T., & Habib, A. (2018). Simultaneous System Calibration of a Multi-LiDAR Multicamera Mobile Mapping Platform. *IEEE Journal of Selected Topics in Applied Earth Observations and Remote Sensing*, 11(5), 1694-1714.
8. Li, Z., Tan, J., & Liu, H. (2019). Rigorous boresight self-calibration of mobile and UAV LiDAR scanning systems by strip adjustment. *Remote Sensing*, 11(4), 442.
9. Habib, A., Zhou, T., Masjedi, A., Zhang, Z., Flatt, J. E., & Crawford, M. (2018). Boresight calibration of GNSS/INS-assisted push-broom hyperspectral scanners on UAV platforms. *IEEE Journal of Selected Topics in Applied Earth Observations and Remote Sensing*, 11(5), 1734-1749.
10. Rehak, M., & Skaloud, J. (2017). Time synchronization of consumer cameras on Micro Aerial Vehicles. *ISPRS Journal of Photogrammetry and Remote Sensing*, 123, 114-123.
11. Elbahnasawy, M. (2018). *GNSS/INS-assisted Multi-camera Mobile Mapping: System Architecture, Modeling, Calibration, and Enhanced Navigation* (Doctoral dissertation, Purdue University).

12. Chiang, K. W., Tsai, M. L., Naser, E. S., Habib, A., & Chu, C. H. (2015). New calibration method using low cost MEM IMUs to verify the performance of UAV-borne mms payloads. *Sensors*, 15(3), 6560-6585.
13. Gabrlik, P., Cour-Harbo, A. L., Kalvodova, P., Zalud, L., & Janata, P. (2018). Calibration and accuracy assessment in a direct georeferencing system for UAS photogrammetry. *International Journal of Remote Sensing*, 39(15-16), 4931-4959.
14. Agisoft. (2013). November 08 2018, from <http://www.agisoft.ru>
15. Blázquez, M., & de la Tecnologia, P. M. (2008). A new approach to spatio-temporal calibration of multi-sensor systems. *Proceedings of the International Archives of the Photogrammetry, Remote Sensing and Spatial Information Sciences*, Beijing, China, 3-13.
16. Matese, A., Toscano, P., Di Gennaro, S. F., Genesio, L., Vaccari, F. P., Primicerio, J., & Gioli, B. (2015). Intercomparison of UAV, aircraft and satellite remote sensing platforms for precision viticulture. *Remote Sensing*, 7(3), 2971-2990.
17. Ravi, R., Hasheminasab, S. M., Zhou, T., Masjedi, A., Quijano, K., Flatt, J. E., Habib, A. (2019). UAV-based multi-sensor multi-platform integration for high throughput phenotyping. *Autonomous Air and Ground Sensing Systems for Agricultural Optimization and Phenotyping IV*. (Vol. 11008, p. 110080E). International Society for Optics and Photonics.
18. Masjedi, A., Zhao, J., Thompson, A. M., Yang, K., Flatt, J. E., Crawford, M. M., Chapman, S. (2018). Sorghum biomass prediction using UAV-based remote sensing data and crop model simulation. *IGARSS 2018 - 2018 IEEE International Geoscience and Remote Sensing Symposium* (pp. 7719-7722). IEEE.
19. Zhang, Z., Masjedi, A., Zhao, J., & Crawford, M. M. (2017). Prediction of sorghum biomass based on image based features derived from time series of UAV images. *2017 IEEE International Geoscience and Remote Sensing Symposium (IGARSS)*. (pp. 6154-6157). IEEE.
20. Chen, Y., Ribera, J., Boomsma, C., & Delp, E. (2017). locating crop plant centers from UAV-based RGB imagery. *2017 IEEE International Conference on Computer Vision Workshops (ICCVW)* (pp. 2030-2037).

21. Buchaillet, M.; Gracia-Romero, A.; Vergara-Diaz, O.; Zaman-Allah, M.A., Tarekegne, A.; Cairns, J.E.; Prassanna, B.M.; Araus, J. L.; and Kefauver, S.C. (2019). Evaluating maize genotype performance under low nitrogen conditions using RGB UAV phenotyping techniques. *Sensors*, 19(8), 1815.
22. Gracia-Romero, A., Kefauver, S. C., Fernandez-Gallego, J. A., Vergara-Díaz, O., Nieto-Taladriz, M. T., & Araus, J. L. (2019). UAV and ground image-based phenotyping: a proof of concept with Durum wheat. *Remote Sensing*, 11(10), 1244.
23. Pádua, L., Vanko, J., Hruška, J., Adão, T., Sousa, J. J., Peres, E., & Morais, R. (2017). UAS, sensors, and data processing in agroforestry: A review towards practical applications. *International journal of remote sensing*, 38(8-10), 2349-2391.
24. Habib, A., Han, Y., Xiong, W., He, F., Zhang, Z., & Crawford, M. (2016). Automated ortho-rectification of UAV-based hyperspectral data over an agricultural field using frame RGB imagery. *Remote Sensing*, 8(10), 796.
25. Bisquert, M., Sánchez, J. M., López-Urrea, R., & Caselles, V. (2016). Estimating high resolution evapotranspiration from disaggregated thermal images. *Remote sensing of environment*, 187, 423-433.
26. Merlin, O., Chirouze, J., Olioso, A., Jarlan, L., Chehbouni, G., & Boulet, G. (2014). An image-based four-source surface energy balance model to estimate crop evapotranspiration from solar reflectance/thermal emission data (SEB-4S). *Agricultural and Forest Meteorology*, 184, 188-203.
27. Zhang, D., & Zhou, G. (2016). Estimation of soil moisture from optical and thermal remote sensing: A review. *Sensors*, 16(8), 1308.
28. Sun, L., & Schulz, K. (2015). The improvement of land cover classification by thermal remote sensing. *Remote sensing*, 7(7), 8368-8390.
29. Sagan, V., Maimaitijiang, M., Sidike, P., Eblimit, K., Peterson, K. T., Hartling, S., Esposito, F., Khanal, K., Newcomb, M., Pauli, D., Ward, R., Fritschi, F., Shakoob, N., Mockler, T. (2019). UAV-based high resolution thermal imaging for vegetation monitoring, and plant phenotyping using ICI 8640 P, FLIR Vue Pro R 640, and thermomap cameras. *Remote Sensing*, 11(3), 330.
30. Zhang, Z. (2000). A flexible new technique for camera calibration. *IEEE Transactions on pattern analysis and machine intelligence*, 22(11), 1330-1334.

31. Costa, F. A. L., & Mitishita, E. A. (2019). An approach to improve direct sensor orientation using the integration of photogrammetric and lidar datasets. *International Journal of Remote Sensing*, 40(14), 5651-5672.
32. He, F., Zhou, T., Xiong, W., Hasheminnasab, S. M., & Habib, A. (2018). Automated aerial triangulation for UAV-based mapping. *Remote Sensing*, 10(12), 1952.
33. Tomašík, J., Mokroš, M., Surový, P., Grznárová, A., & Merganič, J. (2019). UAV RTK/PPK Method—An Optimal Solution for Mapping Inaccessible Forested Areas?. *Remote sensing*, 11(6), 721.
34. Chiang, K. W., Tsai, M. L., & Chu, C. H. (2012). The development of an UAV borne direct georeferenced photogrammetric platform for ground control point free applications. *Sensors*, 12(7), 9161-9180.
35. Padró, J. C., Muñoz, F. J., Planas, J., & Pons, X. (2019). Comparison of four UAV georeferencing methods for environmental monitoring purposes focusing on the combined use with airborne and satellite remote sensing platforms. *International Journal of Applied Earth Observation and Geoinformation*, 75, 130-140.
36. Rehak, M., Mabillard, R., & Skaloud, J. (2013). A micro-UAV with the capability of direct georeferencing. *International Archives of the Photogrammetry, Remote Sensing and Spatial Information Sciences.*, XL-1/W2, 317-323.
37. Sedaghat, A., & Mohammadi, N. (2019). Illumination-Robust remote sensing image matching based on oriented self-similarity. *ISPRS Journal of Photogrammetry and Remote Sensing*, 153, 21-35.
38. Delara, R., Mitishita, E. A., & Habib, A. (2004). Bundle adjustment of images from non-metric CCD camera using LIDAR data as control points. In *International Archives of XXth ISPRS Congress* (pp. 13-19).
39. Matrice 200 User Manual. (2018). November 08 2018, from https://dl.djicdn.com/downloads/M200/20180910/M200_User_Manual_EN.pdf
40. Matrice 600 Pro User Manual. (2018). November 08 2018, from https://dl.djicdn.com/downloads/m600%20pro/20180417/Matrice_600_Pro_User_Manual_v1.0_EN.pdf
41. APX 2017. Trimble APX-15UAV(V2) - Datasheet. (2016). May 01 2020, from https://www.applanix.com/downloads/products/specs/APX15_DS_NEW_0408_YW.pdf

42. FLIR 2018. FLIR Duo Pro R - User Guide. (2018). November 08 2018, from <https://www.flir.com/globalassets/imported-assets/document/duo-pro-r-user-guide-v1.0.pdf>.
43. Sony 2018. Sony ILCE-7R – Specifications and Features. (2018). November 08 2018, from <https://www.sony.com/electronics/interchangeable-lens-cameras/ilce-7r/specifications>
44. Lowe, D. G. (2004). Distinctive image features from scale-invariant keypoints. *International journal of computer vision*, 60(2), 91-110.
45. Hasheminasab, S. M., Zhou, T., & Habib, A. (2020). GNSS/INS-Assisted Structure from Motion Strategies for UAV-Based Imagery over Mechanized Agricultural Fields. *Remote Sensing*, 12(3), 351.
46. Zhao, L., Hu, Y., Zhou, W., Liu, Z., Pan, Y., Shi, Z., Wang, L., Wang, G. (2018). Estimation Methods for Soil Mercury Content Using Hyperspectral Remote Sensing. *Sustainability*, 10(7), 2474.
47. Notesco, G., Weksler, S., & Ben-Dor, E. (2020). Application of Hyperspectral Remote Sensing in the Longwave Infrared Region to Assess the Influence of Dust from the Desert on Soil Surface Mineralogy. *Remote Sensing*, 12(9), 1388.
48. Lin, Y., Cheng, Y., Zhou, T., Ravi, R., Hasheminasab, S., Flatt, J. E., Troy, C., Habib, A. (2019). Evaluation of UAV LiDAR for Mapping Coastal Environments. *Remote Sensing*, 11(24), 2893.
49. Hakkenberg, C. R., Zhu, K., Peet, R. K., & Song, C. (2018). Mapping multi-scale vascular plant richness in a forest landscape with integrated LiDAR and hyperspectral remote-sensing. *Ecology*, 99(2), 474-487.
50. Laforest, L., Hasheminasab, S., Zhou, T., Flatt, J. E., & Habib, A. (2019). New Strategies for Time Delay Estimation During System Calibration for UAV-Based GNSS/INS-Assisted Imaging Systems. *Remote Sensing*, 11(15), 1811.
51. Ravi, R., Lin, Y. J., Elbahnasawy, M., Shamseldin, T., & Habib, A. (2018). Bias impact analysis and calibration of terrestrial mobile lidar system with several spinning multibeam laser scanners. *IEEE Transactions on Geoscience and Remote Sensing*, 56(9), 5261-5275.
52. Headwall Nano- Hyperspectral Sensor Product Data Sheet. (2018). May 01 2020, from https://geo-konzept.de/wp-content/uploads/2019/12/NanoHyperspec0118_prospect.pdf

53. Headwall Micro-Hyperspectral Sensors Product Data Sheet. (2018). May 01 2020, from:
https://cdn2.hubspot.net/hubfs/145999/June%202018%20Collateral/MicroHyperspec0418.pdf?fbclid=IwAR0jXtSaQ3Mvx3gWmOFDVKN4YVoxb3XUcjlGhssg4tRyHTzMcBn_xoaa3RZA
54. Bay, H., Tuytelaars, T., & Van Gool, L. (2006, May). Surf: Speeded up robust features. In *European conference on computer vision* (pp. 404-417). Springer, Berlin, Heidelberg.
55. Sedaghat, A., & Ebadi, H. (2015). Remote sensing image matching based on adaptive binning SIFT descriptor. *IEEE transactions on geoscience and remote sensing*, 53(10), 5283-5293.
56. Etezadifar, P., & Farsi, H. (2020). A New Sample Consensus Based on Sparse Coding for Improved Matching of SIFT Features on Remote Sensing Images. *IEEE Transactions on Geoscience and Remote Sensing*.
57. Kocaman, S., Zhang, L., & Gruen, A. (2006, January). Self-calibrating triangulation of airborne linear array CCD cameras. In *EuroCOW 2006 International Calibration and Orientation Workshop, Castelldefels, Spain* (Vol. 25, p. 27).
58. Koch, K. R. (1999). *Parameter estimation and hypothesis testing in linear models*. Springer Science & Business Media.
59. Mikhail, E., & Ackermann, F. (1982). *Observations and least squares*. Washington, D.C.: University Press of America.
60. Wang, T., Zhang, Y., Lin, L., & Pan, S. (2012). Airborne Three-Linear CCD Sensor ADS40 Geometric Calibration. *2012 8th International Conference on Wireless Communications, Networking and Mobile Computing*. (pp. 1-4). IEEE.
61. Adam, A., Rivlin, E., & Shimshoni, I. (2001). ROR: Rejection of outliers by rotations. *IEEE Transactions on Pattern Analysis and Machine Intelligence*, 23(1), 78-84.
62. Wu, C. (2007). A GPU implementation of scale invariant feature transform (SIFT). <http://www.cs.unc.edu/~ccwu/siftgpu/>.
63. Nistér, D. (2004). An efficient solution to the five-point relative pose problem. *IEEE transactions on pattern analysis and machine intelligence*, 26(6), 756-770.
64. Fischler, M. A., & Bolles, R. C. (1981). Random sample consensus: A paradigm for model fitting with applications to image analysis and automated cartography. *Communications of the ACM*, 24(6), 381-395.

65. Andersen, P. K., Klein, J. P., & Rosthøj, S. (2003). Generalised linear models for correlated pseudo-observations, with applications to multi-state models. *Biometrika*, 90(1), 15-27.